# CHARACTERIZATION OF METAL-CARBON NANOCOMPOSITE MAGNETIC THIN FILMS PREPARED BY PULSED FILTERED VACUUM ARC DEPOSITION

By

**Poon Chun Yu**

A Thesis Submitted in Partial Fulfilment of the Requirements
for the Degree of Master of Philosophy in
Electronic Engineering



July 2002

# Acknowledgements

I would like to express my sincere gratitude to my supervisor, Professor Wong Sai-Peng, for his valuable advice and constant encouragement during the last two years at the Chinese University of Hong Kong.

Moreover, I would like to thank Dr. Cheung Wing-Yu and Dr. Ke Ning for their valuable discussions and constructive advise in the experiments. Besides, thanks to Dr. H. Wang and Mr. M. F. Chiah for lots of valuable suggestions and encouragement when I am facing the problems in my work. Thanks also to Mr. W. K. Chan who offered many excellent suggestions for improving the experimental techniques.

Thanks to my lab mates, Dr. D. H. Chen, Dr. H. J. Peng, Dr. P. Chen, Dr. Z. S. Xiao, Dr. H. Y. Guo, Ms. Y. Gao, Mr. K Xue, Mr. Y. M. Fung, Mr. W. M. Tsang, Mr. T. B. Ng, Mr. C. H. Ng, Mr. K. W. Lo and K. H. Cheng.

Besides, I would like to acknowledge the financial support of the Chinese University of Hong Kong for providing the Graduate Studentship.

Last but not least, I would like to thank my parents who have given me constant encouragement and support throughout the course of my M. Phil. research work.

## Abstract

Magnetic thin films of Co-C and Fe-C were prepared by a pulsed filtered vacuum arc deposition technique. Annealing was performed in vacuum ($<10^{-3}$ Pa) for one hour at various temperatures. The structural evolution and magnetic properties of the films were studied by non-Rutherford backscattering spectrometry (NRBS), x-ray diffraction (XRD), Raman spectroscopy, transmission electron microscopy (TEM), x-ray photoelectron spectroscopy (XPS), atomic force microscopy (AFM), magnetic force microscopy (MFM) and vibrating sample magnetometry (VSM). The resistivity of the films is measured by the four-contacts technique.

The composition and thickness of the thin films were determined by NRBS. The dependence of magnetic properties on the carbon composition and processing conditions was studied. For Co-C films, XRD results showed that the as-deposited films were amorphous and the Co grains crystallized into hexagonal close packed (hcp) phase after annealing. The grain size was also determined by XRD measurements. Higher annealing temperature and higher Co concentration resulted in larger grain size. High coercive fields were achieved in films with optimal combinations of large grain size and weak intergrain exchange coupling was happened.

The structural and magnetic properties of Fe-C films were also studied. For the as-deposited $Fe_{90}C_{10}$ films, the saturation magnetization was about 1550 emu/cm$^3$. The coercive field and resistivity of these films were determined to be about 7 Oe and 98 $\mu\,\Omega$cm at room temperature, respectively. The roughness of the films was

measured to be about 0.15nm. These properties showed that they are promising for high-density magnetic recording head applications.

## 摘要

本論文研究利用脈衝磁過濾方法制備 Co-C 和 Fe-C 磁性薄膜，並在不同溫度下對樣品進行真空退火處理。利用盧瑟福背散射(NRBS)、X-射線衍射(XRD)、拉曼譜、透射電子顯微鏡(TEM)、光電子能量譜(XPS)、原子力顯微鏡(AFM)、磁力顯微鏡(MFM)和振動樣品磁強計(VSM)等表證手段分析了制備簿膜的結構和磁特性。並利用四端法測量了樣品的電阻率。

首先利用盧瑟福背散射技術分析了樣品的組份和厚度。再研究了不同組份的碳以及不同的制作條件怎樣影響其磁的特性。對 Co-C 樣品，X-射線衍射結果顯示未經加熱退火的樣品是非晶的。經過加熱退火後，Co 原子結晶成六方密堆積(hcp)結構。X-射線衍射結果亦給出晶尺寸粒的大小。XRD 結果顯示退火溫度越高和 Co 的含量越高，顆粒尺寸就越大。透過調整退火溫度和工藝參數，可研製出適當的晶粒尺寸和弱的交換耦合，從而得出 700 Oe 較高的矯頑力 Co-C 樣品。

另外，我們也研究了 Fe-C 磁性薄膜的結構和磁特性，例如未經退火的 $Fe_{90}C_{10}$ 樣品，它的磁矩是 1550 emu/cm$^3$，室溫的矯頑力和電阻率分別是 7 Oe 和 98 $\mu\Omega$cm，而粗糙度是 0.15nm，這樣的特性最適合用作爲高儲存量的磁頭應用。

# Table of contents

# List of Figures

# List of Tables

# Chapter 1 Introduction

## 1.1 Overview

In recent years, hard and soft magnetic films have attracted increasing research interests for their wide applications in integrated magnetic and magnetoelectreonic devices such as magnetic storage media, magnetic sensors and spin valves. Until now, most Co-C phases and their magnetic properties have been reported but there are few not many papers on magnetic thin films with low cobalt content. Moreover, it is well known that ferromagnetic amorphous alloys of TM (3d-transition metals)-metalloids and TM-metal systems (such as Co-Zr, Co-Ti, Co-Ta) have large saturation magnetization and excellent soft magnetic properties compared to those of Fe-rich amorphous alloys. Meanwhile, since the discovery of the Huffman-Kratschmer carbon arc process for the production of fullerences [1], there has been increasing interest in the study of carbon-coated nanoparticles [2]. It was pointed out that carbon encapsulated magnetic nanoparticles can be used as high density magnetic recording media, high-resistive soft magnetic materials, magnetic toner in xerography, ferrofluid, and contrast agents in magnetic resonance imaging. The carbon encapsulation can, on the one hand, provide protection against surface oxidation of the magnetic nanoparticles, which is of practical importance because a slight contamination by magnetic oxide can lead to significant effect on the coercivity and saturation magnetization values of nanoparticles. Moreover, it also increases the effective separation between neighbouring nanoparticles to weaken or eliminate the exchange coupling between them, which is another issue of concern for the application of these materials as ultra-high-density magnetic recording media. These carbon-coated magnetic nanoparticles and granular metal carbon films have been prepared using various methods including the standard pulse laser deposition

[3], dc magnetron co-sputtering [4], ion beam co-sputtering [5], and lower-energy cluster beam deposition [6].

## 1.2 Ferromagnetism

Certain metallic materials possess a permanent magnetic moment in the absence of an external field, and manifest very large and permanent magnetizations [7]. These are the characteristics of ferromagnetism, a number of transition metals including iron (as BCC $\alpha$-ferrite), cobalt, nickel, and some of the rare earth metals such as gadolinium (Gd) are ferromagnetic materials. Magnetic susceptibilities as high as $10^6$ are possible for ferromagnetic materials. Consequently, in the absence of external magnetic field H=0 or under small field H<<M, from the equation $B = \mu_o H + \mu_o M$, we can write:

$$B = \mu_o M \qquad \text{(Equation 1.1)}$$

where $\mu_o$ is the permeability of a vacuum, a universal constant with a value of $4\pi \times 10^{-7}$ H/m.

Permanent magnetic moments in ferromagnetic materials result from atomic magnetic moments due to electron spin—uncancelled electron spins as a consequence of the electronic structure. There is also an orbital magnetic moment contribution that is small in comparison to the spin moment. Furthermore, in a ferromagnetic material, coupling interaction causes net spin magnetic moments of adjacent atoms to align with one another, even in the absence of an external field. This is schematically illustrated in Fig 1.1. This mutual spin alignment exists over relatively large volume regions of the crystal called domains.

The saturated magnetization $M_s$ of a ferromagnetic material represents the magnetization that results when all the magnetic dipoles in a solid piece are mutually aligned with the external field. There is also a corresponding saturation flux density $B_s$. The saturation magnetization is equal to the product of the net magnetic moment for each atom and the number of atoms present. For iron, cobalt, and nickel, the net magnetic moments per atom are 2.22, 1.72 and 0.60 Bohr magnetons, respectively.

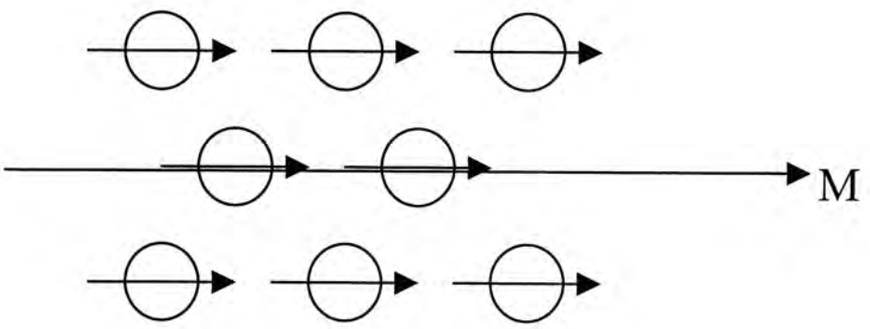


Fig. 1.1 In a magnetized region of a ferromagnetic material, all the magnetic moments are aligned in the same direction There is a strong magnetization vector M even in the absence of an applied external magnetic field

### 1.3 Ferromagnetic granular thin film

As shown in Fig 1.2, in the absence of an applied magnetic field, the magnetic moments of the granules are randomly aligned, and the conduction electrons are strongly scattered. Under an external magnetic field, the randomly oriented magnetic moments of the granules are gradually aligned, leading to a reduction of the electrical resistance.

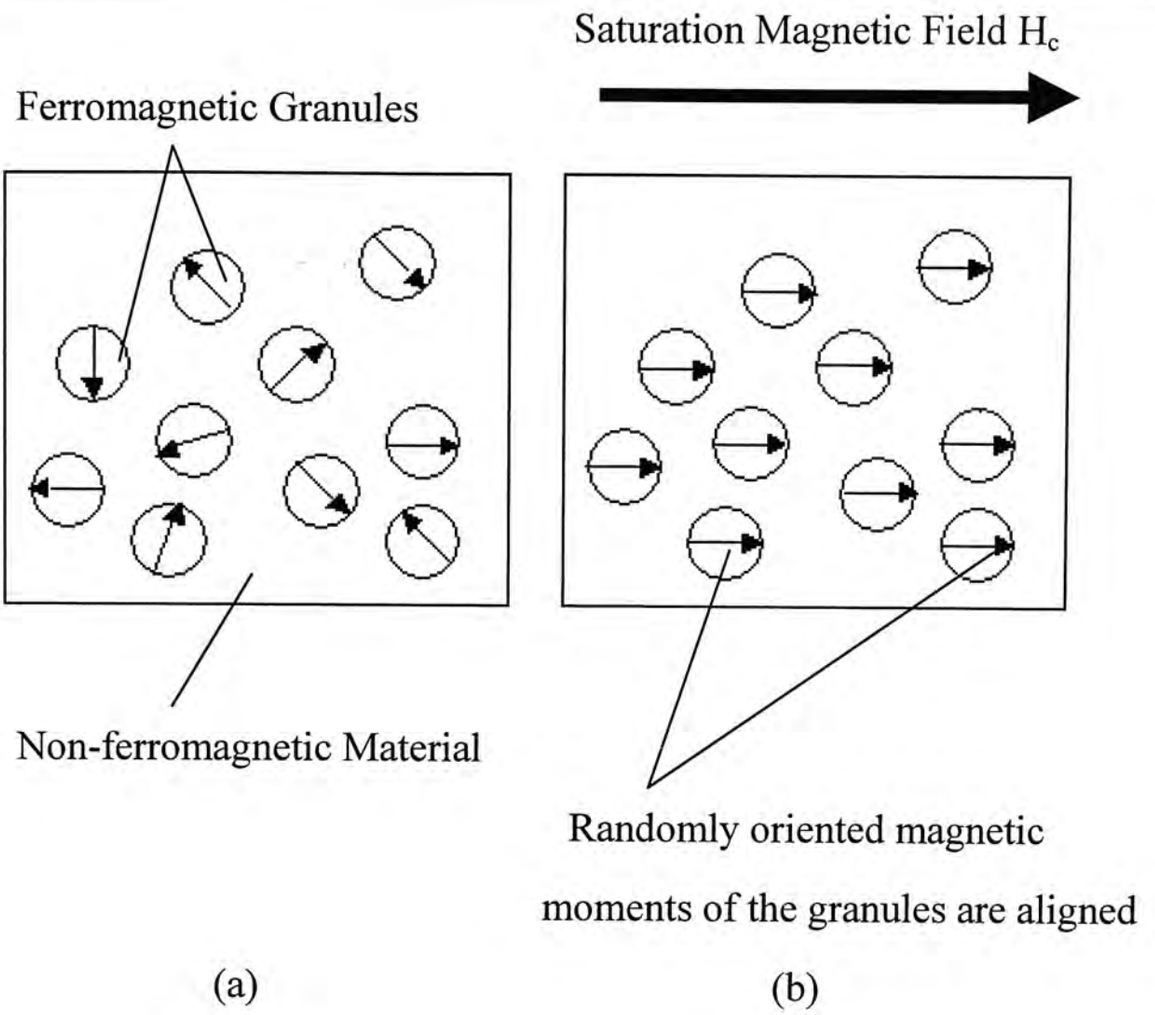


**Fig 1.2** The magnetization state of granular thin film with (a) no magnetic field applied and (b) a saturation magnetic field applied

### 1.4 Ferromagnetism-magnetization

To minimize magneto static energy a ferromagnetic crystal has to minimize the demagnetizing field which is proportional to its magnetization by dividing the crystal into two domains where the magnetizations are on opposite direction [7]. This process is limited by balance with energy need to create a domain (Fig. 1.3). Each domain is magnetizated to its saturation magnetization. Adjacent domains are separated by domain boundaries or walls, across which the direction of magnetization gradually changes (Fig. 1.3). Normally, domains are microscopic in size, and for a polycrystalline specimen, each grain may consist of more than a single

domain. Thus, in a macroscopic piece of material, there will be a large number of domains, and all may have different magnetization orientations. The magnitude of the magnetization M for the entire solid is the vector sum of the magnetizations of all the domains, each domain contribution being weighted by its volume fraction. For an unmagnetized specimen, the appropriately weighted vector sum of the magnetization of all the domains is zero.

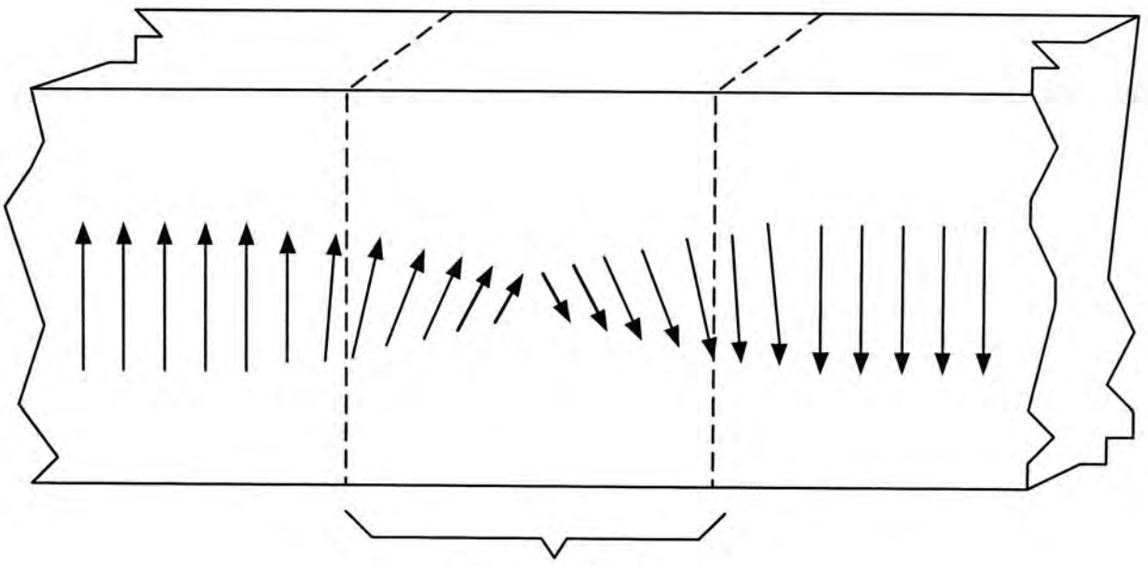


Fig. 1.3 The gradual change in magnetic dipole orientation across a domain wall

## 1.5 Ferromagnetism – magnetization of a polycrystalline material

Magnetization M and field intensity H are not proportional for a ferromagnet and ferrimagnet. If the material is initially unmagnetized, then M varies as a function of H as shown in Fig. 1.4. The curve begins at the origin, and as H is increased, the magnetization M begins to increase slowly, then more rapidly, finally leveling off and becoming independent of H. The maximum value of M is the saturation magnetization $M_s$. Since the permeability $\mu$ is the slope of the M-H

curve, it may be noted that the permeability changes with and is dependent on H [7].

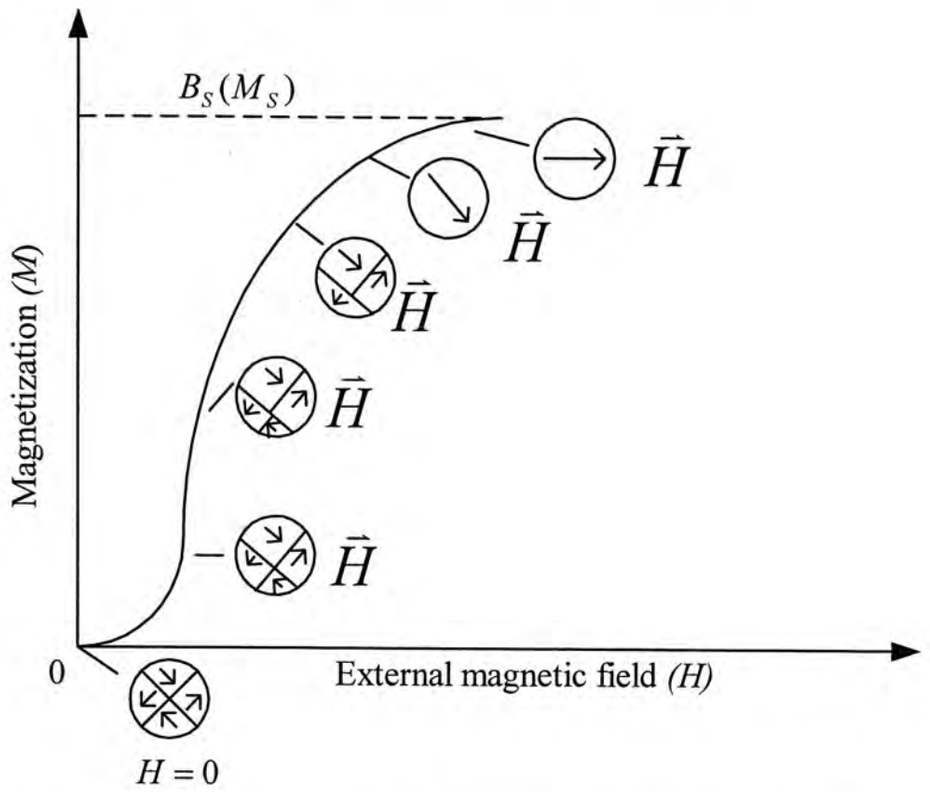


**Fig. 1.4** The M-H behaviour for a ferromagnetic material that was initially unmagnetized. Domain configurations during several stages of magnetization are represented.

As a magnetic field H is applied, the domains change shape and size by the movement of domain boundaries. Schematic domain structures are represented at several points along the M-H curve in Fig 1.5. Initially, the moments of the constituent domains are randomly oriented such as there is no net magnetization. As the external field is applied, the domains that are oriented in directions favorable to the applied field grow at the expense of those that are unfavorably oriented. This process continues with increasing field strength until the macroscopic specimen becomes a single domain, which is nearly aligned with the field. Saturation is achieved when the magnetization of this domain, becomes oriented with the H field.

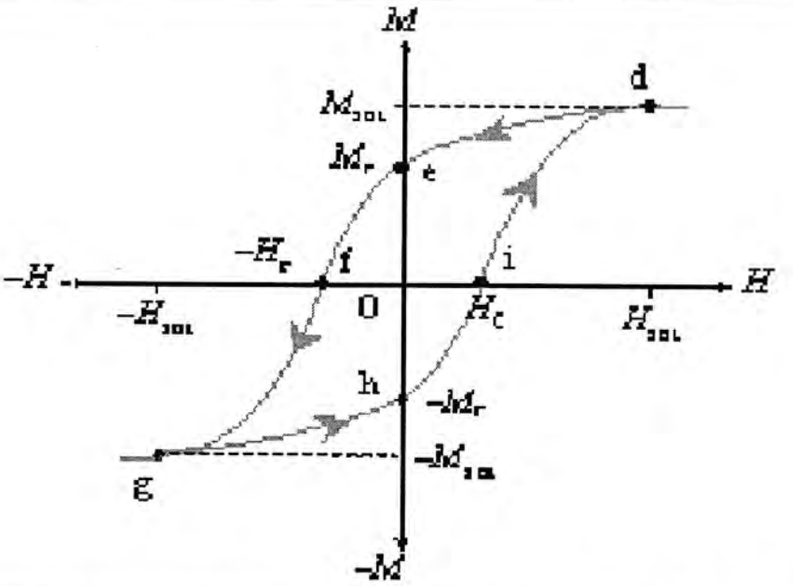


**Fig. 1.5** Magnetization versus the external magnetic field for a ferromagnetic material that is subjected to forward and reverse saturations (point d and g). The hyteresis loop is represented by the solid curve; the dashed curve indicates the initial magnetization. The remanence $M_r$ and the coercive force $H_c$ are also shown

The motion of domain walls may explain hysteresis behavior and permanent magnetization. Upon reversal of the field direction from saturation (point d and g in Fig.1.5), the process by which the domain structure changes is reversed. First, there is a rotation of the single domain with the reversed field. Next, domains having magnetic moments aligned with the new field form and grow at the expense of the former domains. Critical to this explanation is the resistance to movement of domain walls that occurs in response to the increase the magnetic field in the opposite direction. When the applied field reaches zero, there is still some net volume fraction of domains oriented in the former direction, which explains the existence of the remanence $M_r$.

To reduce the magnetization M within the specimen to zero (point f and i on Fig 1.5), an H field of magnitude $|-H_c|$ must be applied in a direction opposite to that of the original field; $H_c$ is called coercivity. Upon continuation of the applied field in this reverse direction, saturation is ultimately achieved in the opposite sense,

corresponding to point g. A second reversal of the field to the point of the initial saturation (point d) completes the symmetrical hysteresis loop and also yields both a negative remanences ($-M_r$) and a positive coercivity ($+H_c$).

## 1.6 Soft and hard magnetic materials

Both ferromagnetic and ferrimagnetic materials are classified as either soft and hard on the basis of their hyteresis characteristics [7]. Firstly, soft magnetic materials are used in devices that are subjected to alternating magnetic fields and in which energy losses must be low. Consequently, a soft magnetic material must have a high initial permeability and a low coercivity. A material possessing these properties may reach its saturation magnetization with a relatively low applied field (i.e., is easily magnetized and demagnetized) and still has low hyteresis energy losses. Secondly, hard magnetic materials must have a high resistance to demagnetization. In terms of hyteresis behavior, a hard magnetic material has a high remanence, coercivity and saturation flux density, as well as a low initial permeability and high hyteresis energy losses. The hyteresis characteristics for hard and soft magnetic materials are compared in Fig 1.6.

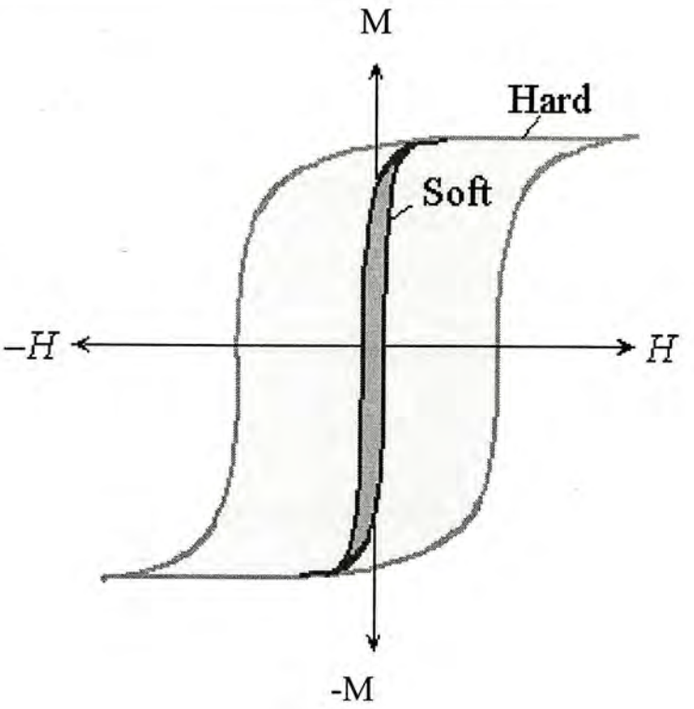


**Fig. 1.6** Schematic M-H loops for hard and soft magnetic materials

## 1.7 Preparation methods

Since the discovery of the Huffman-Kratschmer carbon arc process for the production of fullerences, there has been increasing interest in the study of carbon-coated nanoparticles. Furthermore, a real densities in longitudinal magnetic recording have reached 40-100 Gbits/in$^2$ [8]. At such densities, tight control of the media microstructure, especially grain size, grain size dispersion and chemical isolation to break the magnetic exchange are necessary, in order to keep the media noise within acceptable bounds [9]. However, due to the superparamagnetic behavior, the magnetization of the bit cell becomes destabilized. To avoid the thermal instability, a minimal stability ratio of stored magnetic energy, $K_uV$, to thermal energy, $k_BT$, $\frac{K_uV}{k_BT} \cong 50-70$, is required [2]. $K_u$ and V are the anisotropic energy density and magnetic switching volume, respectively. V typically drops with high areal density, hence higher $K_u$ materials are needed to maintain the stability. However, the

uniaxial magnetocrystalline anisotropy $K_u$ of hcp-cobalt is quite high. It has the anisotropies in the $10^6$ erg/cm$^3$ regime. Moreover, there is no report on observation of the magnetic characterization of carbon-coated to the composition Co below 50 at.%.

As data rates in magnetic recording approach gigahertz levels, much effort has been invested in developing magnetically soft, high-moment materials with high resistivity to minimize eddy current effects in magnetic recording heads. With a saturation magnetization in the range of 1400-1700 emu/cm$^3$, FeXN (X= Ta, Ti, Cr, etc.) thin films have been the focus of much research [10, 11]. Their magnetically soft properties (coercivity $H_c < 5$Oe) [10] and combined with a high saturation moment make them particularly interesting for recording head applications. However, moderate resistivities of ~100 $\mu\Omega$ cm [12] can limit their permeability at high frequencies. In fact, there is no report on the iron-carbon granular thin film for recording head applications. We have a great interest to observe these granular thin films.

Among these studies, there are a few recent attempts to synthesize granular thin films by pulsed filtered cathodic arc co-deposition system which is a new method for sample preparation.

In this work, we use pulsed filtered cathodic arc co-deposition system to co-deposit cobalt-carbon and iron-carbon onto silicon dioxide substrate. As a result, the Co-C and Fe-C granular thin films are prepared. We can vary the different composition of Co and Fe.

## 1.8 This thesis

In this thesis, we report on that the magnetic granular thin films of Co-C and Fe-C were prepared by a pulsed filtered vacuum arc deposition technique. Annealing was performed in vacuum ($<10^{-3}$ Pa) for one hour at various temperatures. The structures and magnetic properties of the films were studied by non-Rutherford backscattering spectrometry (NRBS), x-ray diffraction (XRD), Raman spectroscopy, transmission electron microscopy (TEM), x-ray photoelectron spectroscopy (XPS), resistivity measurement, atomic force microscopy (AFM), magnetic force microscopy (MFM) and vibrating sample magnetometry (VSM).

The objectives of this thesis include the preparation and characterization of Co-C samples with Co concentrations below 50 at.% and to investigate their potential for high density magnetic recording applications, as well as the synthesis of Fe-C samples and to study their properties and potential for magnetic writing head applications. The pulsed filtered vacuum arc deposition technique is a new method. Since the system is operated in the pulse mode, the thickness and composition of the deposited films can be more easily and precisely controlled

In chapter 2, the details of the sample preparation and the methods of measurement are presented. In chapters 3 and 4, the discussions and results of the Co-C and Fe-C granular thin films will be presented respectively. In the final chapter, we would like to give the summarized of the main research results and the suggestion for future work.

# Chapter 2 Sample preparation and experimental methods

## 2.1 Sample preparation

### 2.1.1 The pulsed filtered cathodic arc co-deposition system

The pulsed filtered cathodic arc co-deposition system is a new method for deposition. It is custom made by the Institute of Low Energy Nuclear Physics, Beijing Normal University. The system is designed to use vacuum arc discharge to produce high-density metal plasma and they are guided through a bent magnetic field to deposit thin films on the substrate negatively biased in the vacuum chamber. The composition and thickness of the deposited thin films can be more easily and precisely controlled because the system is operated in the pulse mode. When the deposition is in process, the pressure always keep below $4\times10^{-4}$ Pa.

The schematic of the filtered vacuum-arc plasma source is shown in Fig. 2.1. When a trigger voltage is applied between the trigger and the cathode electrodes, a spark is formed to initiate the arc. The trigger voltage is set at 8kV with pulse width about of 6 $\mu$ s and repetitive frequency adjustable from 0 to 25 Hz. The arc power is applied between the cathode and anode electrodes to pulsely sustain the main arc. The width of the arc voltage is fixed at 2.5ms and its magnitude is variable up to 250V. When the arc is initiated by a high voltage pulse trigger and sustained between the solid cathode and the cylindrical anode, a plasma consisting of ionised metal vapour of the cathode material produces at discrete, minute areas across on the cathode surface. Both the cathode and anode are water-cooled.

Focus magnetic field is employed to sweep the spots over the cathode surface in order to provide more uniform cathode erosion and to confine the plasma

from the source.

The concentrated heat flux and the bombardment of ions under electric field at the cathode surface from microscopic liquid pools and then form droplets or so-called macroparticles, which are ranged from 0.1 $\mu$m to 10 $\mu$m in dimensions. If the macroparticles become entrained in the plasma stream and arrive at the substrate surface, they can cause serious degradation to the quality of the deposited films such as inclusion and pinhole defects in the films. So a conventional method, the curved magnetic filter is used to reduce the macroparticles from the vacuum arc plasma in the cathodic arc plasma from arriving at the substrate in order to drastically reduce the macroparticles contamination of the films. For cobalt and iron channel (source position 2), the filter consists of a 90° bent filter duct and a guiding solenoid (filter magnetic coil) which generates the guiding magnetic field. For the carbon channel (source position 1), there are the 65° and 45° double bent magnetic filter coils in order to filter the carbon macroparticles (Fig. 2.2) [13]. The two angles are in different plane. The filter ducts are water-cooled too.

The system consists of a spherical deposition vacuum chamber 50cm in diameter. There are three ports for arc plasma sources, three ports for pumping, a window and a door. It can provide three different species of metal plasma transported to the spherical vacuum chamber simultaneously for deposition because the system is equipped with three filtered arc plasma sources. A schematic of the pulsed filtered vacuum arc deposition system is shown in Fig. 2.3. In this work, two adjacent sources with (cobalt / iron) and carbon as the cathode materials were used simultaneously. The substrate could be placed in the line facing to the bisector of two sourced. For my sample preparation, (cobalt / iron) source and the carbon source are

placed to sources 2 and 1, respectively. The substrate is placed to position 2 which in the line facing to the bisector of cobalt / iron and carbon sources.

### 2.1.2 Details of sample preparation

(100) Silicon wafers are used as the substrates with a thickness of about 460-490 $\mu$ m. To eliminate the shunting effect from the substrate, 100 nm thick silicon dioxide were grown on the substrate by wet thermal oxidation at 1050℃ for 40 minutes. Then the cobalt-carbon and iron-carbon films in a desired thickness were deposited on the substrate.

The granular magnetic thin films of $Co_xC_{1-x}$ and $Fe_yC_{1-y}$ of various compositions were prepared using a pulsed filtered cathodic arc co-deposition system. The composition of the films was varied by adjusting the arc discharge conditions of the sources and by monitoring the integrated charge arriving at the sample holder from the respective arc sources. The bias, arc and trigger voltages were adjusted in order to maintain the stability of the cathodic arc source. The actual composition and thickness of the films was determined by non-Rutherford Backscattering Spectroscopy. The details of characteristics for deposition are shown in Table 2.1

**Table 2.1** The details of characteristics for deposition from different sources

| | Cobalt | Carbon | Iron |
|---|---|---|---|
| Bias | 107V | 140V | 105V |
| Focus | 80 $\mu$ A | 135 $\mu$ A | 85 $\mu$ A |
| Arc | 120V | 150V | 125V |
| Trigger | 125V | 155V | 125V |
| Deflect | 125 $\mu$ A | 150 $\mu$ A | 130 $\mu$ A |

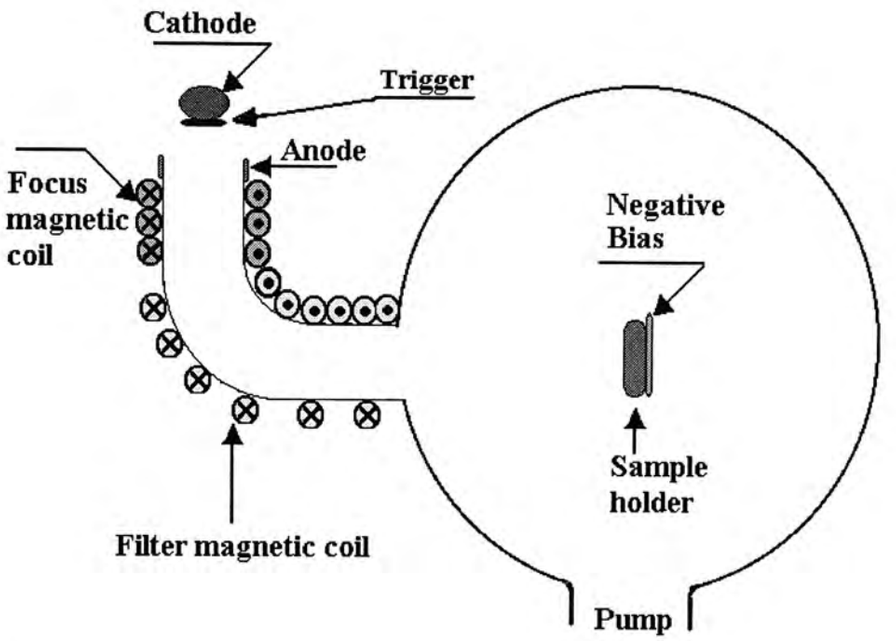


**Fig. 2.1** A schematic of the filtered vacuum-arc plasma source

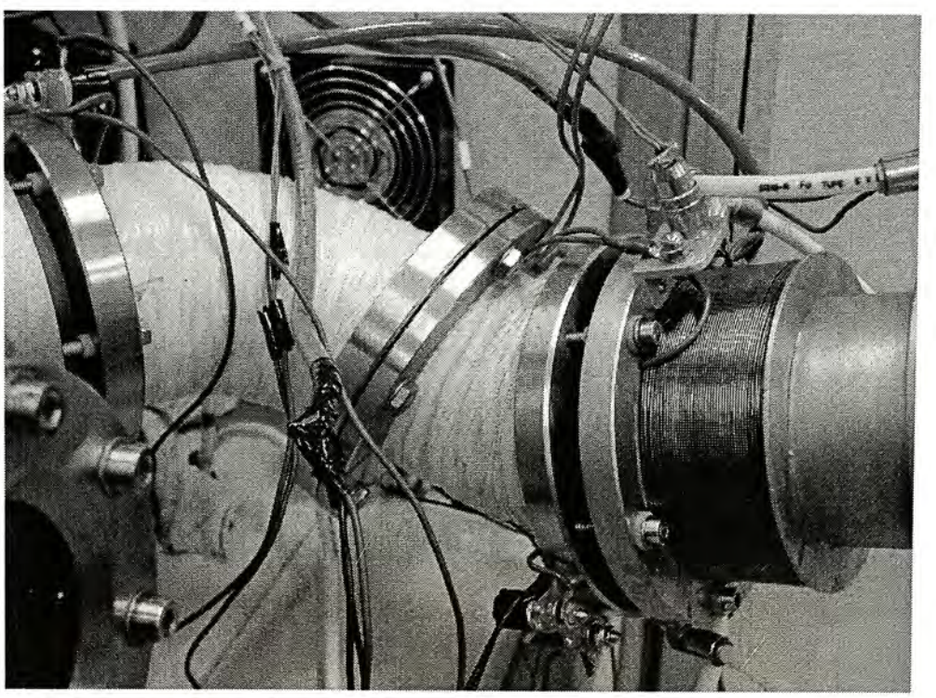

**Fig 2.2** The 65° and 45° double bent magnetic filter coils

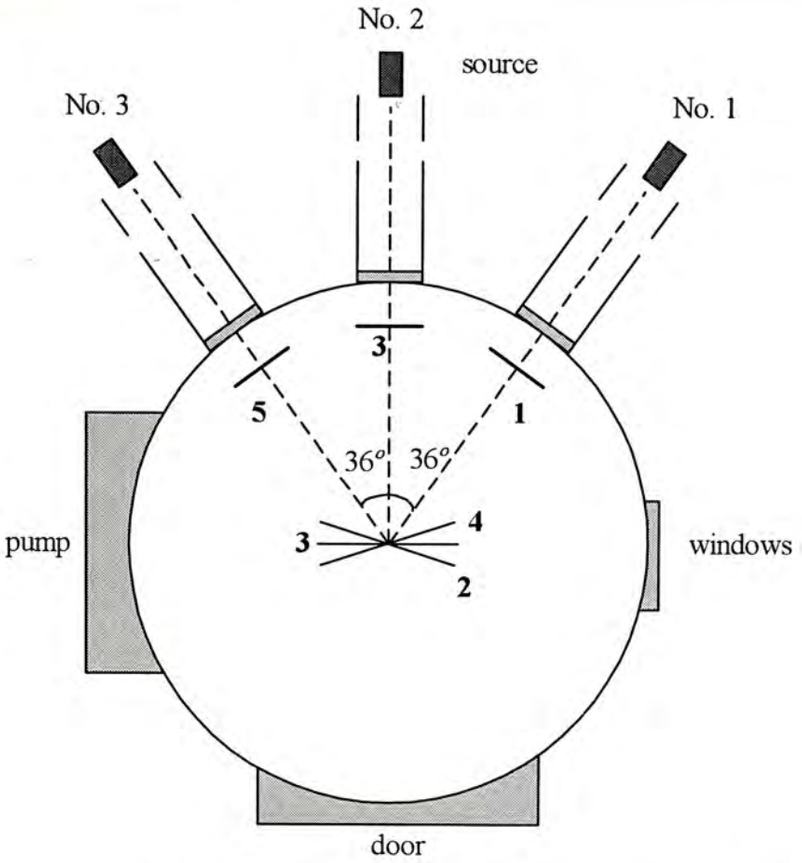


**Fig. 2.3** The schematic of the filtered vacuum-arc plasma source deposition system

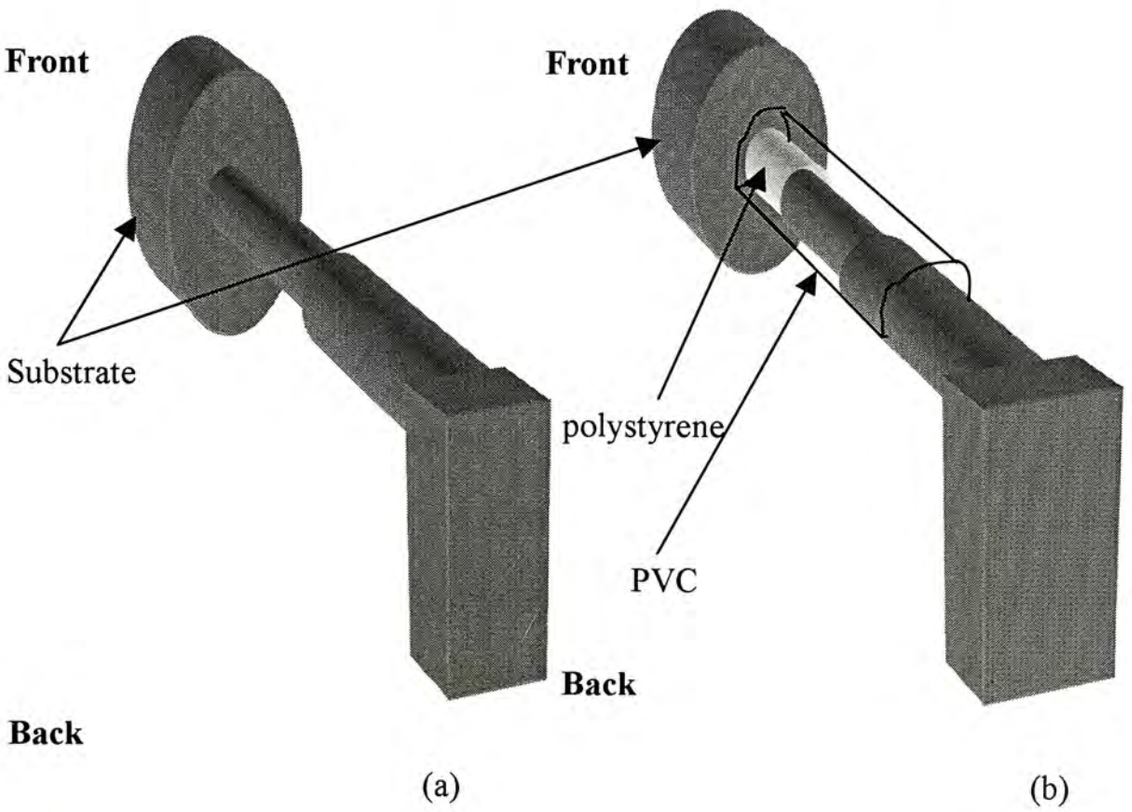


**Fig. 2.4** (a) Before improvement of the target holder. (b) After improvement of the target holder

### 2.1.3 Improvement of the target holder

Before improvement (Fig. 2.4(a)), the entire target holder is electrically connected to the substrate bias voltage of –80V. Therefore, the positive ions in the plasma would strike onto the whole negative by biased holder assembly. It was difficult to estimate the effective area that would collect the incoming ions from the plasma. Therefore the rate of ions arriving at the sample surface could not be determined accurately. Improvement was done by the insert ion of a polystyrene isolator and PVC shield behind the sample holder as shown in Fig. 2.4(b). The purpose of inserting the polystyrene isolator and the PVC shield is to provide electrical insulation between the front surface of the sample holder and the rear part of the sample holder assembly so that the effective area receiving the incoming ions is restricted to the front surface of the sample holder, hence allowing a more accurate determination of the ion dose. The polystyrene is tough enough in order to support the front target holder. Finally, the accuracy of the film composition and the thickness of the films samples will be improved.

## 2.2 Rutherford backscattering spectrometry (RBS):

Rutherford Backscattering Spectrometry (RBS) is used to bombard a sample with very high helium ions, and to measure the yield and energy of backscattered helium. RBS is an energy spectrometry of MeV He+ ions, elastically scattered by the nucleus of the analytical sample, providing with the stoichiometry and thickness of the magnetic granular thin films on a substrate. It is a well developed and non-destructive characterization method. It is quantitative and relatively fast. It measures the energy distribution of the ions, which are backscattered from the sample at a defined angle.

Typically RBS is used not only to determine thin film thickness and composition as a function of depth, but also to determine lattice disorder and location of lattice impurities. However, in some cases, its sensitivity is not adequate, especially when the masses of the different nuclei present in the sample are not far enough apart [14].

In my work, non-Rutherford backscattering spectrometry (NRBS) was performed with a 2MV tandem accelerator at a resonance mode for the carbon atoms, using a beam of 3.5 MeV $^4He^{++}$ ions at an incident angle of 7° to the normal of the film plane and with the backscattered $He^{++}$ ions detected at a scattering angle of 170° with respect to the incident direction. With the detection of the energy of backscattered ions, one can determine the mass of the target atom and the depth at the collision taken place. Obviously, the energy of the backscattered ion after collision with the target atom depends on the mass of the target atom and the scattering angle. On the other hand, on the way to the depth at which the collision taken palace, as well as on the outward path to the detector after collision, the ion also loses energy to many electrons through the Coulombic interaction. Therefore, by the backscattering technique, the mass and hence the atomic number, and the depth of the element can be detected. To determine the thickness and composition of the film, the NRBS spectra are fitted and simulated by the computer software SIMNRA [15].

Generally, the positions of the peaks in the energy spectrum of the scattered particle give the atomic masses of the elements in the sample and the width of the peak correspond to the thickness of the film. The scattering cross-section is directly proportional to the square of the atomic number of the target atom and from

the ratio of the yield from the specific target atoms, the composition can also be found. The basic backscattering spectrometry is shown in Fig 2.5.

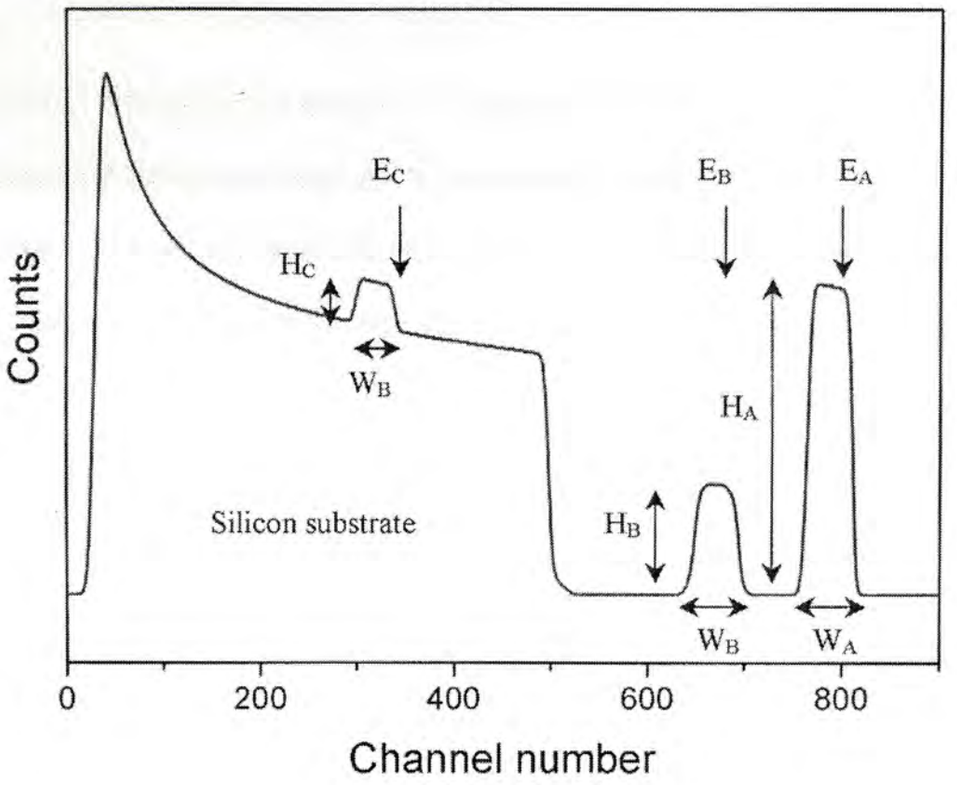


**Fig. 2.5** Backscattering spectrum for the three-element compound film of uniform composition on silicon substrate

For this backscattering spectrum (Fig. 5), EA, EB and EC are the rising edge of three elements. We can identify the atomic species by them. According to the relative height of the peak HA, HB and HC, we can find out the composition of the compound. For the film thickness, we can calculate it by the width of the peak WA, WB and WC.

## 2.3 X-ray diffraction (XRD)

### 2.3.1 Diffraction technique

X-ray Diffraction (XRD) is a powerful non-destructive technique for

characterizing crystalline materials. It provides information on structures, phases, preferential crystal orientations (texture) and other structural parameters such as average grain size, crystallinity, strain and crystal defects. X-ray diffraction peaks are produced by constructive interference of the monochromatic beam scattered from each set of lattice planes at specific angles. The peak intensities are determined by the atomic decoration within the lattice planes. Consequently, the X-ray diffraction pattern is the fingerprint of periodic atomic arrangements in a given material. An on-line search of a standard database for X-ray powder diffraction pattern enables quick phase identification for a large variety of crystalline samples [16].

When a powder or polycrystalline specimen consisting of many fine and randomly oriented particles that are exposed to monochromatic x-radiation, each powder particle (or grain) is a crystal, and having a large number of them with random orientations ensures that some particles are properly oriented such that every possible set of crystallographic planes will be available for diffraction.

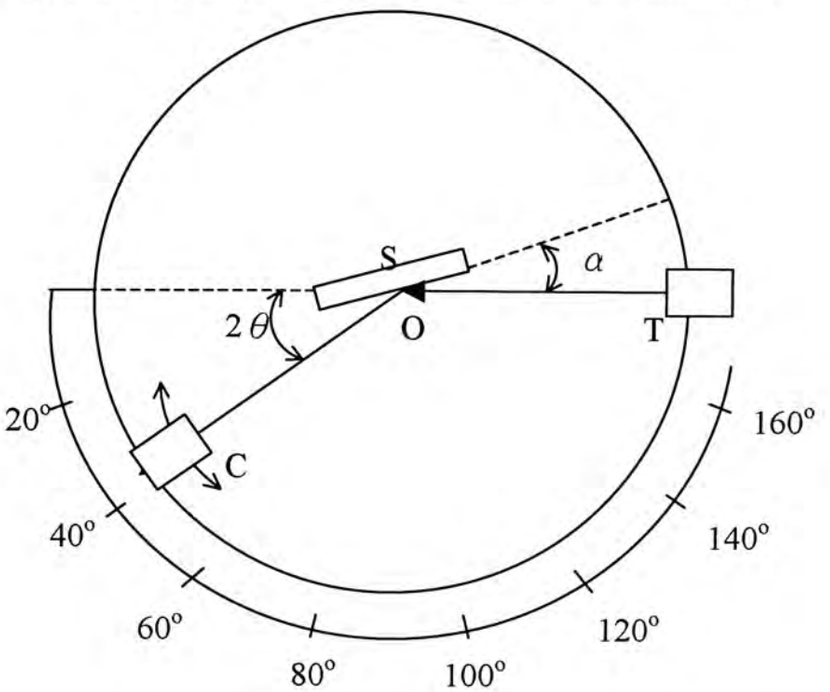


**Fig. 2.6** The schematic diagram of an x-ray-diffractometer; T = x-ray source, S = spectrum, C = detector and O = the axis around the specimen and detector rotate

The diffractometer is an apparatus used to determine the angles at which diffraction occurs for powdered specimens; its features are represented schematically in Fig 2.6. A specimen S in the form of a flat plate is supported so that rotations about the axis labeled O are possible; this axis is perpendicular to the plane of the page. The monochromatic x-ray beam is generated at point T, and the intensities of diffracted beams are detected with a counter labeled C in Fig. 2.6. The specimen, x-ray source, and counter are all coplanar.

The counter is mounted on a movable carriage that may also be rotated about the O axis; its angular position in term by a $2\theta$ is marked on a graduated scale. Carriage and specimen are mechanically coupled such that a rotation of specimen through $\theta$ is accompanied by a $2\theta$ rotation of the counter; this assures that the incident and reflection angles are maintained equal to one another (Fig 2.6). Collimators are incorporated within the beam path to produce a well-defined and focused beam. Utilization of a filter provides a near-monochromatic beam. For the $\alpha$-$2\theta$ mode, the incident angle $\alpha$ is fixed to be 1°.

As the counter moves at constant angular velocity, a recorder automatically plots the diffracted beam intensity (monitored by the counter) as a function of $2\theta$ is termed the diffraction angle, which is experimentally measured.

Other powder techniques have been devised wherein diffracted beam intensity and position are recorded on a photographic film instead of being measured by a counter.

One of the primary uses of x-ray diffractometry is for the determination of

crystal structure. The unit cell size and geometry may be resolved from the angular positions of the diffraction peaks, whereas the arrangement of atoms within the unit cell is associated with the relative intensities of these peaks.

X-rays, as well as electron and neutron beams, are also used in other types of material investigations. Other uses of x-rays include qualitative and quantitative chemical identification, and the determination of residual stresses and crystal size.

### 2.3.2 Scherrer's formula

By the Scherrer formula, crystal grain size can be determined. The formula is shown below:

$$D = \frac{K\lambda}{W\cos\theta} \qquad \text{(Equation 2.1)}$$

where $D$ is the grain size, $K$ is the constant ~ 0.9-1, $\lambda$ is the wavelength of the x-ray source (Cu-K$\alpha$ 0.15405nm), $W$ is the full-mean-half-maximum of the peak and $\theta$ is the diffracted angle.

## 2.4 Raman spectroscopy

In Raman spectroscopy, a power laser sources of visible or infrared monochromatic radiation is irradiated upon the sample. During irradiation, the spectrum of the scattered radiation is measured at some angle with a suitable spectrometer. At very most, the intensities of Raman lines are 0.001% of the intensity of the source; as a result their detection and measurement are more difficult. Raman scattering effect can be visualized as the resultant effect from the collisions between

a stream of photons with molecules. If the collision is perfectly elastic, intact photons can be scattered and collected (Raylsigh scattering); however if the collision is inelastic, energy is exchanged between photon and molecule during collision. The scattered photons may gain or loss energy from the molecules (Raman scattering) [17, 18]. Radiation scattered with a frequency lower than that of the incident beam is referred as the Stokes scattering while that at higher frequency is called the anti-Stokes scattering.

## 2.5 Transmission electron microscopy (TEM)

### 2.5.1 The technique of transmission electron microscopy (TEM):

The microstructual image seen with transmission electron microscopy (TEM) is formed by an electron beam that passes through the specimen [19]. Details of internal microstructural features are accessible to observation. The contrasts in the image are produced by differences in beam scattering or diffraction produced between various elements of the microstructural or compositional analysis. Since solid materials are highly absorption to electron beams, a specimen to be examined must be prepared in the form of a very thin foil. This ensures transmission through the specimen of an appreciable fraction of the incident beam. The transmitted beam is projected onto a fluorescent screen or a photographic film so that the image may be viewed. Magnification approaching 1,000,000× are possible with transmission electron microscopy, which is frequently utilized in the study of grain size.

TEM provides a resolution on the order of 0.2nm. In order to achieve the highest quality image, the sample must be thinned down to less than 30-40nm. Therefore, TEM requires an intensive and difficult process of sample preparation.

Although multiple techniques are used in TEM sample preparation, ion beam milling provides the highest degree of accuracy in a specific area since the specimen may be viewed by secondary electron imaging while thinning.

In my research, a plane views TEM are used to give a "top-view" of my magnetic granular thin films and is frequently used to determine grain sizes and grain size distribution. The characterization of crystalline materials is measured by electron diffraction analysis.

TEM is generally the final analytical technique of a sample, due to the fact that TEM sample preparation is a destructive process. A thin sample not only lets higher percentage of electron beam transmit, but also reduces the beam heating to the sample and contaminate the TEM column.

### 2.5.2 Transmission electron microscopy (TEM) sample preparation

For a plan view TEM, there are two main processes for preparation, the first is mechanical polishing and the second is ion milling. The TEM sample preparation procedures are described in the following in details.

Plan View TEM sample preparation:

1. Cut square samples – carefully cut one piece of square from the sample with dimension of at least 3mmx3mm.

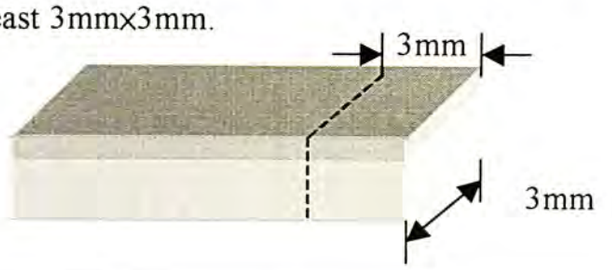

2. Glue the specimen with a copper ring – prepare an epoxy mixture (one part of hardener and seven to ten parts of epoxy) and then glue the top of 3mm copper ring to the face of the sample cleaned with IPA. Then, heat the specimen with the copper ring at 100℃ for 45 minutes in order to dry the epoxy.

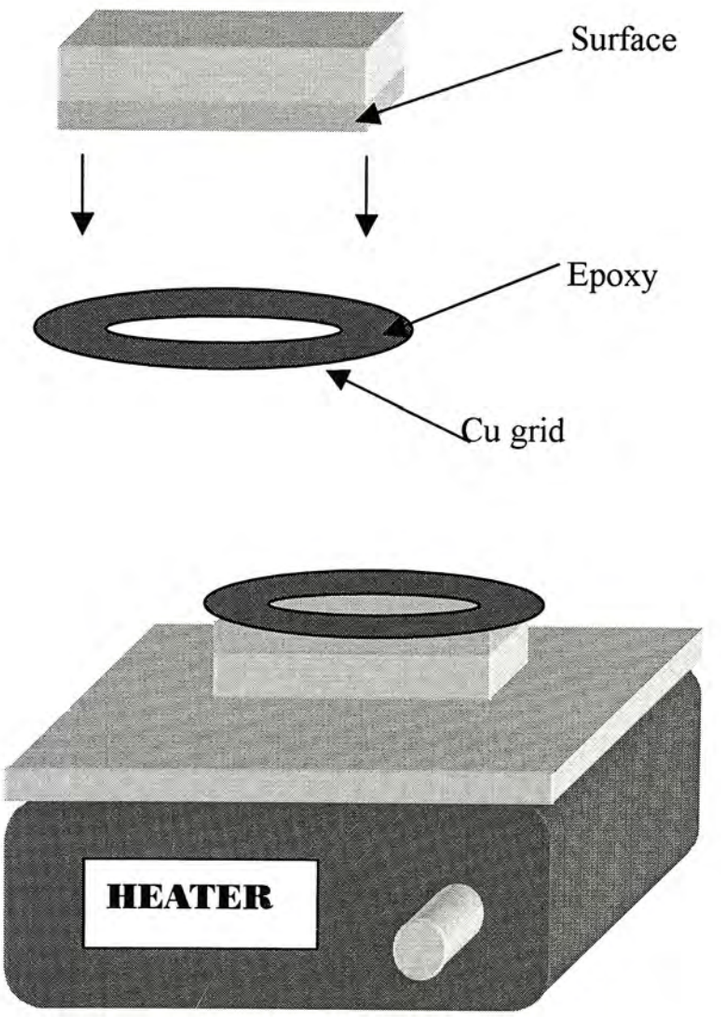


(heat about 100℃ for 45 minutes)

3. Glue the specimen on the sample holder of the polishing machine - put the copper ring with the sample on the sample holder of the polishing machine, and glue with melting wax. Make sure the melting wax fill to the middle of the copper ring so as to prevent the sample from crash in the final step.

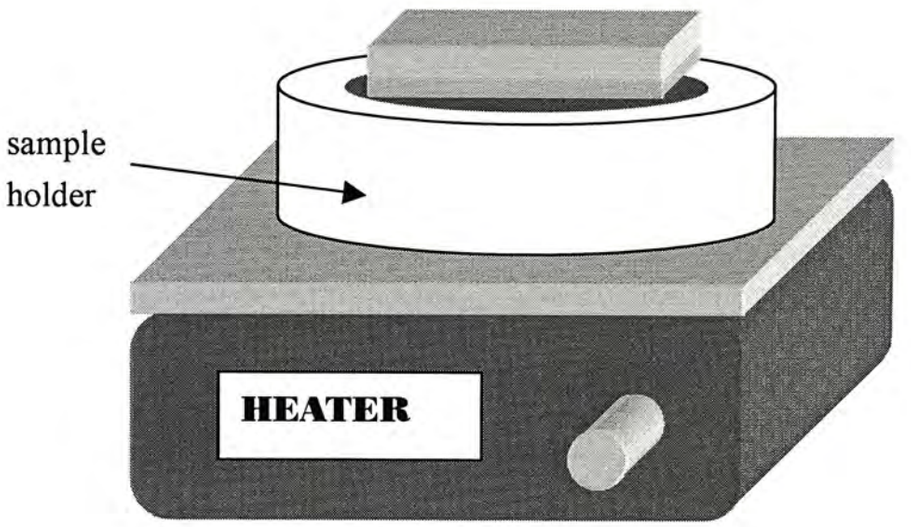


Heat (~60℃ 45 minutes)

4. Polish the specimen - screw the cool sample holder on the polishing tools. Carefully polish the specimen with different polishing carbon papers from GRIT No. 400 to 4000 in a high rotating speed of the polishing machine. Then the fine thinning with different diamond-papers of grit size from 3 $\mu$ m to 0.1 $\mu$ m. Carefully polish the sample until red transparent light can be seen through the sample on top of a light source. The rotation of the sample and the polishing machine are independently.

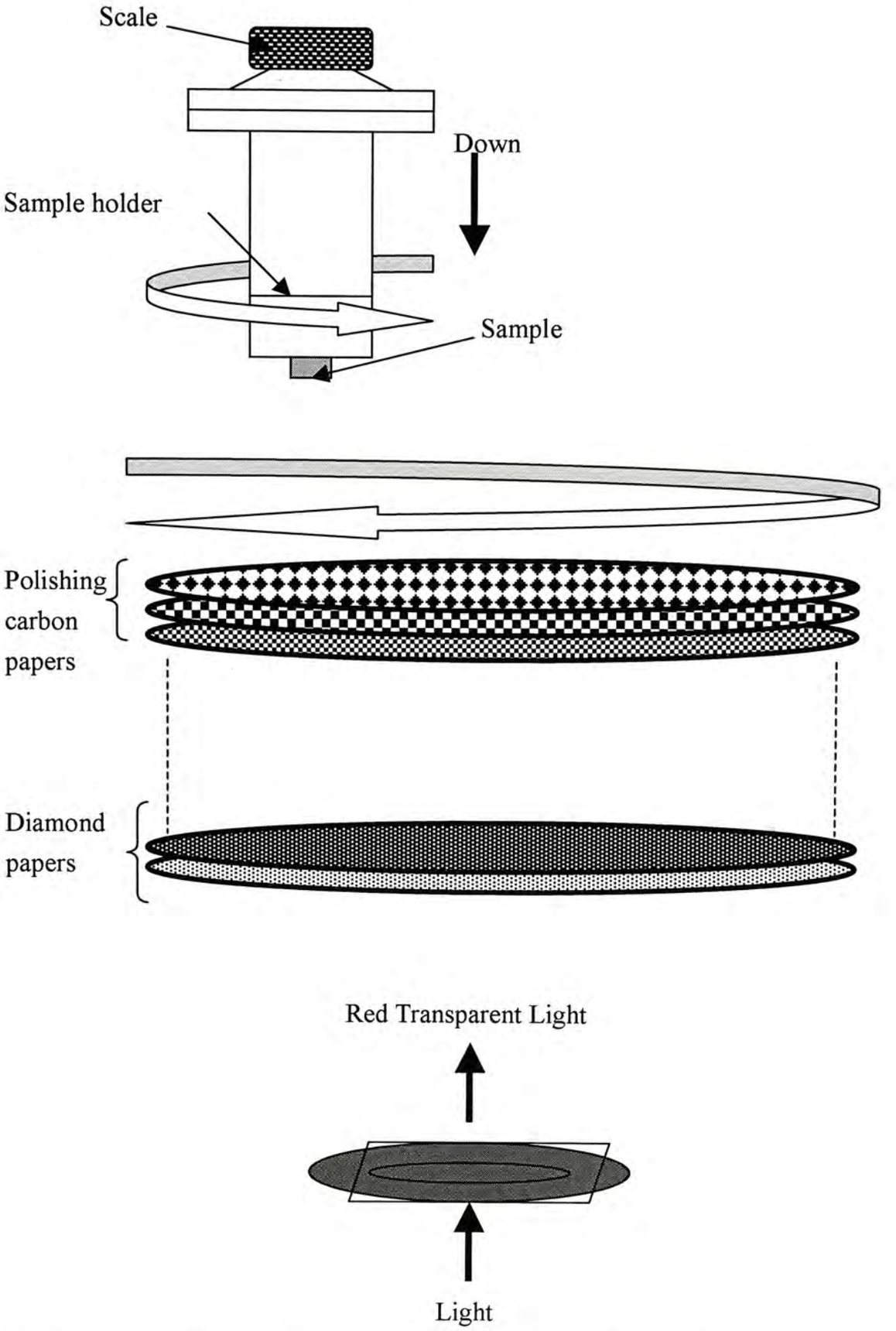


5. Focused Ion Beam Milling – clean the specimen with IPA after the wax is melt.

Load the sample with the copper ring into the ion-milling machine. The ion milling condition of an extraction voltage of 5keV and a beam current of 35 – 40 $\mu$A. Two small angles $\theta_o$ (4°) and $\theta_f$(2°) are used at the beginning and at last, respectively so as to obtain a larger area with the specimen for ion milling. Continue the ion milling process until a small hole at the center of the specimen is appeared.

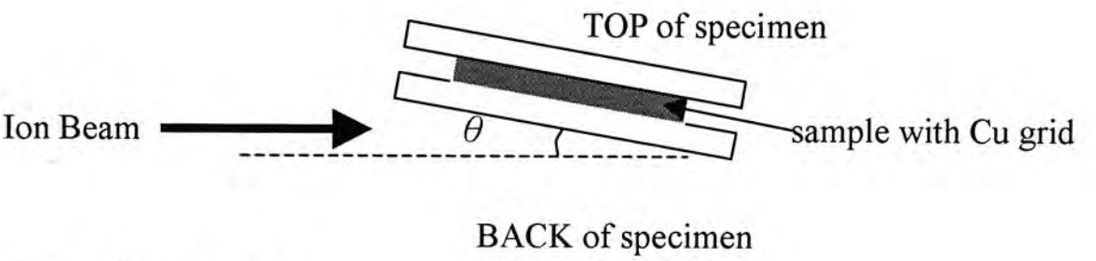


where $\theta_o$ (4°) and $\theta_f$(2°)

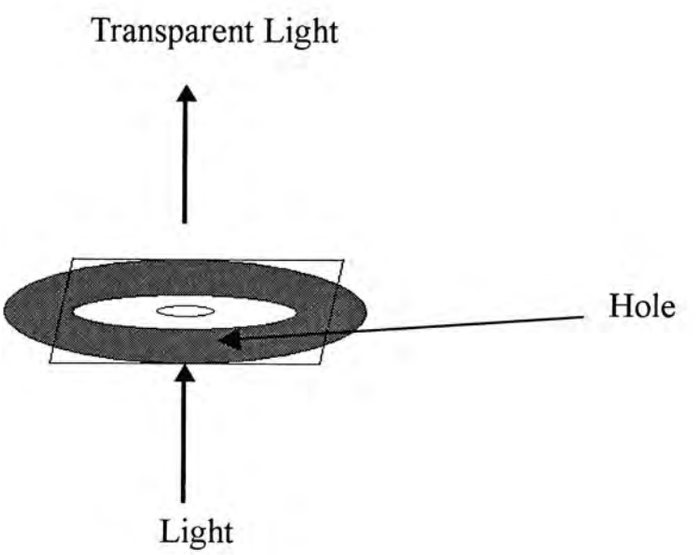


## 2.6 X-ray photoelectron spectroscopy (XPS)

### 2.6.1 The principle of XPS

X-ray photoelectron spectroscopy (XPS) is known as "Electron Spectroscopy for Chemical Analysis (ESCA)". If x-ray is used as the photon source to excite a sample surface and then the energy of those electrons ejected after photoemission process (photoelectrons) are detected and analysed, this technique is named as "X-ray photoelectron spectroscopy (XPS)" [20].

For XPS, Al K$\alpha$ (1486.6eV) or Mg K$\alpha$ (1253.6eV) are often the photon energies of choice. When a sample surface is irradiated with photons of energy h$\upsilon$, the energy of those electrons ejected after the photoemission process (photoelectrons) as shown in Fig. 2.7 are detected and analyzed by a concentric hemispherical analyzer (CHA). And the energy of the electrons are following the equation:

$$E_{KE} = h\nu - E_{BE} - \Phi(sample) \qquad \text{(Equation 2.2)}$$

where $E_{KE}$ is kinetic energy of the electron which will be detected and analyzed by the energy analyzer, $E_{BE}$ is the binding energy and $\Phi$(sample) is the work function of the sample.

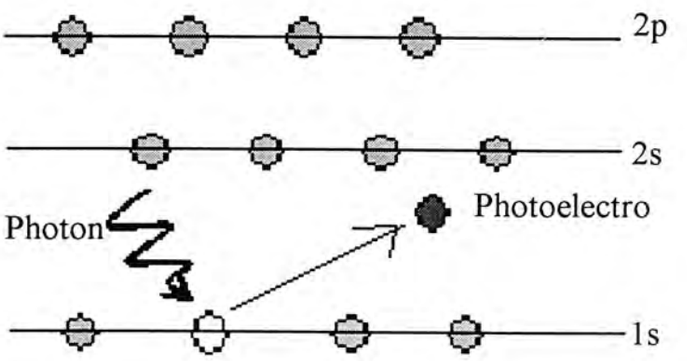


**Fig. 2.7** A incoming photon causes the ejection of the photoelectron. It is called XPS emission process for a model atom

The photoemission experiment found that the energy of ejecting electrons is directly proportional to the wavelength, $\upsilon$, of the photon source, instead of the intensity of photons. This photoelectric effect is in term of emission of the electrons from quantized energy levels, orbital of electrons.

Therefore, observing the peaks in the XPS spectrum, the elements in the sample can be defined.

### 2.6.2 Qualitative analysis of XPS (chemical shift)

The binding energy of a particular electron from a certain energy level in XPS is actually the energy required to remove the electron from that energy level to vacuum level. When the element is in different chemical states, its corresponding energy levels will be different, thus giving out photoelectrons at slightly different energy from those arisen from its elemental state. This energy shift is the so-called "chemical shift". As a result, such chemical shift information allows us to identify the chemical states of particular element.

## 2.7 Scanning probe microscopy (SPM)

### 2.7.1 The principle of atomic force microscopy (AFM)

Atomic Force microscopy (AFM) was the first instrument to produce real-space images of the surfaces with atomic resolution on non-conducting samples (Fig 2.8) [21]. An AFM consists of a scanner, a feedback loop and high voltage amplifiers. Besides it constitutes a special probe – cantilever and displacement detector. Both form a force sensor. A sharp tip with a couple of microns long is used. Its very end is

often about 20nm in diameter. The tip is located at the free end of the cantilever of 100 $\mu$ m to 200 $\mu$ m in length. When the tip engaged and then contacted to the surface of sample, the atomic interactions between the atoms on the tip and the sample cause the cantilever to bend, or deflect. Experimentally, a laser diode shined a laser beam on and reflected from the back of the cantilever into a position-sensitive photodiode (PSPD) detector. When the tip is scanned over the sample, the cantilever bends, the position of the laser beam on the detector shifts and thus a vertical displacement as small as 1nm can be measured. Therefore, the measured cantilever deflections allow a computer to produce a map of surface topography.

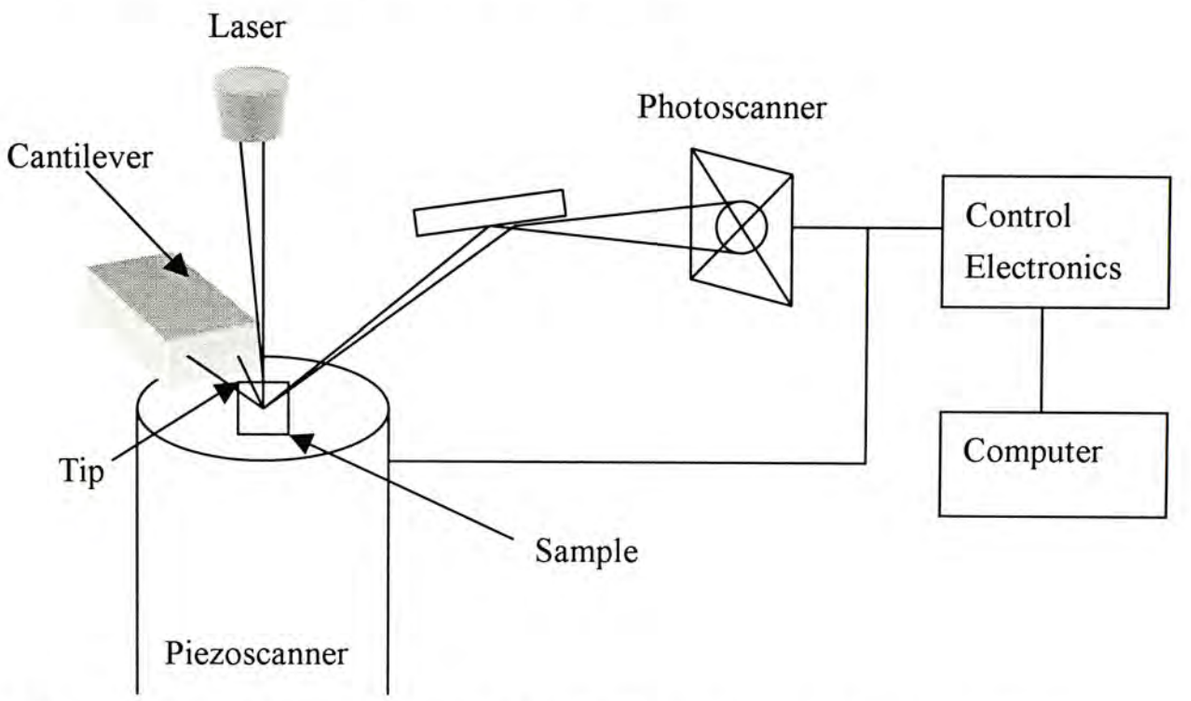


**Fig. 2.8** The schematic diagram of the main of a scanning probe microscopy

### 2.7.2 Tapping mode atomic force microscopy

In tapping mode AFM, the cantilever is driven to vibrate at its resonance frequency by a small piezoelectric element. The vibrating cantilever tip is brought closer to the sample so that at the bottom of its travel it just barely contacts, or "taps", the surface of sample. The cantilever's oscillation amplitude frequency or phase

varies when the tip contacts the sample surface. The force imparted onto the sample by the cantilever can be extremely small because small shifts in the vibration amplitude or phase can be easily detected. An image representing the surface topography can be obtained. The tapping mode AFM has lots of advantages, such as, high resolution, negligible surface impacts and sensitive of magnetic, chemical and electric forces [22].

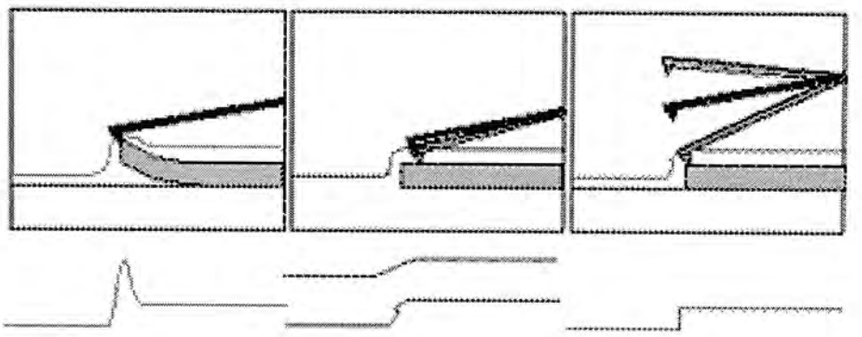

(a) (b) (c)

**Fig. 2.9** The comparison of (a) contact mode (b) non-contact mode (c) tapping mode scanning technique

Comparison of contact mode, non-contact mode and tapping mode scanning techniques (Fig. 2.9). Contact mode imaging (left) is heavily influenced by frictional and adhesive forces which can damage samples and distort image data. Non-contact imaging (center) generally provides low resolution and can also be hampered by the contaminant layer which can interfere with oscillation. Tapping mode imaging (right) eliminates frictional forces by intermittently contacting the surface and oscillating with sufficient amplitude to prevent the tip from being trapped by adhesive meniscus forces from the contaminant layer. The graphs under the images represent likely image data resulting from the three techniques.

### 2.7.3 Magnetic force microscopy (MFM)

Magnetic force microscopy (MFM) is a special type of tapping mode AFM, which can be used to observe the magnetic domain structure on the surface of a sample. The tapping cantilever used for MFM is equipped with a special tip. A Nanoscope III scanning probe microscope with a hard Co-alloy-coated silicon tip is used for this measurement. The tip first scans over the surface of the sample to obtain the topographic information. And then the lift mode is used in the second scan, as shown in Fig 2.10. Life mode, however, has advantages in both flexibility and reliability. Since the tip oscillates and follows a path predetermined by the topography, lift mode is not prone to "tip crashes". Also, frequency, phase or amplitude shifts can be recorded as desired. Small lift heights (<50 nm) exploit the full potential of MFM for high-resolution imaging. The weak magnetic features may not be resolved by high lift scanning. The surface topography will affect the MFM image if the smaller lift height and large surface roughness are happened.

The magnetic interaction of the tip and the local sample surface is measured at this constant scan height. When there is no magnetic force, the cantilever has a resonance frequency $f_o$. The influence of magnetic force is measured using the principle of force gradient detection. The shifts in the resonance frequency tend to very small, typically in the range of 1-50 Hz for cantilever having a resonance frequency $f_o$ of 10-100kHz. Phase detection and frequency modulation produce results that are generally superior to amplitude detection.

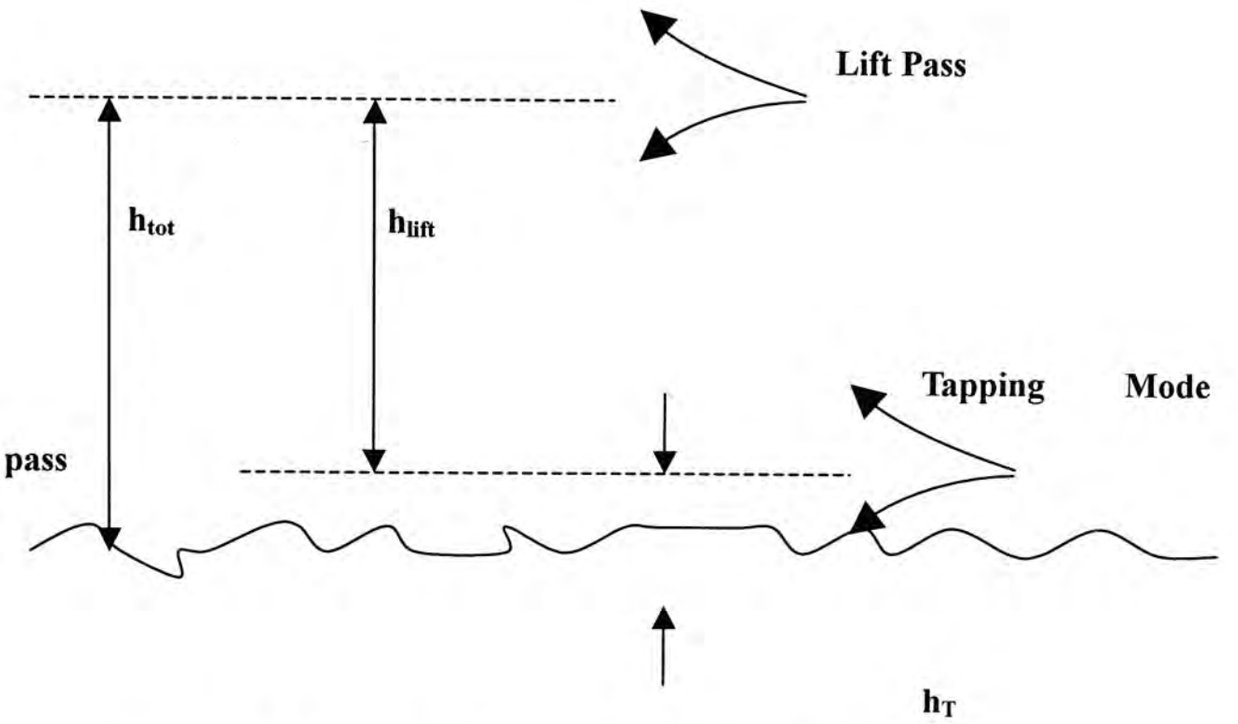


**Fig. 2.10** Schematic of the operation of Magnetic Force Microscopy

$h_T$ : average tip-sample distance in tapping mode.

$h_{lift}$ : the lift scan height.

$h_{total}$: the total tip-sample distance is the sum of the $h_T$ and $h_{lift}$.

## 2.8 Vibrating sample magnetometer (VSM)

The vibrating sample magnetometer (VSM) offers a user a high sensitivity measurement instrument. The VSM may be supplied with a number of options of magnet and operation of the magnet.

### 2.8.1 The principle of VSM operation

All materials acquire a magnetic moment when placed in a magnetic field.

The magnetic moment per unit volume is known as the magnetization. The VSM uses an induction technique for the measurement of magnetic moment by detecting an a.c. field produced by an oscillating sample moment.

The technique is very simple to describe. The sample is attached to the lower end of a rigid rod and makes to oscillate vertically, typically over 1-1.5mm and frequencies 40-80 Hz. If the sample is magnetized, the oscillation will induced an a.c. signal in a set of suitably placed pick-up or sense coils. The amplitude of this signal is proportional to the magnetic moment of the sample (Fig. 2.11).

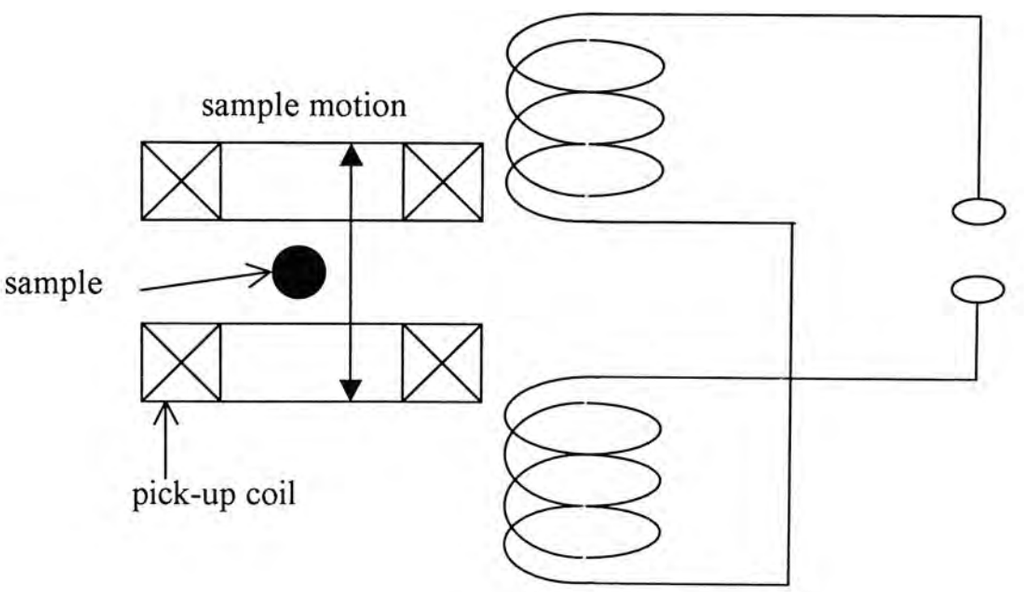


**Fig. 2.11** The schematic diagram of signal generator

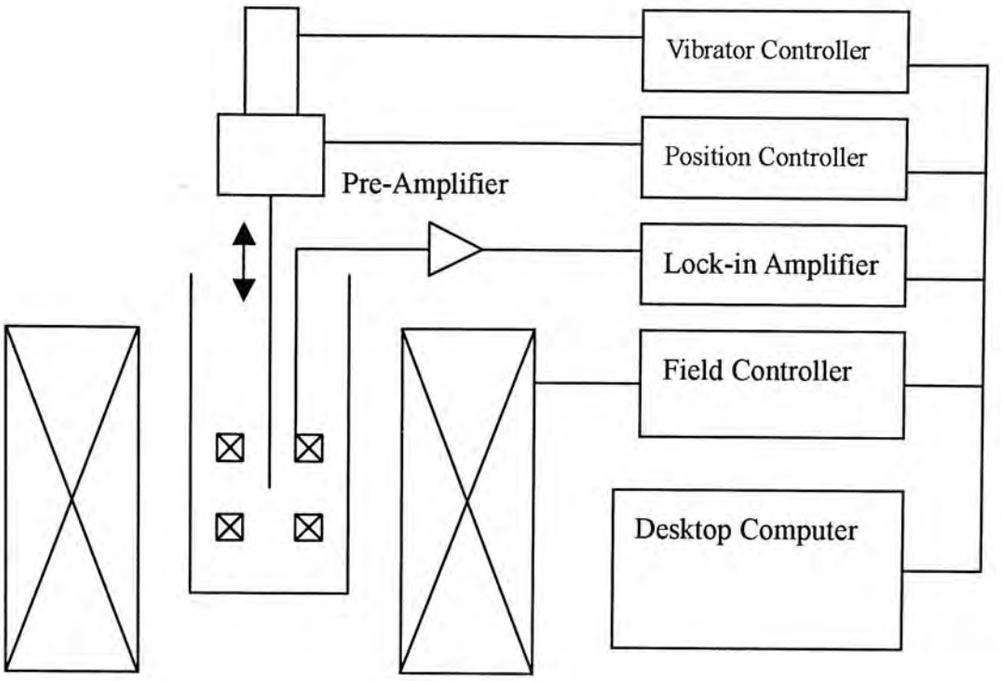


**Fig. 2.12** The block diagram of the individual components of the VSM system

### 2.8.2 Useful of the pick up coils

The pick up coils are usually connected as a gradient pair such that the induced emfs in each coil add. The lock-in amplifier is tuned to the vibration frequency using a reference signal from the vibrator controller and detects the in-phase voltage from the sense coils.

The applied field and vibrating frequency are varied under computer controlled (Fig. 2.12). Finally, the computer records the Lock-in Amplifier (LIA) voltage data as a function of field or time.

### 2.8.3 M-H Loop

For the M-H loop (Fig. 2.13), we should determine the saturation magnetization $M_S$, coercivity $H_c$, and the ratio of the remanence to the saturation magnetization $M_r/M_S$.

As the magnetic field H is reduced from the saturation magnetization the M-H loop does not retrace its original path from some value of magnetic field $H_o$. A hysteresis effect is produced. When H reduced to zero (H=0), the $M=M_r$, that is called remanence. The material remains magnetized in the absence of an external H field. In order to reduce the magnetization within specimen to zero, the H-field of magnitude $-H_c$ must be applied in a direction opposite to that of the original field; $H_c$ is called coercivity.

There are two performing M/H loops in the VSM application dialog. The first one is standard loop which is for most magnetic measurement. The second one is special loop. It can be used when a non-standard M/H loop is required, such as which is not centred on zero.

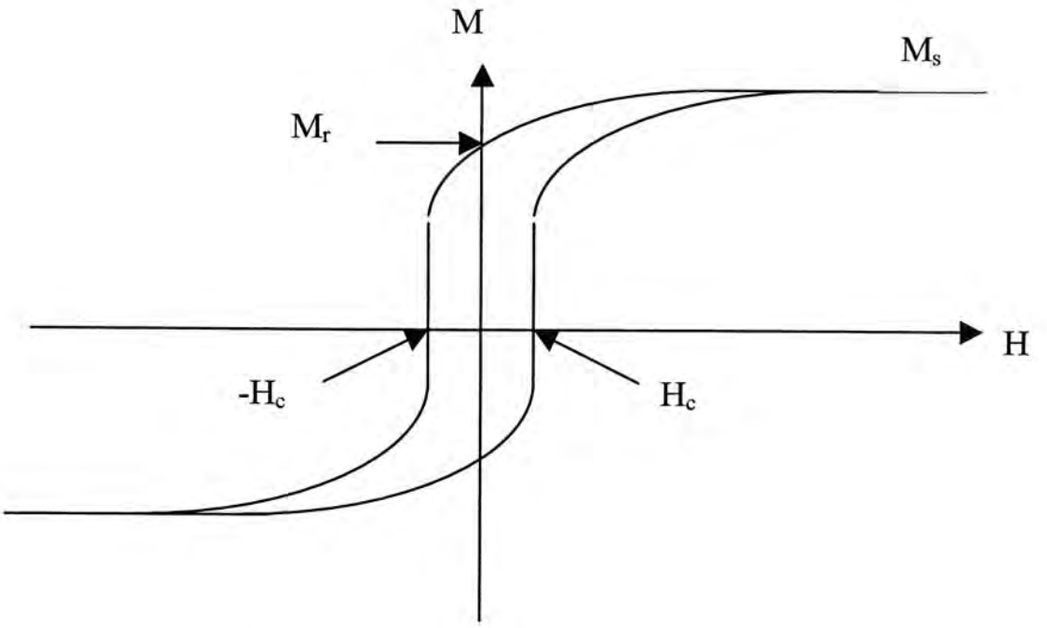


**Fig. 2.13** The hysteresis loop of the ferromagnetic material sample

## 2.9 Four-contacts technique

The resistivities of the samples were measured using the four-contacts technique. The temperature is varied during the measurement. Four silver (Ag) contact pads in a line were evaporated on the samples surface by thermal evaporation (Fig. 3.14). The thickness of the Ag pads is about 300nm. The measurement system is computer controllable. The schematic of the resistivity measurement system is shown in Fig. 2.15. The temperature can be stabilized and adjusted by a CTI-cryostat combined with a LakeShore temperature controller. An Adventest TR6143 DC voltage/current is used to provide a constant current through the sample between the contacts 1 and 4, as shown in Fig. 3.14. A typical current of 10mA was used in this work. An HP 34401A digital multi-meter is used to measure the voltage drop between the contacts 2 and 3. In this work, the resistivity was measured from 30K to 300K in steps of 10K. At each pre-set temperature, a waiting time is set to 3 minutes to allow the temperature to be stabilized before the measurement performed.

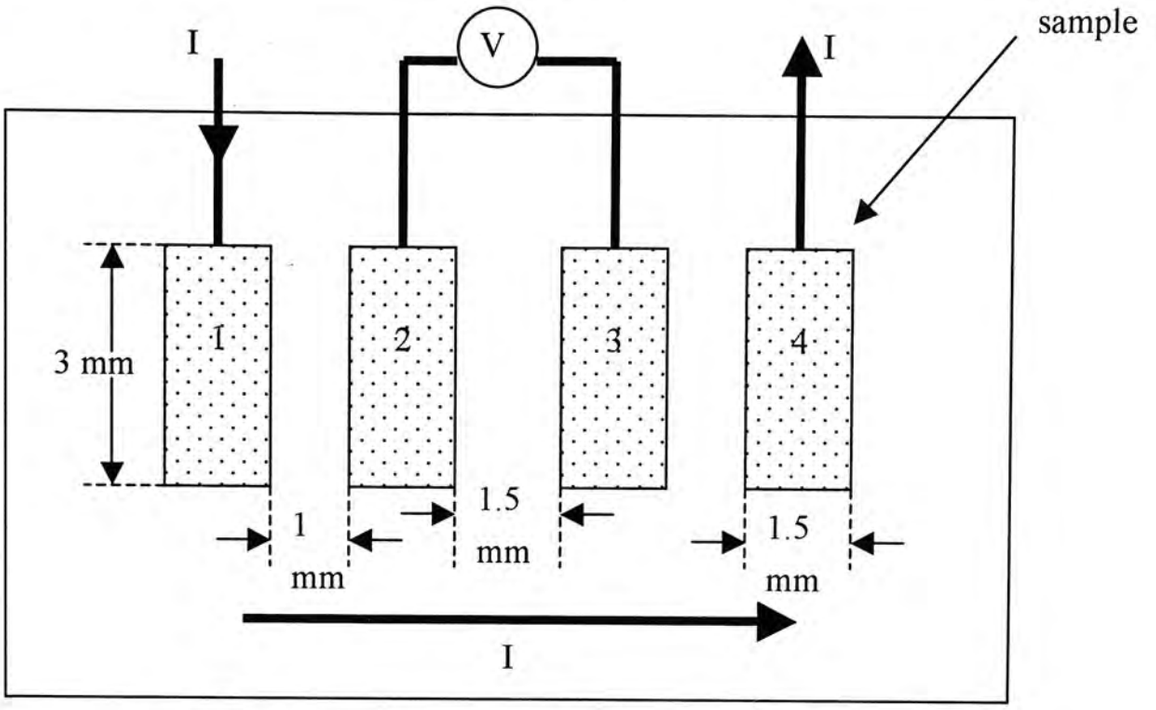


**Fig. 3.14** The schematic of the four-contacts technique

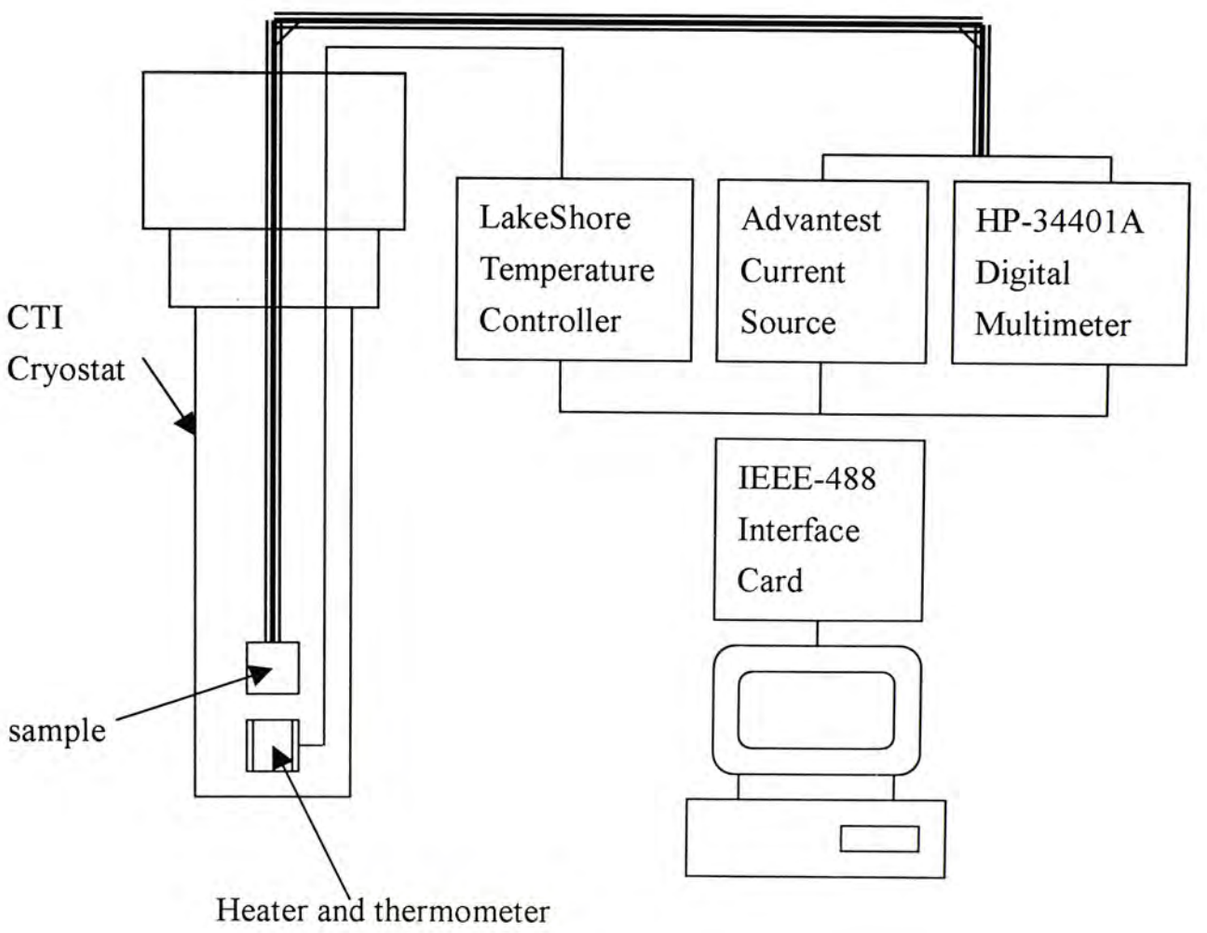


**Fig. 3.15** The schematic diagram of the resistivity measurement

# Chapter 3 Characterization of co-deposited Co-C samples

## 3.1 Introduction

Granular thin films of $Co_xC_{1-x}$ of various compositions were prepared on thermally grown $SiO_2$ layer on (100) Si substrates using a pulsed filtered cathodic arc co-deposition system. The thermally grown oxide on silicon was about 100nm. Pure cobalt and graphite sources were used. For the carbon source, a 65° and 45° double bent magnetic filter was used in order to filter the carbon macroparticles. The substrate is placed at the bi-sector of the cobalt and carbon sources. The composition of the deposited films is controlled by adjusting the arc discharge conditions and the pulse sequence of the respective sources, and by monitoring separately the total charges arriving at the substrate and the sample holder from the respective sources. The cobalt composition varies from 13 at.% to 49 at.% in our batch of samples. Then the as-deposited films were annealed in vacuum ($<10^{-3}$ Pa) for one hour at various temperatures ranging from 200℃ to 600℃.

The arc sources were operated in a pulsed mode with a pulse length of 2.5ms. The pulse sequence was controlled by the computer. The pressure in the chamber was less than $4\times10^{-4}$ Pa.

**Pulsed filtered cathodic arc co-deposition system condition:**

| | Carbon | Cobalt |
|---|---|---|
| Bias | 107V | 140V |
| Focus | 80 $\mu$ A | 135 $\mu$ A |
| Arc | 120V | 150V |
| Trigger | 125V | 155V |
| Deflect | 125 $\mu$ A | 150 $\mu$ A |

The actual composition and the thickness of the deposited films were determined by non-Rutherford backscattering spectrometry (NRBS). The structural evolution of the films against thermal annealing were analysed by x-ray diffraction (XRD) and Raman spectroscopy. The surface morphology was studied by atomic force microscopy (AFM) and the magnetic domain structures were studied by (MFM). The magnetic properties were measured by a vibrating sample magnetometer (VSM).

## 3.2 Results and discussion

### 3.2.1 NRBS measurement

The composition and thickness of the $Co_xC_{1-x}$ films were determined by non-Rutherford backscattering spectrometry (NRBS). The NRBS experiments were performed with a 2MV tandem accelerator at a resonance mode for the carbon atoms, using a beam of 3.5 MeV $^4He^{++}$ ions at an incident angle of 7° to the normal line of the film plane and with the backscattered $He^{++}$ ions detected at a scattering angle of 170°. The schematic structure of the Co-C samples is shown in Fig 3.1. Typical NRBS spectra of several Co-C samples of various compositions as indicated are shown in Fig. 3.2. The spectra were simulated by the software SIMNRA [15] for each sample to determine the composition and thickness. The simulation results are shown as lines in Fig. 3.2 where as the experimental data are presented as symbols.


**Fig 3.1** The schematic structure of the Co-C sample prepared by filtered pulsed cathodic arc co-deposition system

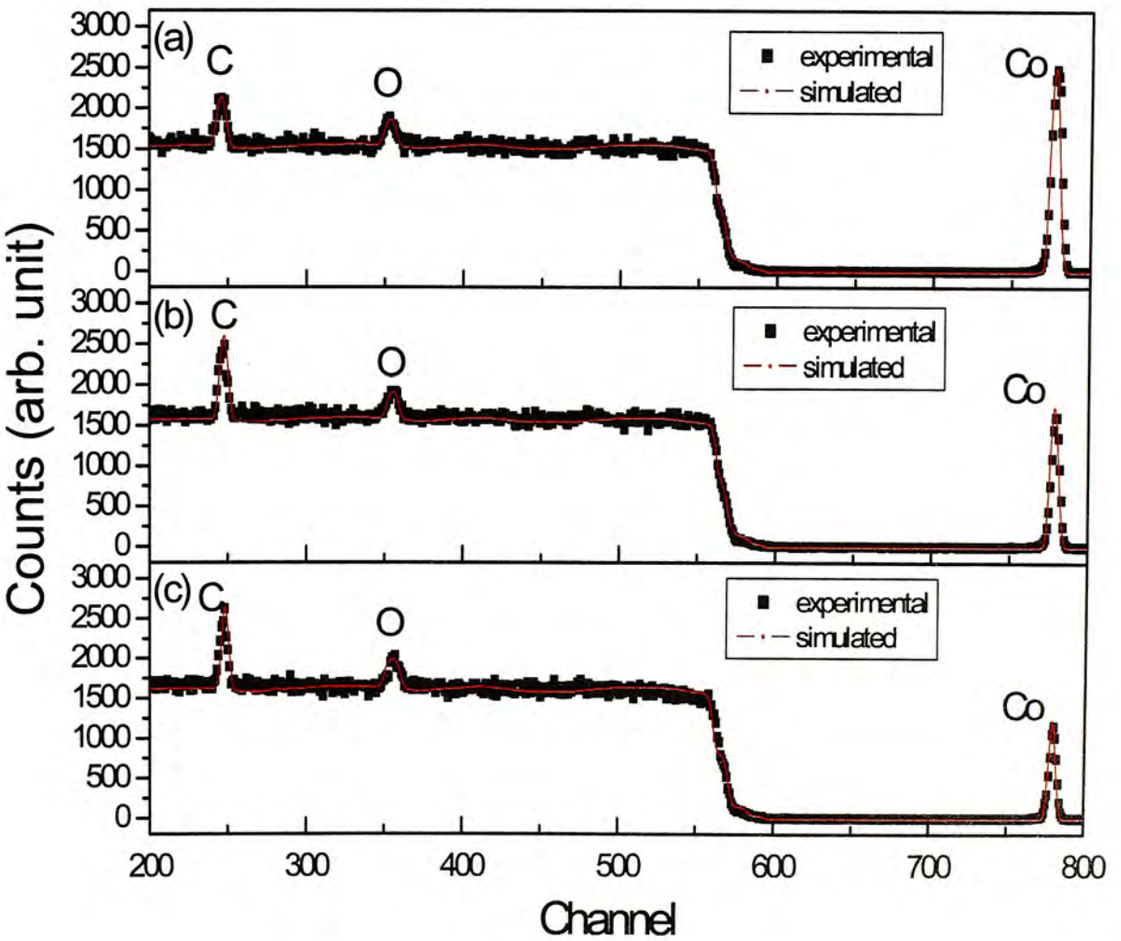


**Fig 3.2** NRBS spectra of the $Co_xC_{100-x}$ films. The experimental and simulation results of (a) $Co_{49}C_{51}$, (b) $Co_{70}C_{30}$ and (c) $Co_{13}C_{87}$ are shown

The NRBS spectra reveal that the composition of the Co-C films is uniform throughout the layer. By assuming a uniform composition and using the SIMNRA 4.4 software, the composition of the batch of Co-C samples prepared in this study was determined to be $Co_{49}C_{51}$, $Co_{43}C_{57}$, $Co_{36}C_{64}$, $Co_{33}C_{67}$, $Co_{30}C_{70}$, $Co_{23}C_{77}$ and $Co_{13}C_{87}$. The thicknesses of the Co-C samples were determined to be about 30 nm. The fitting accuracy for the composition and the thickness are about 1% and 1 nm respectively.

### 3.2.2 X-ray diffraction

The microstructure of the $Co_xC_{1-x}$ films was studied by glancing incidence x-ray diffraction (XRD). The XRD patterns of the as-deposited and annealed $Co_{49}C_{51}$ films are shown in Fig 3.3. The as-deposited film was found to be amorphous. The XRD pattern reveals that small grains of hexagonal close packed (hcp) crystalline Co are presented in the films after annealing at 500℃ and 600℃. By using Scherrer's formula (Equation 2.1) to be (101) lines, the hcp-Co crystallite sizes are estimated to be about 8nm and 12nm in the $Co_{49}C_{51}$ films after annealing at 500℃ and 600℃, respectively. Note that the diffraction intensity is weak because the films are only of about 30nm thick with a Co concentration of 49 at.%.

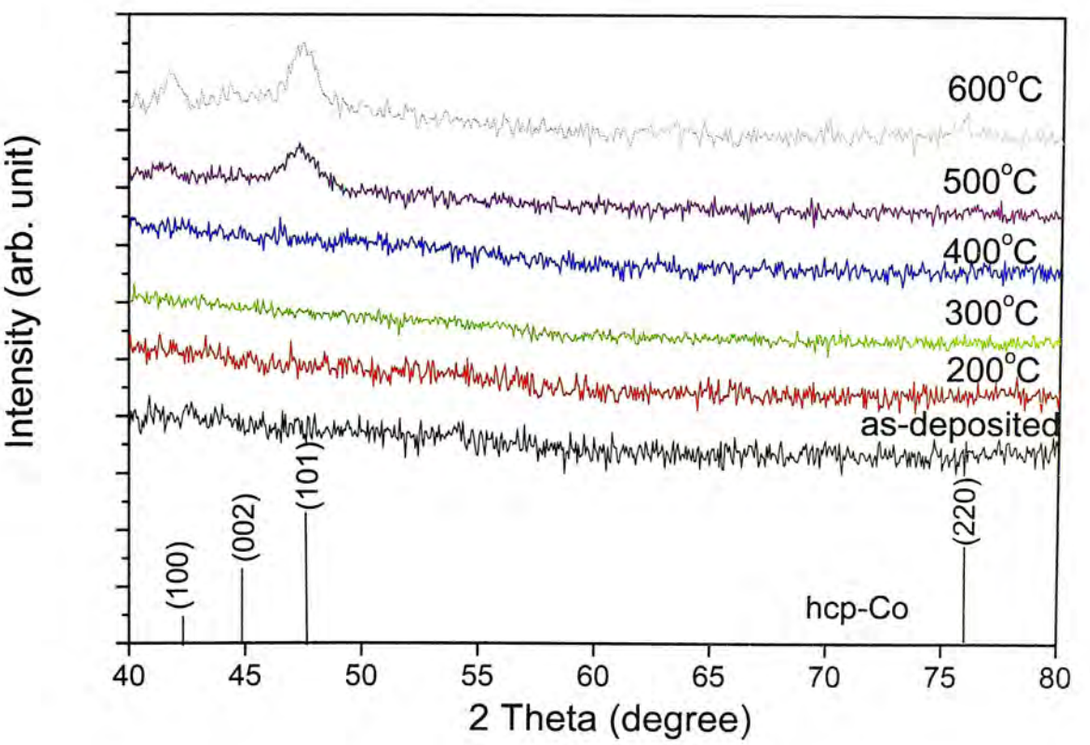


**Fig.3.3** XRD pattern for the as-deposited and annealed $Co_{49}C_{51}$ films

The XRD patterns of as-deposited, 200℃ to 600℃ annealed $Co_{30}C_{70}$ films are shown in Fig. 3.4. Similar to the $Co_{49}C_{51}$ samples, the as-deposited to 400 ℃ annealed films were found to be amorphous. After annealing at 500℃ and 600℃, the XRD pattern of these samples show that small grains of hexagonal close packed (hcp) crystalline Co are presented. The grain size of the 600℃ annealed film estimated by Scherrer's formula using the (100) line from the XRD pattern is about 10nm. The microstructure of our samples according to pervious work of our lab [23], are consistent with those of a study of the crystallization properties of co-sputtered amorphous Co-C alloy using a combination of *in situ* transmission electron microscopy and differential scanning calorimetry [24]. In that study, it was reported that for films with Co content smaller than about 60 at.%, the Co grains will become crystallized while the carbon will remain amorphous after annealing at about 350℃.

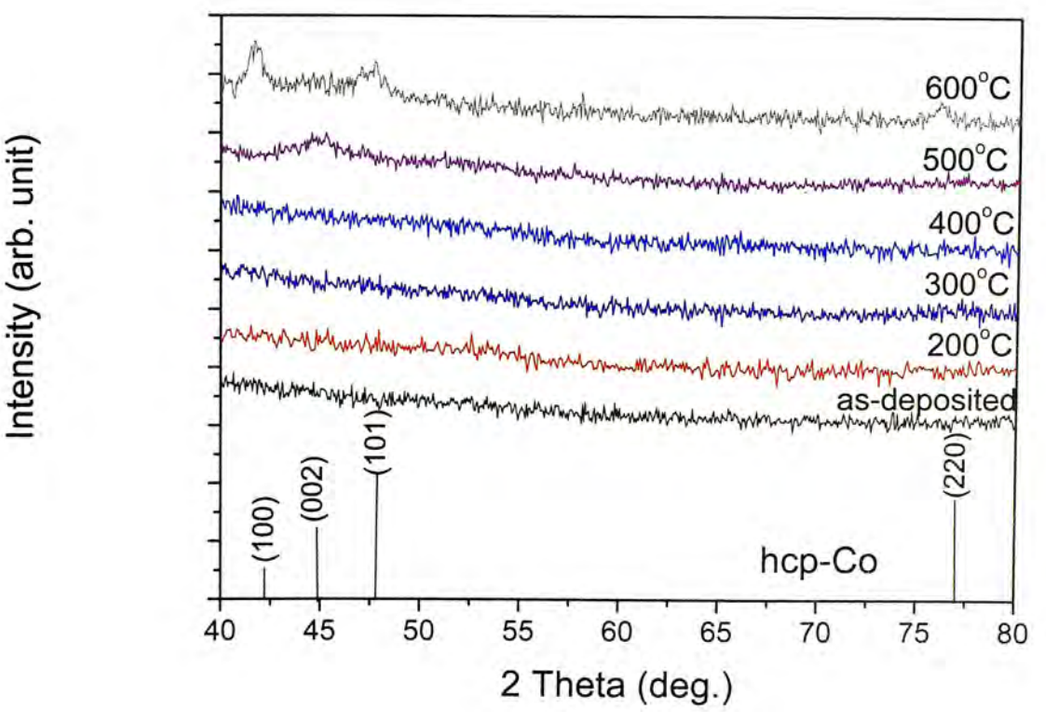


**Fig.3.4** XRD pattern for the as-deposited and annealed $Co_{30}C_{70}$ films

As shown in Fig. 3.5, for the $Co_{13}C_{87}$ sample, no peak can be observed in the XRD patterns both for the as-deposited and annealed samples because the Co content is quite low.

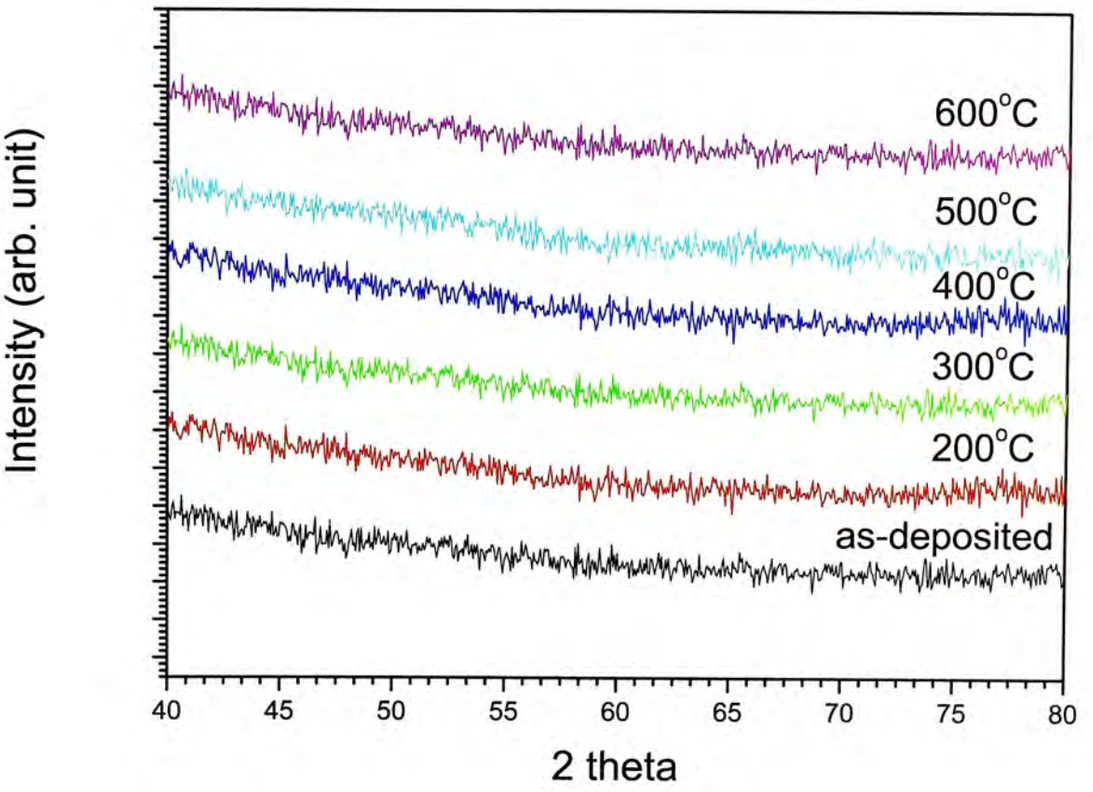


**Fig.3.5** XRD pattern for the as-deposited and annealed $Co_{13}C_{87}$ films

### 3.2.3 Raman spectroscopy

The phase transition of carbon was studied by Raman spectroscopy. Typical Raman spectra of the Co-C films of different compositions at different annealed temperature are shown in Fig. 3.6. The 514.5 nm line of an Ar laser was used for the Raman spectroscopy. All spectra are fitted using a skewed Lorentzian peak centered at about 1560-1585 $cm^{-1}$ (i.e., the "G" peak of the first-order Raman

spectrum of polycrystalline graphite) together with a second Lorentzian peak centered at about 1360-1380 $cm^{-1}$ (i.e., the "D" peak of polycrystalline graphite) and a linear background.

For those as-deposited samples, the presence of the "G" and "D" peaks is evident though their intensities are weak. For the 500℃ and 600℃ annealed samples, the "G" and "D" peaks' intensities are strong. This indicates that the crystal size of graphite-like carbon in these films increased with annealing temperature.

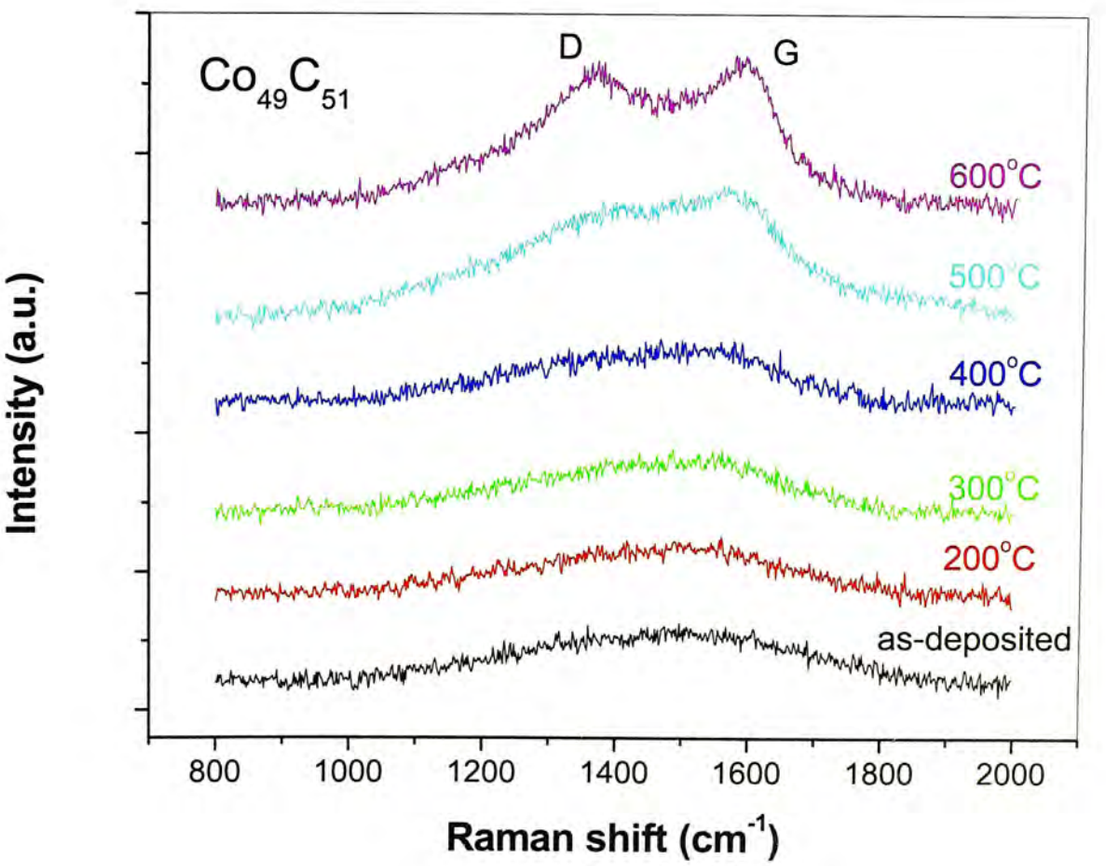


(a)

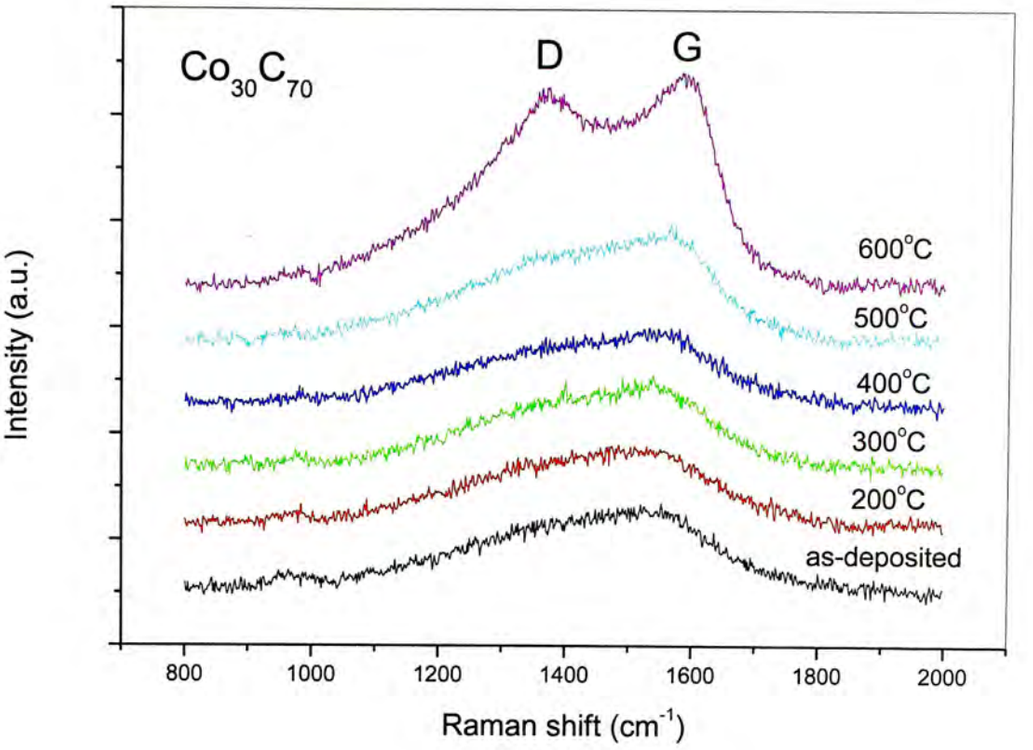


(b)

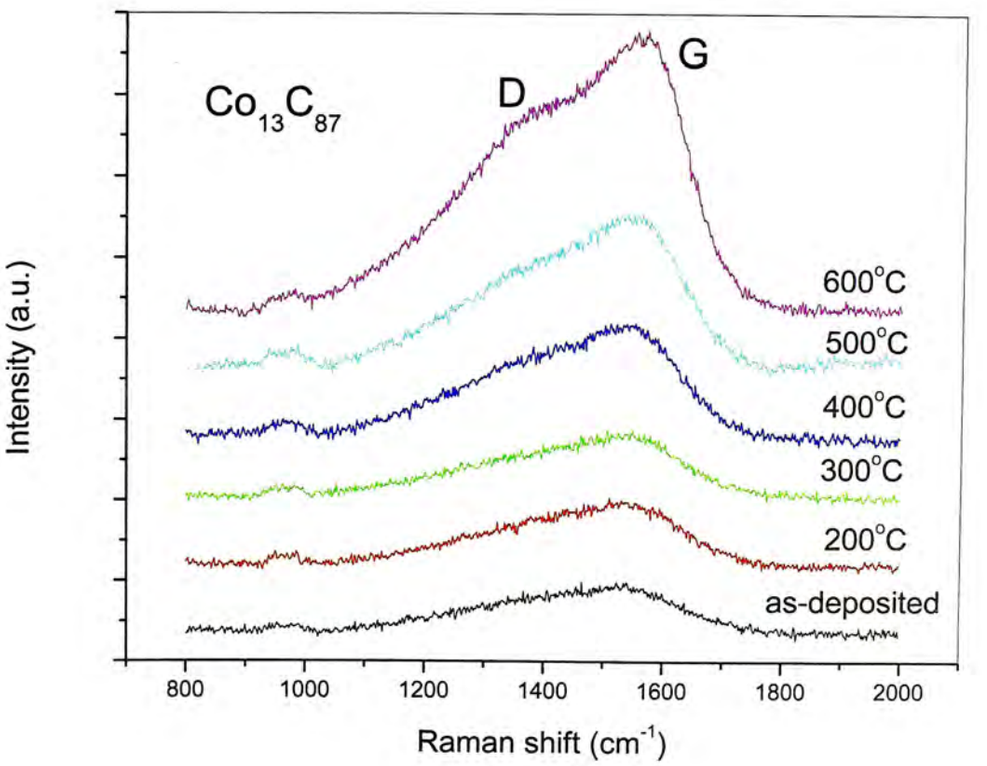


(c)

**Fig. 3.6** The Raman spectra of (a) $Co_{51}C_{49}$, (b) $Co_{70}C_{30}$ and (c) $Co_{87}C_{13}$ samples, as-deposited and after annealing at various temperature as indicated.

It was found that the Raman spectra of these samples can be deconvoluted into two components, one Lorentzian and the other modified Lorentzian with a skewed Breit-Wagner-Fano (BWF) lineshape described by

$$I(\omega) = \frac{I_o[1+2(\omega-\omega_o)/Q\Gamma]^2}{1+[2(\omega-\omega_o)/\Gamma]^2}$$

where $I(\omega)$ is the intensity as a function of frequency, $I_o$ the maximum peak, $\omega_o$ and $\Gamma$ the peak position and full mean half maximum (FMHM), respectively, and Q is the BWF coupling coefficient.

One example of suc deconvolution is thrown in Fig. 3.7, where the component peaked at ~1361cm$^{-1}$ (the 'D' peak) is Lorentzian and that peaked at 1585cm$^{-1}$ (the 'G' peak) is of BWF lineshape. The deconvolution was performed using a commercial available software Peakfit [25].

By fitting the spectra, we can see the variation of the intensity ratio of the D and G peaks ($I_D/I_G$) with annealing temperature and the film composition. Such plots of the ratio $I_D/I_G$ against annealing temperature for these Co-C films with various composition are shown in Fig. 3.8 The figure shows that for the as-deposited films, the $I_D/I_G$ ratios are between 0.24 and 0.63 and increases with the Co content. The $I_D/I_G$ ratio changes little with annealing temperature up to 600℃ when the Co concentration of the films is lower than approximately 30 at.%. This indicates the thermal stability of carbon in these films. When the Co content is equal to or larger than 30 at.%, the increase of the $I_D/I_G$ ratio with annealing temperature becomes significant above 300℃ and the appearance of the 'D' peak, which is associated with the presence of graphitic clusters in the film [26], because more and more

evident in the Raman spectra. For a fully amorphous diamond like carbon film, $I_D$ approaches to zero. The low $I_D/I_G$ ratio indicates the presence of an amorphous carbon-like structure in the films. An increase in the $I_D/I_G$ ratio could be an indication of an increase in the size of the graphitic clusters in the film.

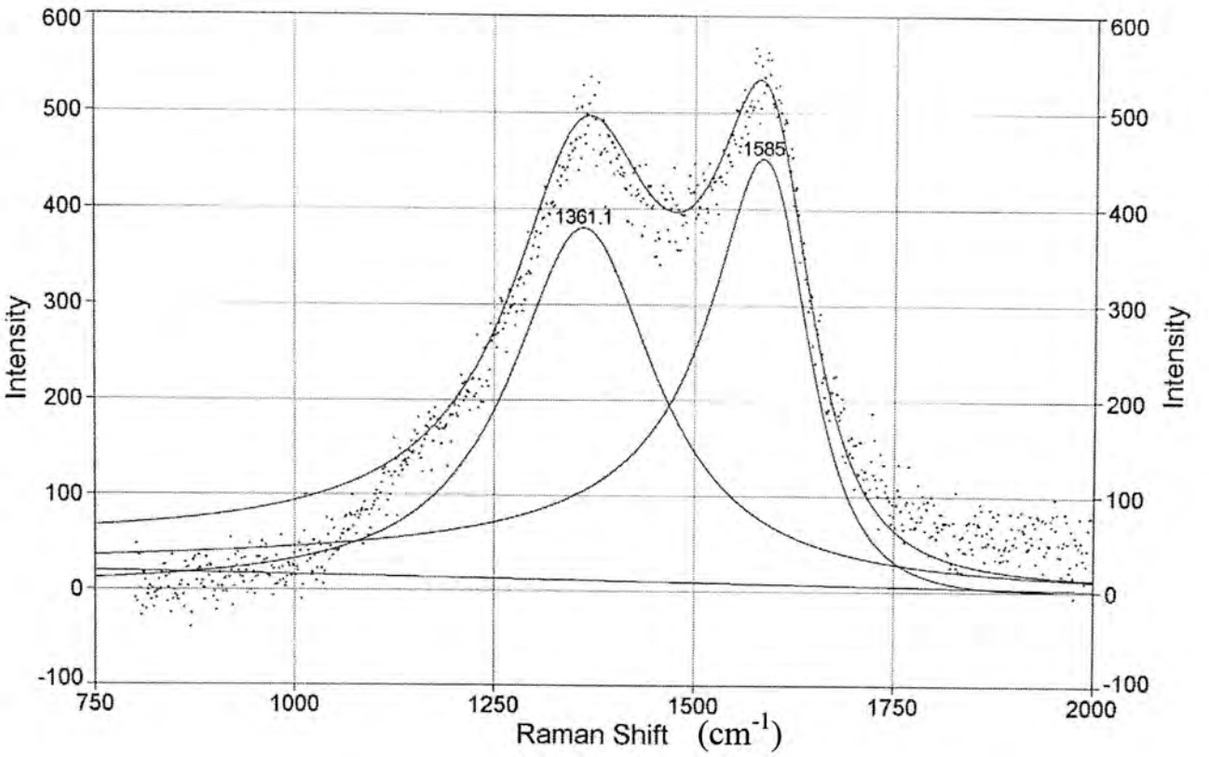


**Fig. 3.7** An example showing the deconvolution of the Raman spectra. This particular sample is a $Co_{49}C_{51}$ sample annealed at 600℃

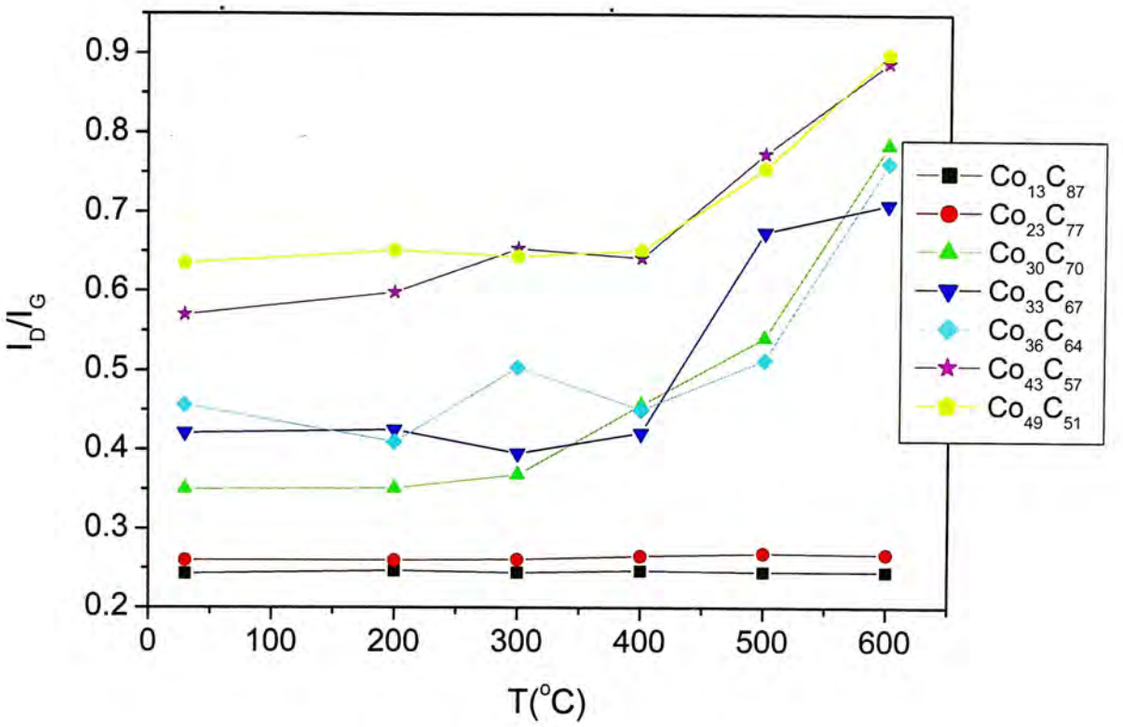


**Fig. 3.8** The ratio $I_D/I_G$ against annealing temperature for Co-C films with various composition

### 3.2.4AFM and MFM measurements

#### 3.2.4.1 AFM results

The surface morphology of the co-deposited Co-C films was observed by AFM and the magnetic domain structures of the co-deposited samples were studied by a Nanoscopy III scanning probe microscope (Digital Instruments Inc.) with a Co-alloy-coated tip using tapping and lifting modes. During the magnetic domain measurement, the tip is lifted to a height of 20 nm to prevent the influence of the surface morphology.

In Fig 3.9, we show the tapping mode AFM micrographs for the sample of a $Co_{49}C_{51}$ film with a thickness of 30 nm, as-deposited and after annealing at various temperatures. The as-deposited and 200℃- 400℃ annealed samples show a very smooth surface morphology. This is believed to be associated with the amorphous structure of these films. After annealing at higher temperatures, the surface of the $Co_{49}C_{51}$ films become rougher and rougher. The reason is that the Co hexagonal close-packed (hcp) phase has been crystallized in these samples and the grains have grown up. This is consistent with the XRD results especially for the samples annealed at 500℃ and 600℃ the crystallization of the Co hcp phase is clearly evident.

The root-mean-square roughness of the corresponding samples has been summarized in Fig 3.10.

(a)

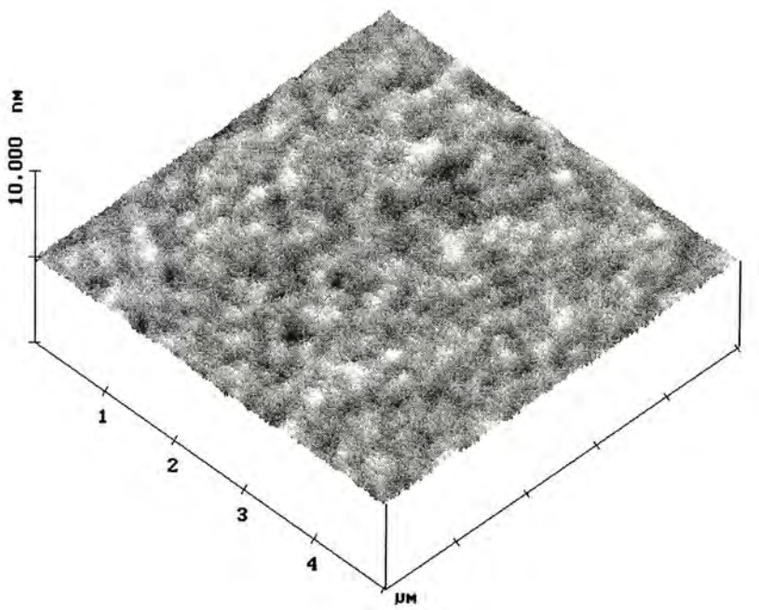

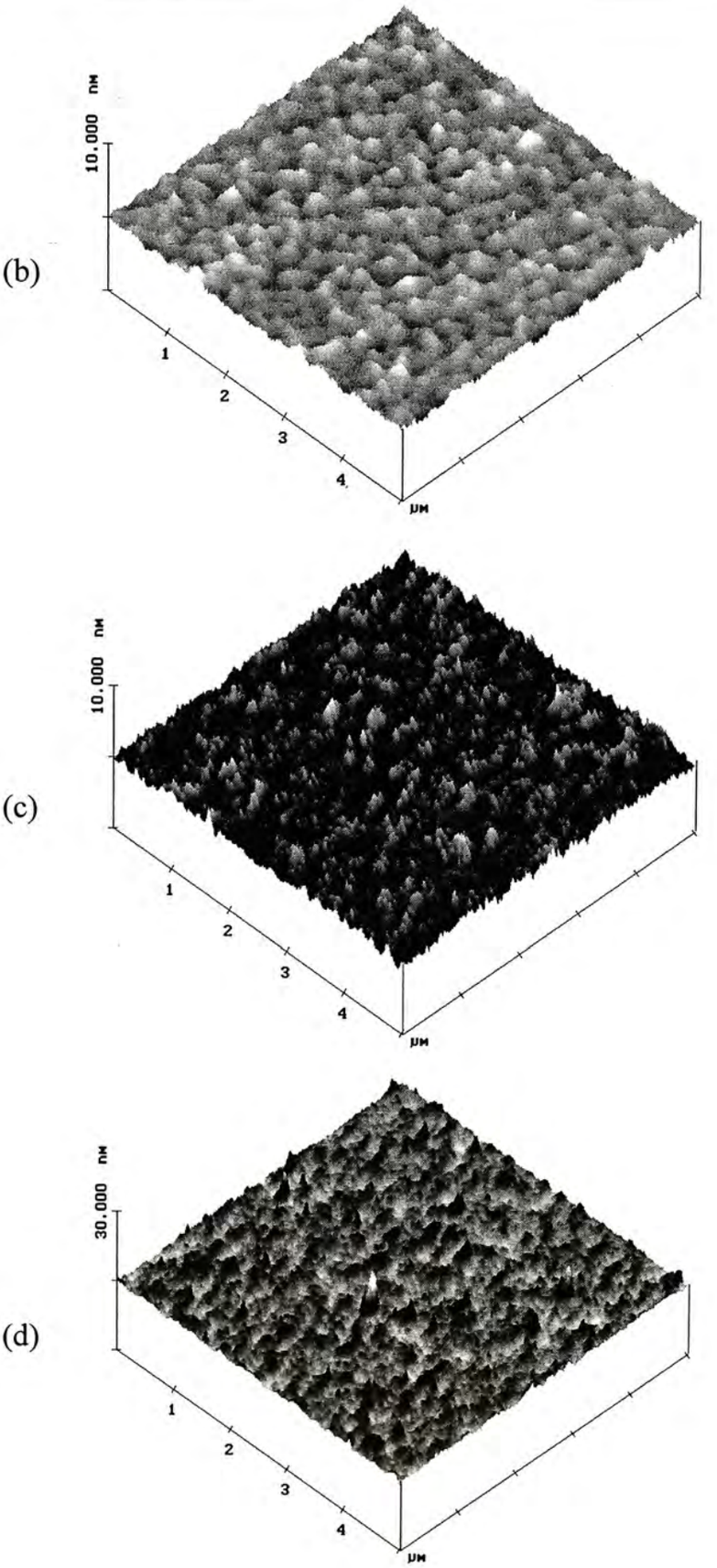


**Fig. 3.9** Tapping mode AFM micrographs for the co-deposited with $Co_{49}C_{51}$ sample, (a) as-deposited; (b) 200℃ annealed; (c) 500℃ annealed; (d) 600℃ annealed

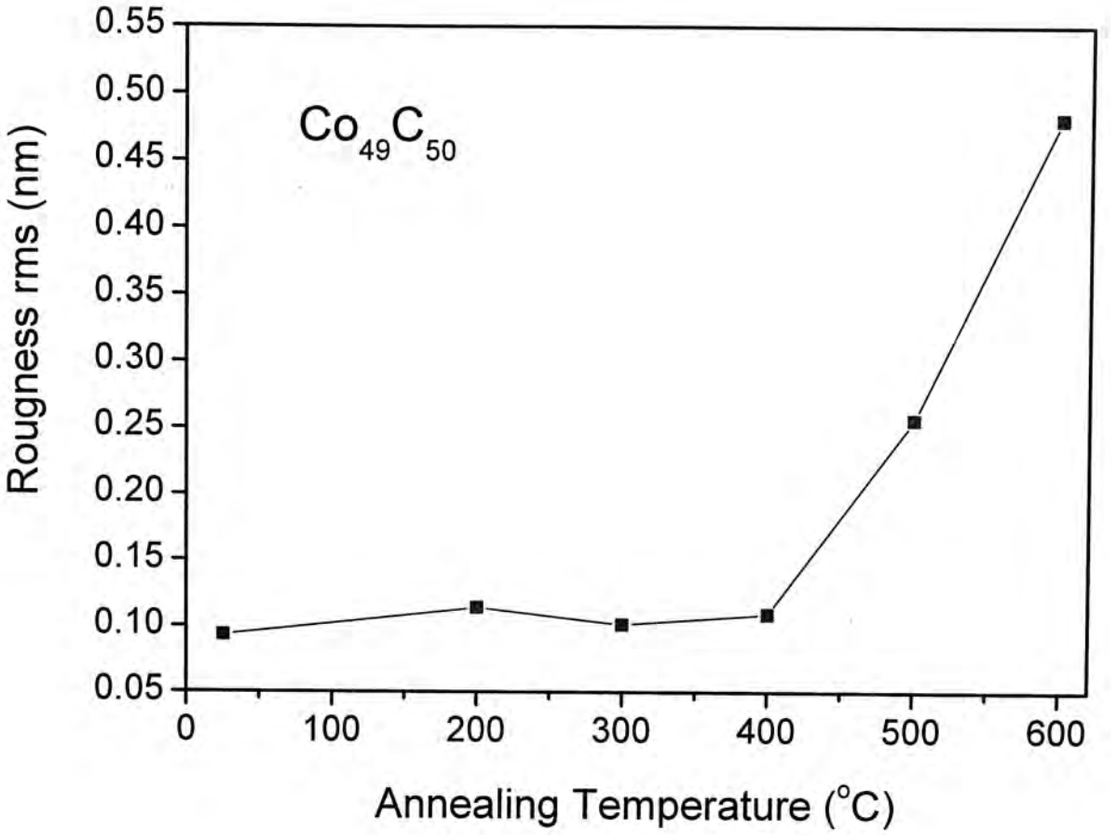


**Fig. 3.10** Root-mean-square roughness (nm) against annealing temperature for the $Co_{49}C_{51}$ sample

This figure shows how the roughness of the sample depends on the annealing temperature. For the samples of as-deposited and the 200℃- 400℃ annealed samples, the surface is smooth and the root-mean-square roughness is about 0.1nm. After annealing at 500℃and 600℃, the root-mean-square roughnesses are 0.25nm and 0.5nm, respectively (Fig. 3.10). This is attributed to the crystallization and grain growth because of the Co hexagonal close-packed (hcp) phase in these samples as mentioned before.

### 3.2.3.2 MFM results

The magnetic domain structures of the co-deposited Co-C samples were studied by a Nanoscopy III scanning probe microscope (Digital Instruments Inc.) with a Co-alloy-coated tip using tapping and lifting modes. As mentioned before, the MFM is capable of detecting the perpendicular magnetization, but not good at detecting the magnetic domain closures at the surface of the sample. During the magnetic domain measurement, the tip is lifted to a height of 20 nm to prevent the influence of the surface morphology.

When the tip is magnetized at vertical direction, the MFM images show the existence of a magnetic microstructure perpendicular to the film plane (Fig. 3.11).

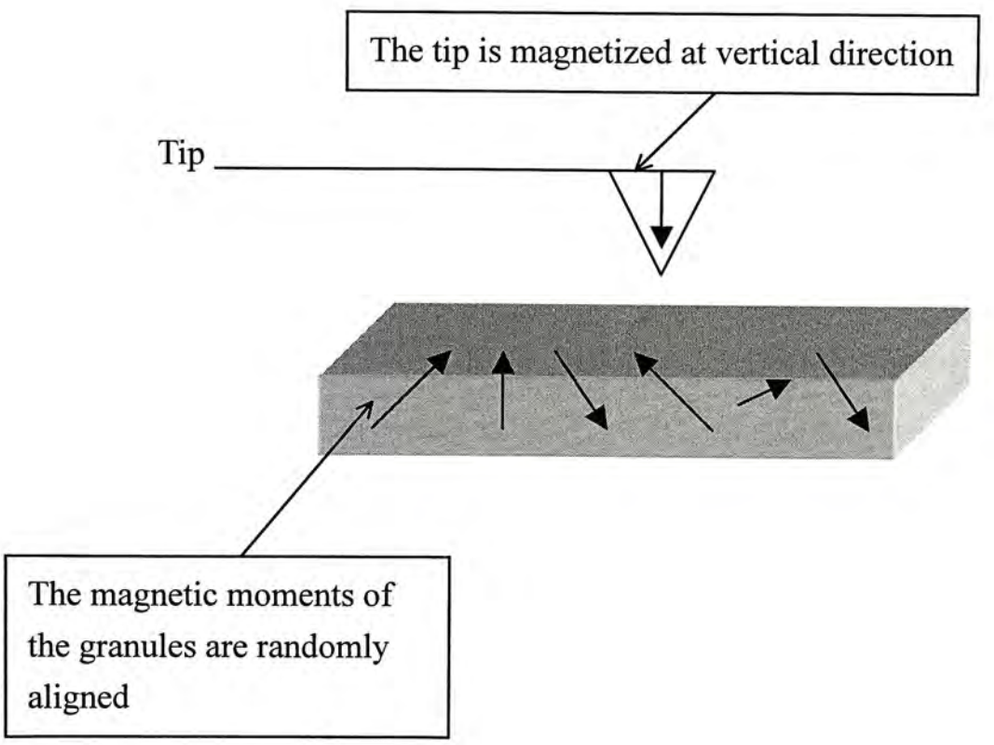


(a)

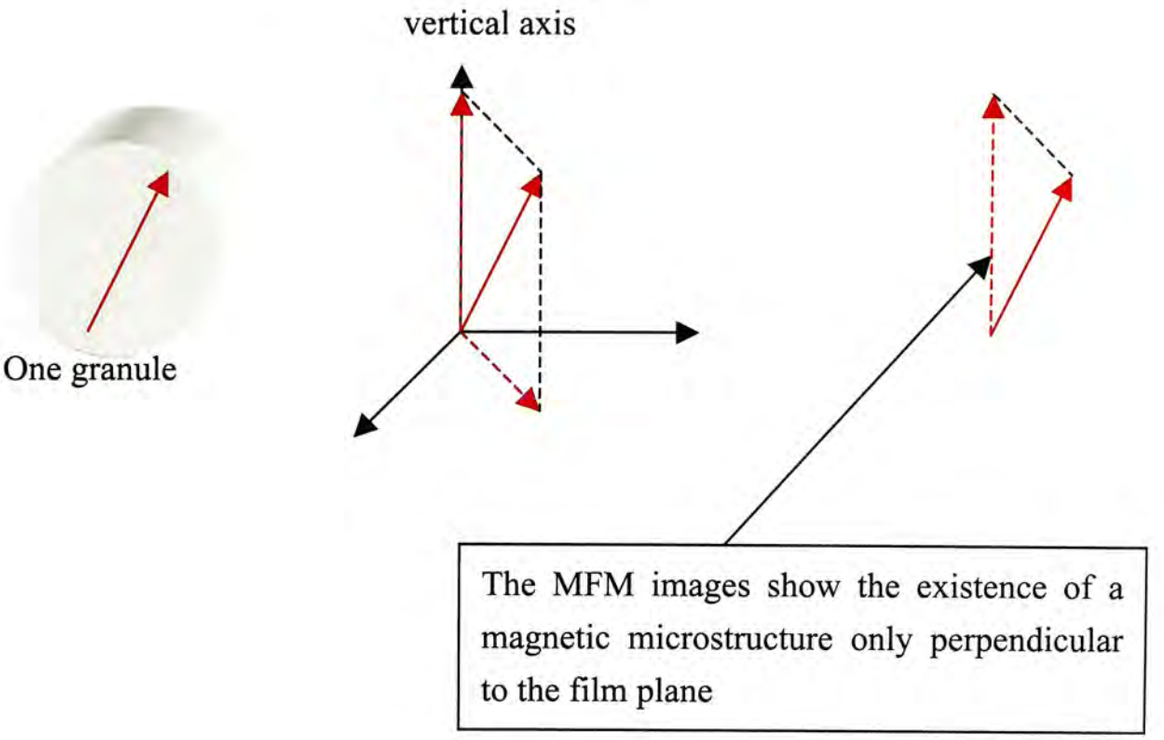


**Fig. 3.11** (a) The relationship of the vertical magnetized tip and random aligned granules. (b) The existence of magnetic microstructure

The AFM images and the corresponding simultaneous MFM images of the as-deposited and annealed $Co_{49}C_{51}$ films are shown in Fig. 3.12(a) to (f). The annealing was performs at temperature from 200℃ to 600℃ in vacuum for 1 h. The as-deposited sample has a MFM image with a poor contrast, not showing any clear domain structures. After annealing at 200℃- 400℃, the contrast of the MFM images remains poor because the hcp-Co phase has not formed. When the annealing temperature reaches 500℃ and 600℃, the MFM images show good contrast and aggregated large domains are observed. This indicates that there is an increase of the exchange coupling between the magnetic grains in these higher temperature annealed samples. The variation of the MFM images with annealing temperature is associated with the Co phase transformation. The MFM images represent magnetic domains

with anti-parallel perpendicular magnetization.

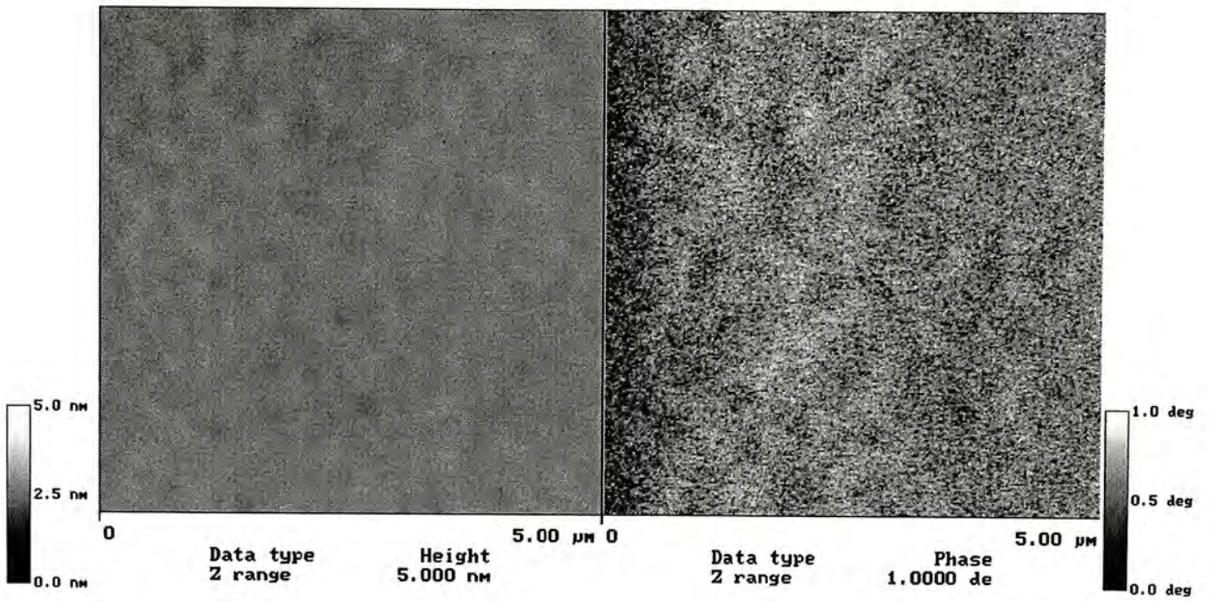


(a)

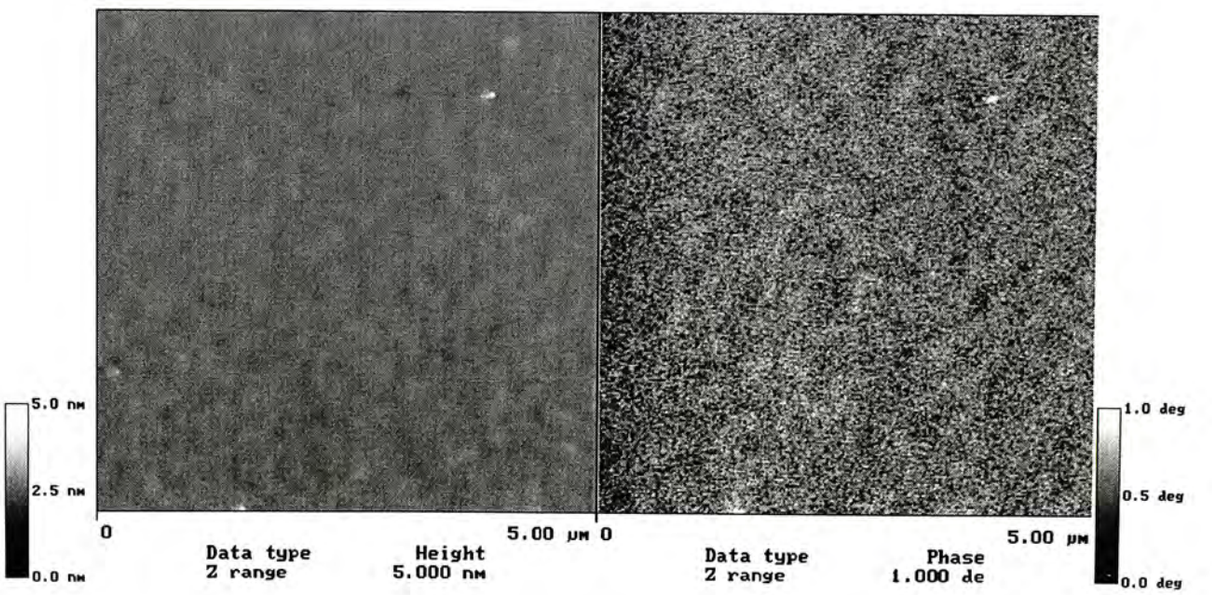


(b)

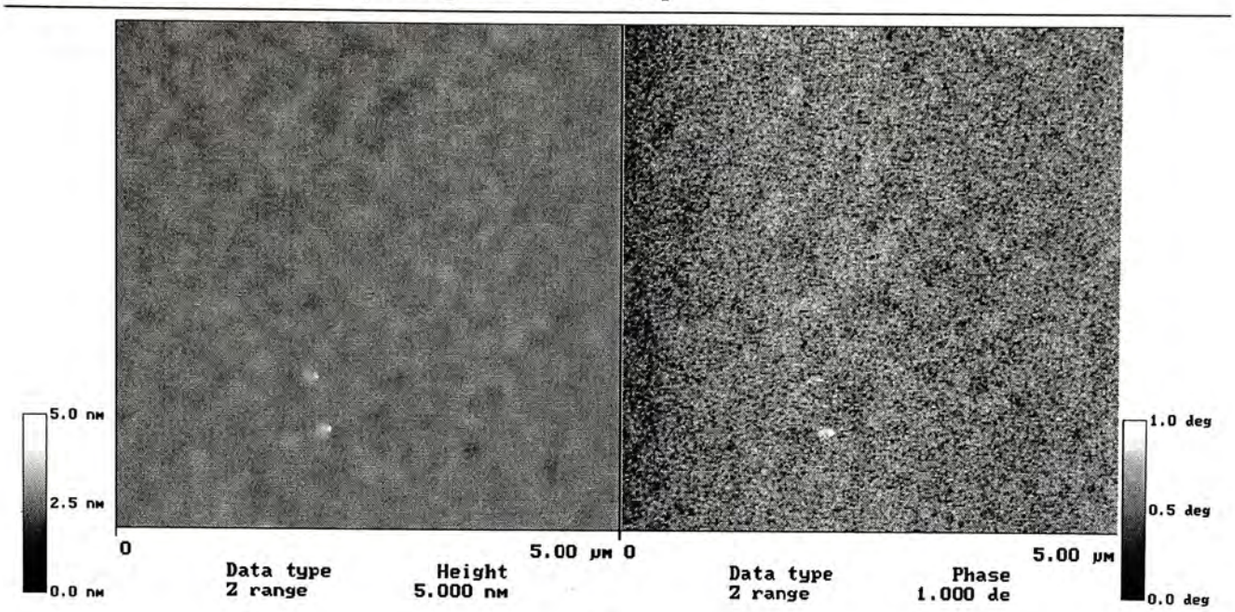
5.0 nm
2.5 nm
0.0 nm
0
5.00 µm
Data type
Z range
Height
5.000 nm
0
5.00 µm
Data type
Z range
Phase
1.000 de
1.0 deg
0.5 deg
0.0 deg

(c)

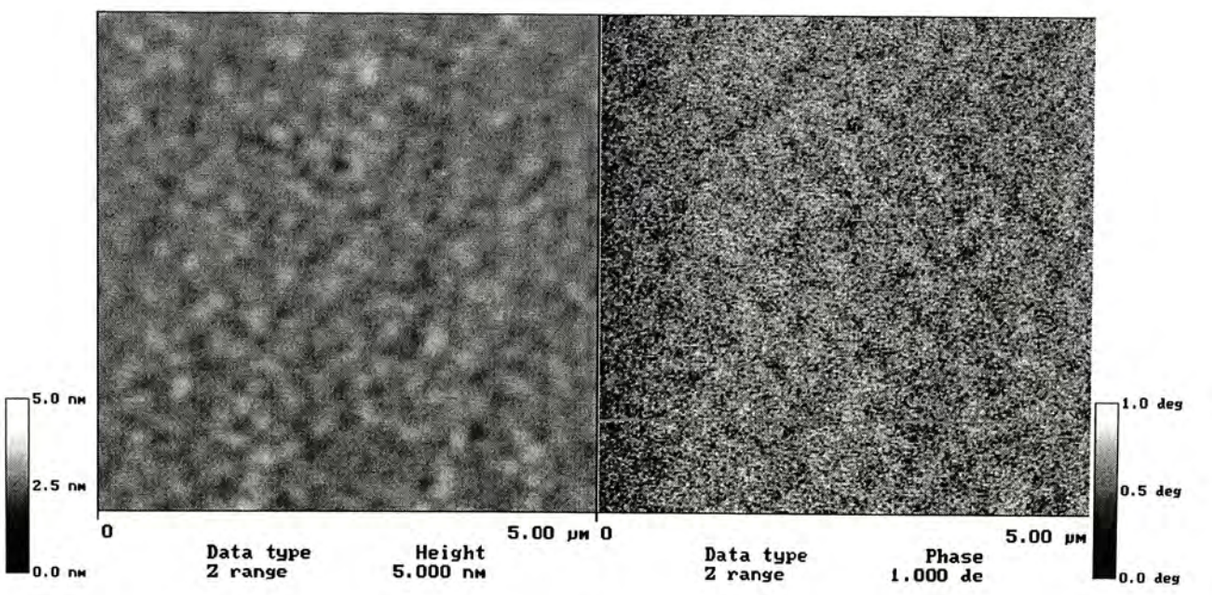
5.0 nm
2.5 nm
0.0 nm
0
5.00 µm
Data type
Z range
Height
5.000 nm
0
5.00 µm
Data type
Z range
Phase
1.000 de
1.0 deg
0.5 deg
0.0 deg

(d)

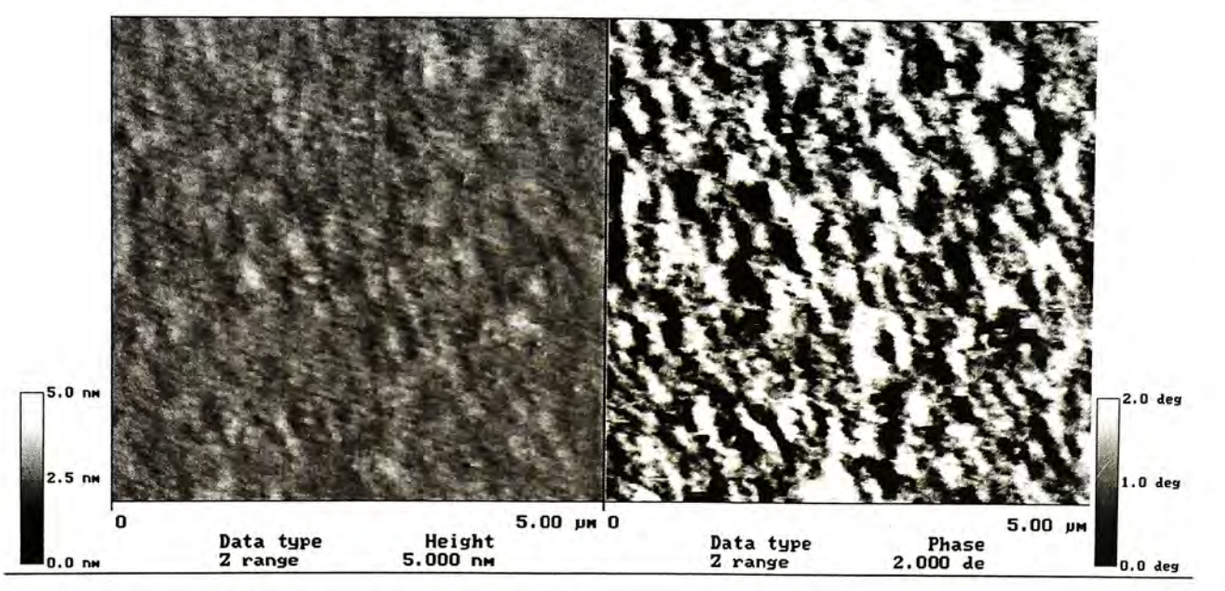
5.0 nm
2.5 nm
0.0 nm
0
5.00 µm
Data type
Z range
Height
5.000 nm
0
5.00 µm
Data type
Z range
Phase
2.000 de
2.0 deg
1.0 deg
0.0 deg

(e)

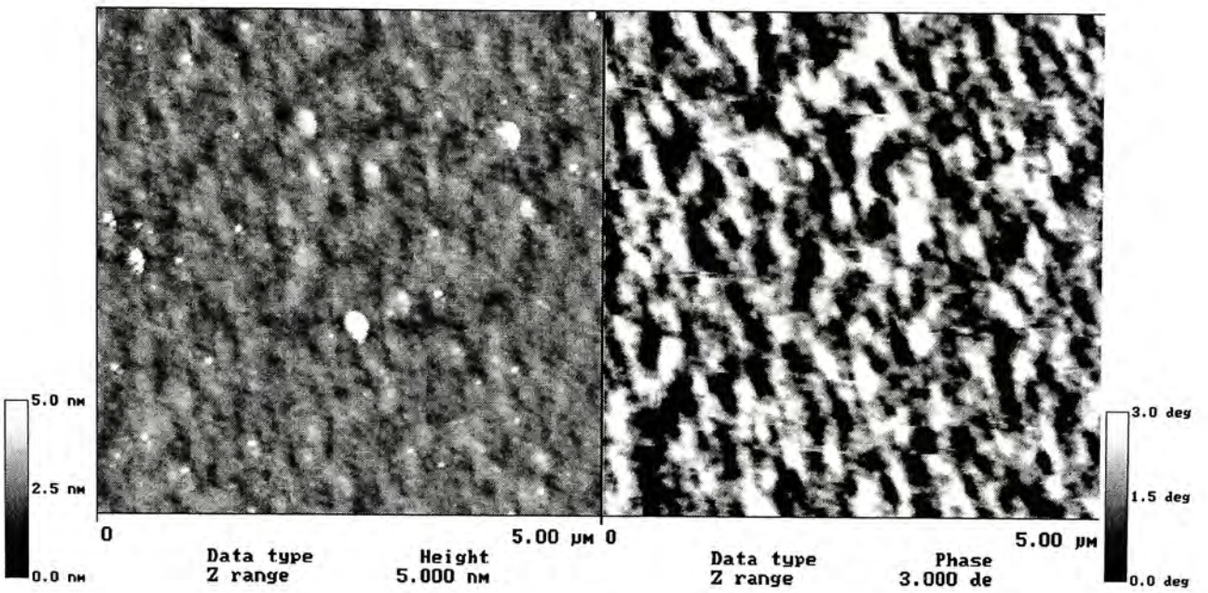


(f)

**Fig. 3.12** AFM (left) and MFM (right) of the $Co_{49}C_{51}$ nanocomposite films. (a) as-deposited; (b), (c), (d), (e) and (f) after annealing at 200℃, 300℃, 400℃, 500℃ and 600℃, respectively

For the samples with a composition of $Co_{30}C_{70}$, the MFM images showed poor contrast even after annealing at 500℃ but MFM images with good contrast and aggregated large domains are observed after annealing at 600℃. The MFM images do not show any domain structures even after annealing at 600℃ for the samples with a composition of $Co_{13}C_{87}$. This is consistent with the XRD results that there is no peak corresponding to the crystalline Co phase observed.

### 3.2.5 Vibrating sample magnetometer (VSM) measurements

The standard M/H loop measurements were performed by VSM measurement. The external field was swept from 2000 Oe to –2000 Oe and then back to 2000 Oe. Therefore, the whole M/H loop was measured. The samples were placed at the centre region between the two magnet pole pieces to ensure that the samples were in a uniform external magnetic field.

Fig 3.13 shows the in-plane magnetic hystersis loops of the $Co_{49}C_{51}$ films after annealing at 500℃ and 600℃ in vacuum for 1 hour. The saturation magnetization $M_S$ and the coercivity $H_C$ for the 500℃ and 600℃ annealed samples are 580 emu/cm$^3$ and 480 Oe, and 630 emu/cm$^3$ and 620 Oe, respectively. For samples annealed at temperature lower than 400℃, XRD results showed that the hcp-Co phase did not form and the MFM results show that no magnetic microstructures could be observed. Also, it is beyond the sensitivity limit of the VSM system we used to measure the hystersis loops of these samples, if any.

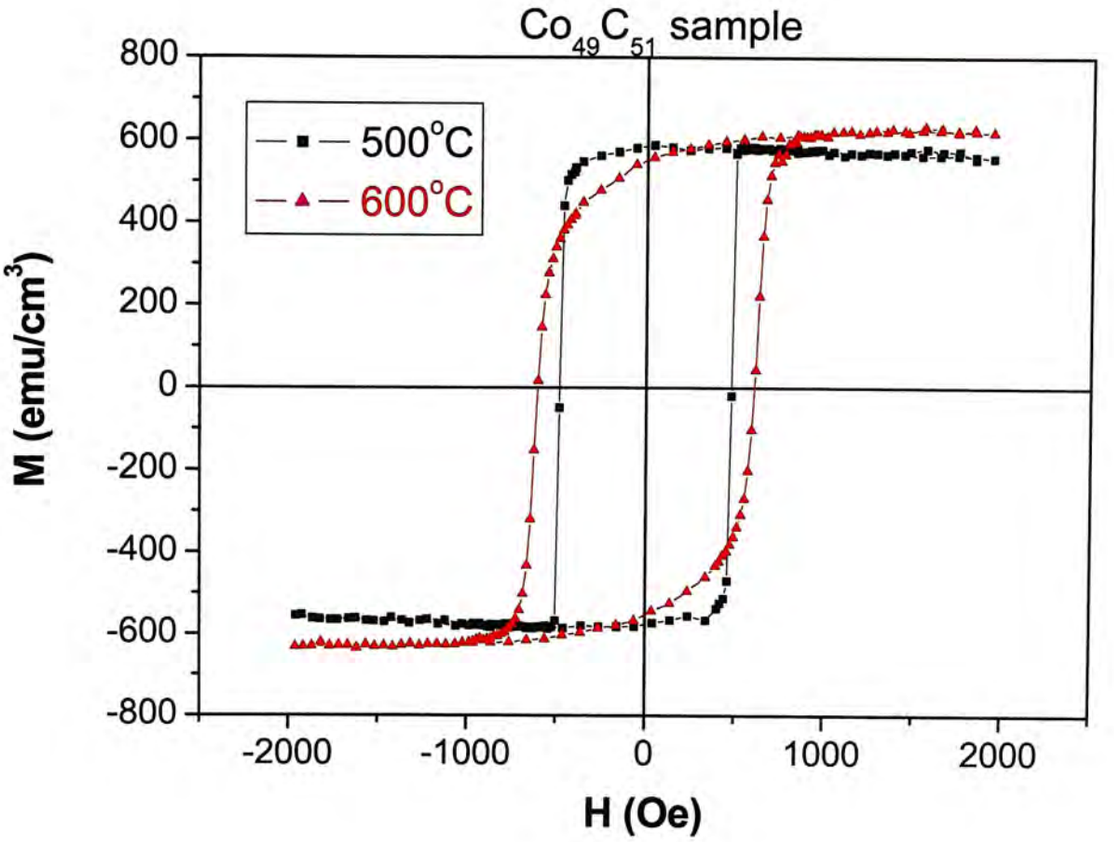


**Fig. 3.13** Magnetic hystersis loops measured at 300K for the $Co_{49}C_{51}$ films after annealing at the temperature as indicated

Figure 3.14 shows the magnetic hystersis loops measured at 300K for the 600℃ annealed films of various composition as indicated. The variation of $M_s$ and $H_c$ with the Co content is shown in Fig. 3.15. The $Co_{49}C_{51}$ film shows the highest saturation magnetization $M_s$ of about 620 emu/cm$^3$ and the $Co_{43}C_{57}$ film shows the highest coercivity $H_c$ of about 700 Oe. For saturated magnetization, when the Co concentration increases from 13 at.% to 49 at.%, Ms is increased almost linearly from 60 eum/cm$^3$ to 620 eum/cm$^3$. Furthermore, when Co concentration increases from 13 at.% to 43 at.%, the coercivity is increased. At a cobalt concentration of 43 at.%, $H_c$ reaches the maximum value of about 700 Oe (Fig. 3.15). When the Co concentration is beyond 43 at.%, it could happen that some of the neighboring Co

grains may contact each other, hence leading possibly to the formation of effective multidomain structures. Therefore intergrain exchange coupling is enchanced when the percolation threshold is reached. The saturation magnetization (Ms), the coercive field (Hc), the magnetic field (Hs) and the ratio of the remanence to the saturation magnetization ($M_r/M_s$) for these films are listed in Table 3.1.

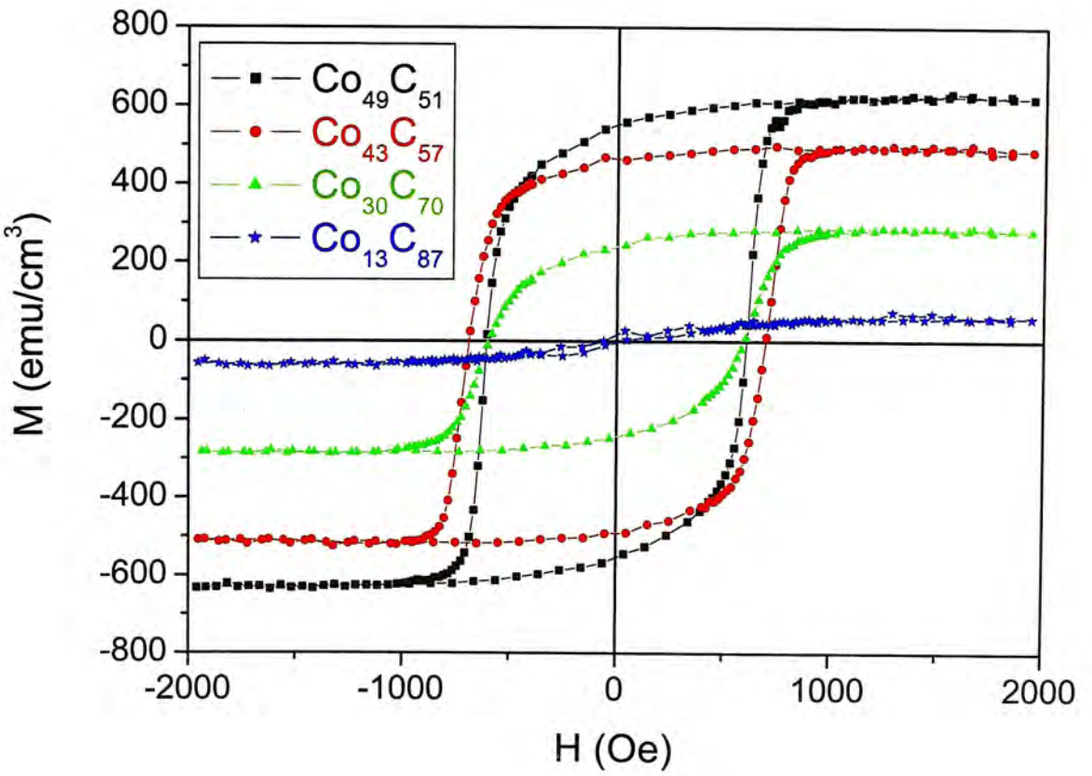


**Fig 3.14** Magnetic hystersis loops measured at 300K for the 600℃ annealed films of various composition as indicated

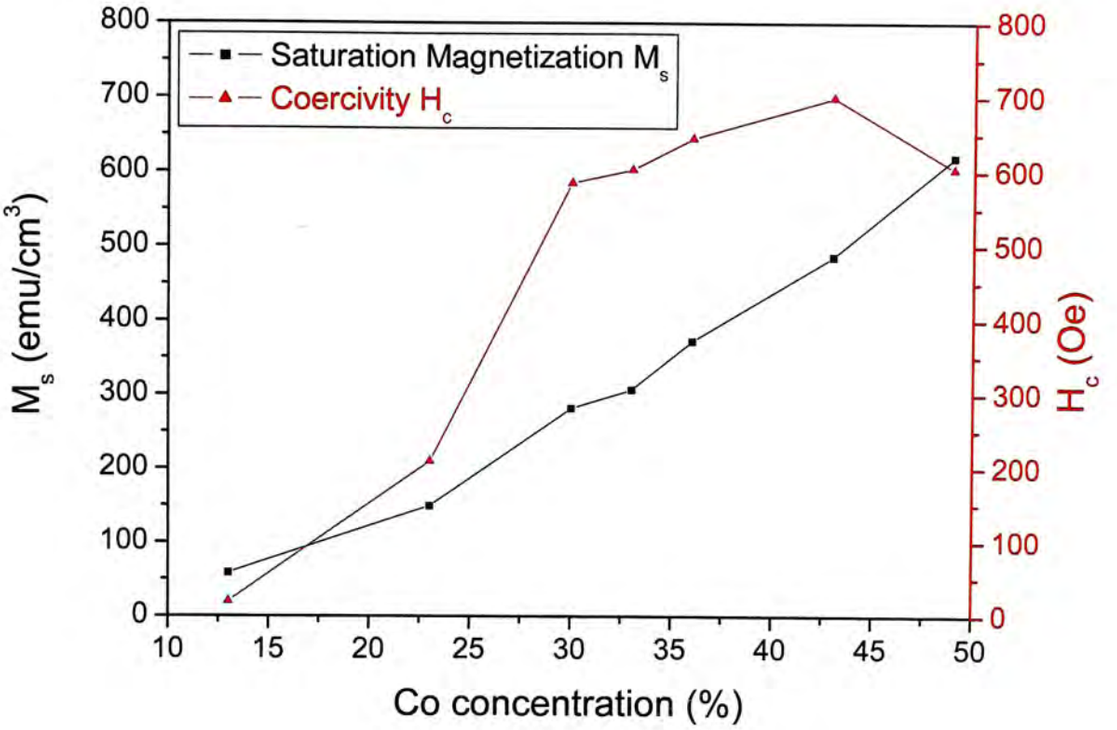


**Fig. 3.15** Saturation magnetization and coercivity versus Co content for Co-C samples annealed 600℃

| | $M_s$ (emu/cm$^3$) | $H_c$ (Oe) | $H_s$ (Oe) | $M_r/M_s$ |
|---|---|---|---|---|
| $Co_{49}C_{51}$ | 620 | 600 | 800 | 0.89 |
| $Co_{43}C_{57}$ | 490 | 700 | 850 | 0.94 |
| $Co_{36}C_{64}$ | 370 | 645 | 850 | 0.91 |
| $Co_{33}C_{67}$ | 310 | 600 | 850 | 0.98 |
| $Co_{30}C_{70}$ | 280 | 585 | 850 | 0.88 |
| $Co_{23}C_{77}$ | 150 | 210 | 300 | 0.62 |
| $Co_{13}C_{87}$ | 60 | 20 | 30 | 0.34 |

**Table 3.1** Saturation magnetization ($M_s$), coercivity ($H_c$), saturation magnetic field ($H_s$), and the ratio of the remanence to the saturation magnetization $M_r/M_s$ as obtained from the M-H loops of the 600℃ annealed Co-C films at 300 K

With the increase of the Co concentration, while $M_s$ increased linearly and $H_c$ also increased. The round shape hystersis loops with $M_r/M_s$ ratio of 0.34 and 0.62 were observed in the $Co_{13}C_{87}$ and $Co_{33}C_{77}$ films respectively. On the other hand, the rectangular hystersis loop with $M_r/M_s$ ratio around 0.9 was obtained in the cobalt concentration above 30 at.% films.

The obtained saturation magnetization $M_s$ is at the same level as those of cobalt-based alloy media (300 – 600 emu/cm$^3$) for high-density-recording [27]. Furthermore, the required coercivity $H_c$ of the future ultra-high-density recording media is about 2500 Oe to increase the linear resolution [28]. The obtained coercivity values of our Co-C granular thin films are yet too small for such applications. In order to solve this problem, we note that there are reports in the literature on the possibility of attaining higher coercivity by optimizing the fabrication processes [29]. On the other hand, higher coercivity could also be attained by adding other elements such as Pt to the Co-C thin films without changing their nanogranular morphology but increasing the uniaxial magnetocrystalline anisotropy $K_u$ through the formation of fct-cobalt-pt phase [30].

**3.3 Summary:**

We have prepared Co-C granular films by pulsed filtered cathodic arc co-deposition system and studied their structural and magnetic properties. In the structural part, the hcp-Co phase is formed when the samples with Co concentration larger than 30 at.% were annealed at a temperature of 500℃ or above. The

root-mean-square roughness value of these samples increased also with annealing temperature. MFM images with good contrast and aggregated large domains are observed in these samples. As the Co concentration increased from 13 at.% to 49 at.%, Ms also increased almost linearly from 60 eum/cm$^3$ to 620 eum/cm$^3$. But the coercivity $H_c$ increase up to a Co concentration of 43 at.%, reached the maximum value about 700 Oe and then decreased at higher Co concentration. This is attributed to the enhancement of intergrain exchange coupling when the percolation threshold of the Co grains is reached.

# Chapter 4 Characterization of co-deposited Fe-C samples

## 4.1 Introduction

Similar to the preparation of the Co-C films, nano granular Fe-C thin films on thermally grown $SiO_2$ layer (400nm) on Si (100) substrates were prepared by pulsed-filtered vacuum arc deposition (PFVAD) using pure iron and graphite as the cathodes. A negative bias voltage of –80V was applied during deposition. The composition of the films was controlled by varying the arc discharge conditions and the pulse sequence of the two sources. For the carbon source, a 65° and 45° double bent magnetic filter was used in order to filter the carbon macroparticles. Thermal annealing was performed in a vacuum furnace (~$8\times10^{-4}$ Pa) for 1 hour at various temperatures ranging from 200 to 500℃.

Two adjacent sources were operated simultaneously in a pulsed mode with a pulse duration of 2.5ms. The pulse train frequency is normally set at 4 pulses per second but individual pulses can be on or off by computer control. The base pressure in the chamber during deposition was less than $4\times10^{-4}$ Pa.

**Pulsed-filtered vacuum arc deposition (PFVAD) condition:**

| | Carbon | Iron |
|---|---|---|
| Bias | 107V | 105V |
| Focus | 80 $\mu$ A | 85 $\mu$ A |
| Arc | 120V | 125V |
| Trigger | 125V | 125V |
| Deflect | 125 $\mu$ A | 130 $\mu$ A |

The composition and thickness of the $Fe_yC_{1-y}$ films were determined by non-Rutherford backscattering spectrometry (NRBS) and their structural and magnetic properties were studied using x-ray diffraction (XRD), transmission electron microscopy (TEM), x-ray photoelectron spectroscopy (XPS), atomic-force microscopy (AFM), magnetic-force microscopy (MFM) and vibrating sample magnetometer (VSM). The resistivity is measured by the four-contact technique. The NRBS experiments were performed with a 2MV tandem accelerator at a resonance mode for the carbon atoms, using a beam of 3.5MeV $^4He^{++}$ ions at an incident angle of $7^o$ to the normal line of the film plane and with the backscattering $He^{++}$ ions detected at a scattering angle of $170^o$. Both the AFM and MFM imaging were performed by tapping and lift modes under ambient condition, using a Nanoscope III scanning probe microscope with a hard Co-alloy-coated silicon tip magnetized along the tip direction.

## 4.2 Results and discussion

### 4.2.1 NRBS measurements

Typical NRBS spectra of three samples prepared using the pulsed filtered arc co-deposition technique with compositions as indicated are shown in Fig. 4.1. The NRBS spectra reveal that the composition of the Fe-C films is nearly constant through out the layer. By assuming a uniform composition and using the SIMNRA 4.4 software, the iron concentration for each of these films was determined quantitatively to be 66, 74 and 90 at.%, respectively. The thickness of these samples with compositions of $Fe_{66}C_{34}$, $Fe_{74}C_{26}$ and $Fe_{90}C_{10}$ were determined to be 28nm, 31nm and 29nm, respectively. The fitting accuracy of the composition and thickness are about 1 at.% and 1 nm, respectively.

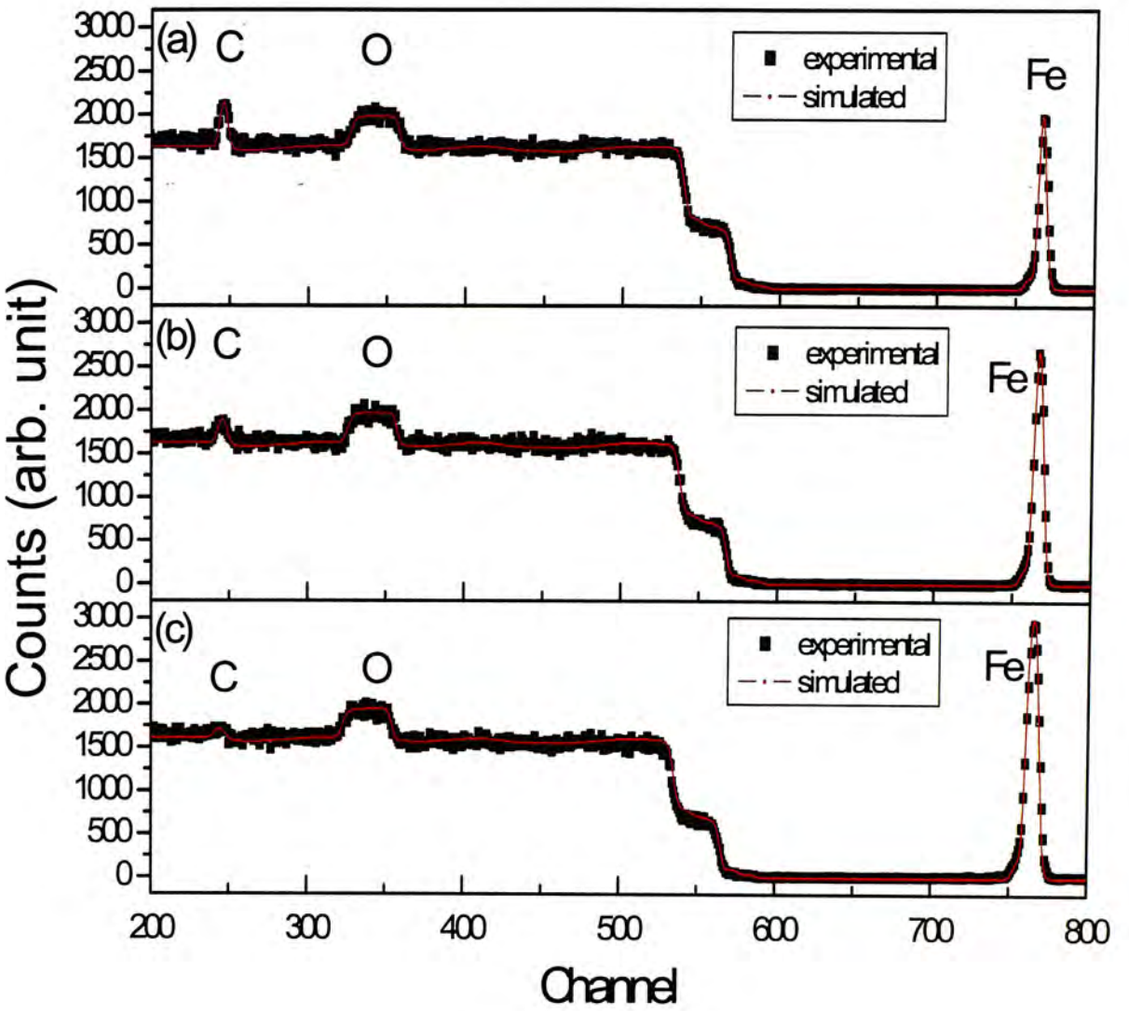


**Fig. 4.1** NRBS spectra of the $Fe_yC_{1-y}$ films. The fitted composition is (a) $Fe_{66}C_{34}$, (b) $Fe_{74}C_{26}$, and (c) $Fe_{90}C_{10}$, respectively

### 4.2.2 X-ray diffraction

The structures of the films were studied by XRD. The XRD experiments were done with a Siemens D5005 x-ray diffractometer, using the glancing incidence mode and the Cu $K\alpha$ radiation. In the experiments, the incident angle was 1°, the

scanning step size was 0.06°, and the scanning range of $2\theta$ was 35° to 80°. Since the signal of the diffraction is very weak, repeated scans from 35° to 80° were performed for many times and the accumulated results were recorded.

The XRD patterns of the as-deposited and annealed $Fe_{74}C_{26}$ films are shown in Fig. 4.2. The as-deposited film was found to be amorphous. The XRD patterns of these samples reveal that small grains of body-centre-cubic (bcc) crystalline Fe and $Fe_3C$ iron-carbide may be co-existed in the films after annealing at 400℃ and 500℃. It is very difficult if not impossible, to separate the peaks from bcc-Fe and $Fe_3C$ from these spectra. Therefore, XPS was used to determine whether only either one of the bcc-Fe, and $Fe_3C$ phases existed, or both of these two phases could have co-existed in these samples. Moreover, the sample $Fe_{66}C_{34}$ is very similar to the $Fe_{74}C_{26}$ sample like the structural formation by XRD results.

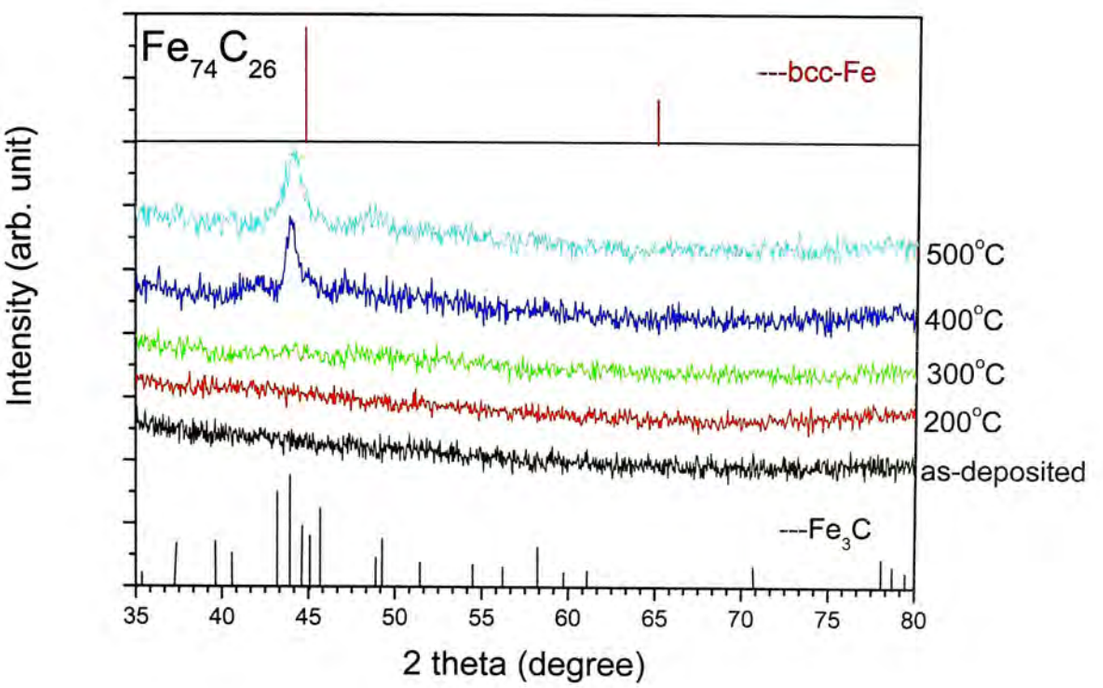


**Fig 4.2** XRD spectra for the as-deposited and annealed $Fe_{74}C_{26}$ films at 200, 300, 400 and 500℃

In the Fig. 4.3, are shown the XRD spectra of the as-deposited and annealed $Fe_{90}C_{10}$ films at various temperatures up to 500℃. Only bcc-Fe phase was formed in the $Fe_{90}C_{10}$ samples after annealing at temperature higher or equal to 300 ℃. The small peak occurred at the 65° is a strong evidence. By Scherrer's formula $D = \frac{K\lambda}{W\cos\theta}$, the grain size was determined to be 15nm using the (110) line when the sample annealed at 500℃.

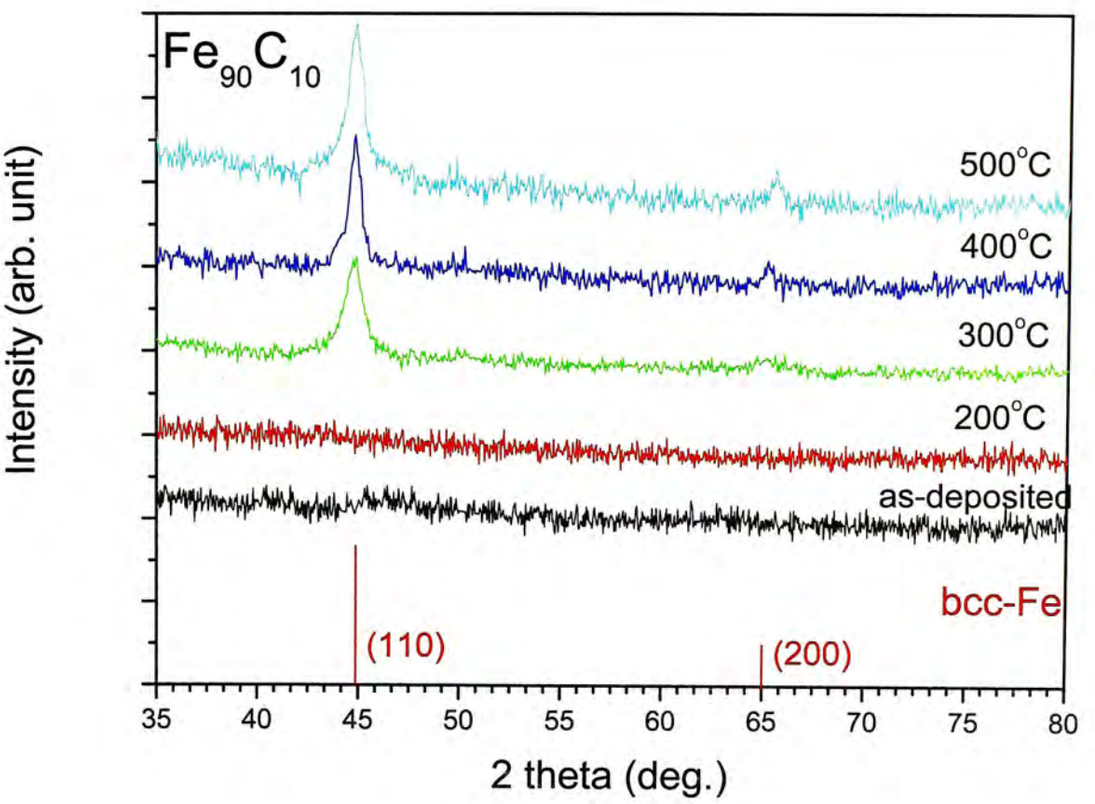


**Fig 4.3** XRD spectra for the as-deposited and annealed $Fe_{90}C_{10}$ films at various temperature as indicated

### 4.2.3 X-ray photoelectron spectroscopy (XPS):

In order to know whether bcc-Fe or $Fe_3C$ were formed or not when the $Fe_{74}C_{26}$ films were annealed at 500℃, XPS measurements were performed trying to separate these phases clearly. Before the XPS experiments, an Ar ion gun was used to sputter about 10nm depth of the surface of the sample in order to prevent interference due to the detection of impurities and oxide because of surface contaminations. After XPS measurement, the whole two main peaks at about 283.3, and 707.0 eV, corresponding to the binding energy of C-1s and Fe-2p, respectively. The atomic concentration of C:O:Fe was calculated to be 24.8:0.3:74.9, respectively. Therefore the atomic ratio of Fe to C is determined to be 75:25. It is consistent with the value determined by NRBS measurements. While the binding energies of the Fe-2p peak [shown in Fig. 4.4 (a)] in pure iron and iron carbides almost coincide with each other, those of the C-1s peak in iron carbide and amorphous carbon or graphite are different. As shown in Fig. 4.4 (b), the C-1s peak was fitted using two Gaussian peaks centered at 283.3, and 284.4eV with area percentages of 96.3%, and 3.7%, respectively. The peak at 283.3eV is corresponding to the binding energy of C-1s in iron-carbide [31]. The other peak corresponds to those of carbon-carbon bonds [32]. The O-1s peak is so weak in Fig. 4.4 (c) so the contribution of the FeO and oxygen to the magnetic properties of this film could be ignored. Moreover, the concentration of Fe and C is three to one, three iron atoms and one carbon atom are formed to a compound easily. Among the XRD, XPS and the concentration of FE and C, we can conclude that $Fe_3C$ should have been formed in the $Fe_{74}C_{26}$ samples after annealing at temperatures above 400℃.

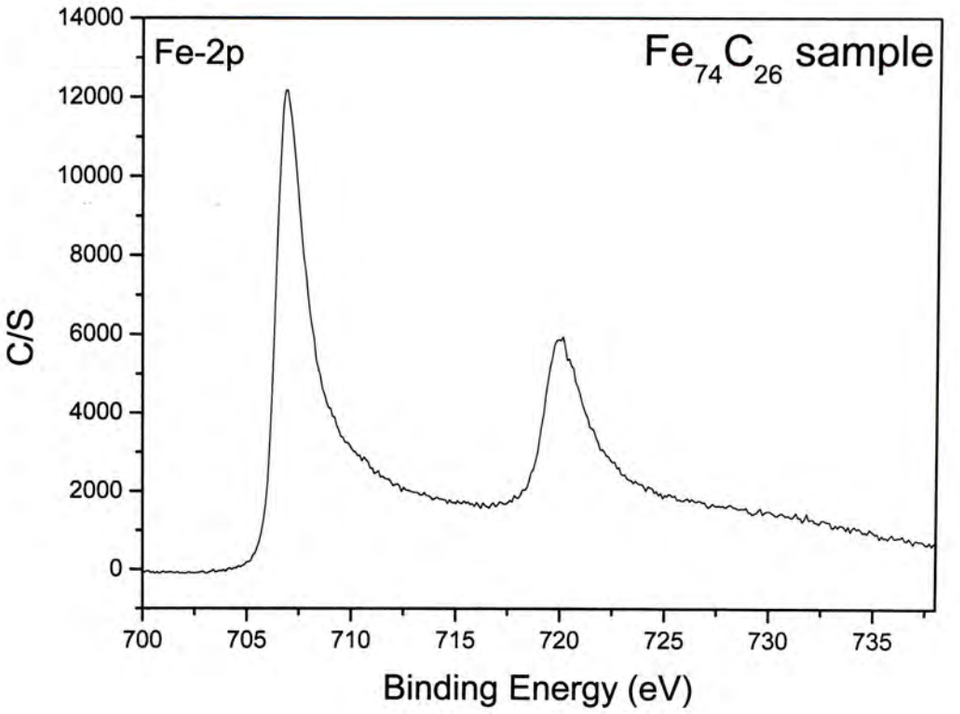
Fe-2p
$Fe_{74}C_{26}$ sample
C/S
Binding Energy (eV)
14000
12000
10000
8000
6000
4000
2000
0
700
705
710
715
720
725
730
735

(a)

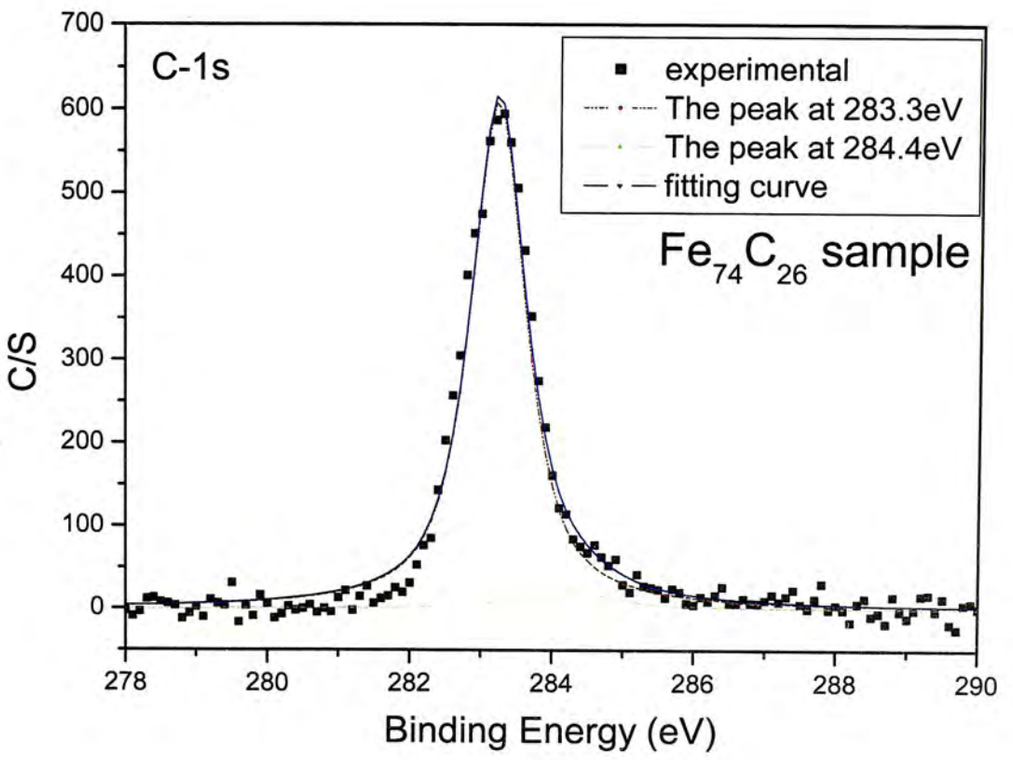
C-1s
experimental
The peak at 283.3eV
The peak at 284.4eV
fitting curve
$Fe_{74}C_{26}$ sample
C/S
Binding Energy (eV)
700
600
500
400
300
200
100
0
278
280
282
284
286
288
290

(b)

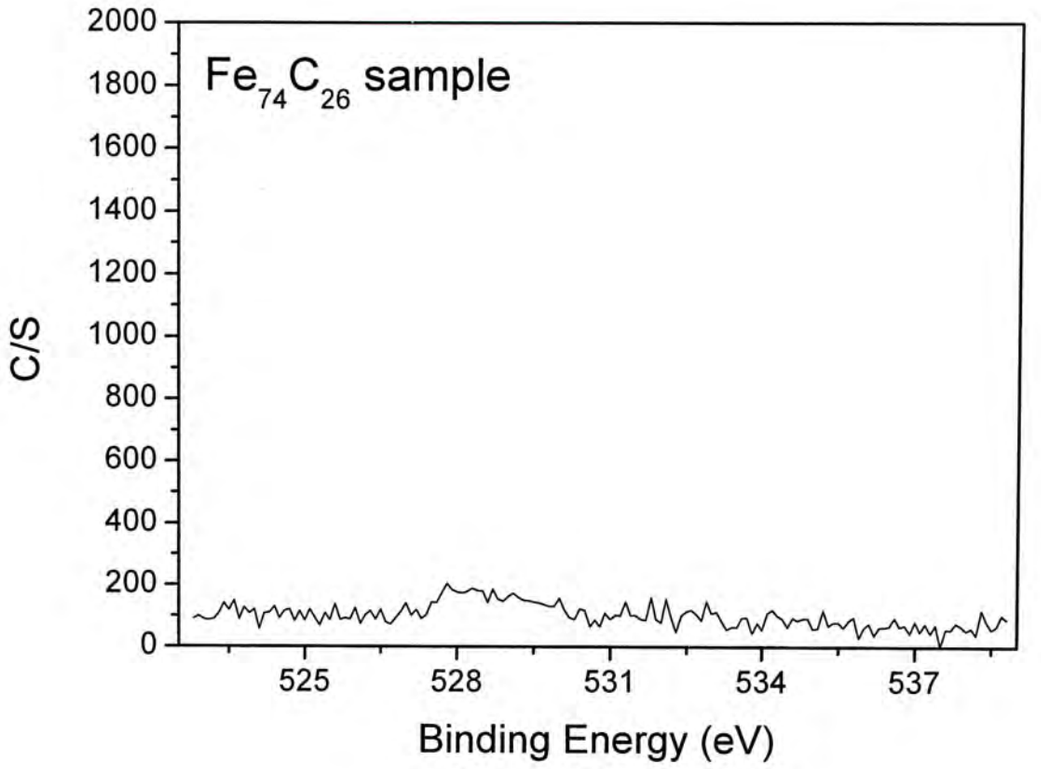


(c)

**Fig. 4.4** XPS spectra for the 500℃ annealed $Fe_{74}C_{26}$ film. (a) Fe-2p spectrum, (b) C-1s spectrum, and (c) O-1s spectrum

| | $Fe_3C$ | bcc-Fe |
|---|---|---|
| $Fe_{66}C_{34}$ | Yes | No |
| $Fe_{74}C_{26}$ | Yes | No |
| $Fe_{90}C_{10}$ | No | Yes |

**Table 4.1** Crystallization summary of 500℃ annealed $Fe_{66}C_{34}$, $Fe_{74}C_{26}$ and $Fe_{90}C_{10}$ samples

### 4.2.4 AFM results

The surface morphology of the co-deposited Fe-C granular films was observed using a Digital Instrument III AFM, operating in the tapping mode. Five typical AFM micrographs for the $Fe_{90}C_{10}$ samples annealed at different temperatures are shown in Fig. 4.5. The granular particle feature can be observed in the surface morphology of these samples. The sizes of the AFM images are 5 $\mu$m$\times$ 5 $\mu$m. The root-mean-square surface roughness of the samples with different annealing temperature is shown in Fig. 4.6.

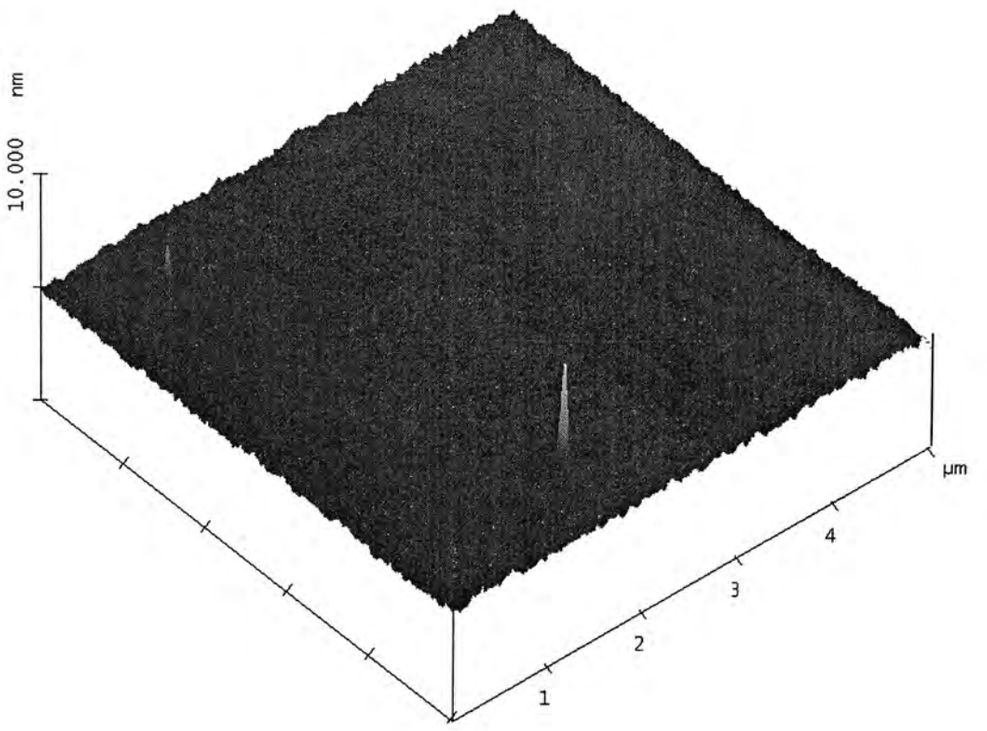


(a)

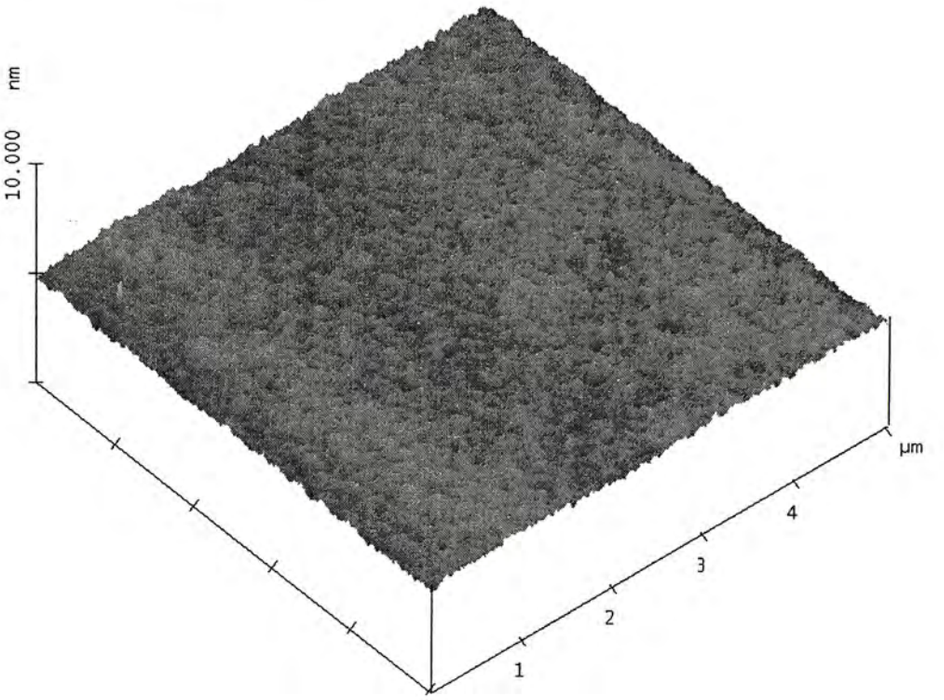


(b)

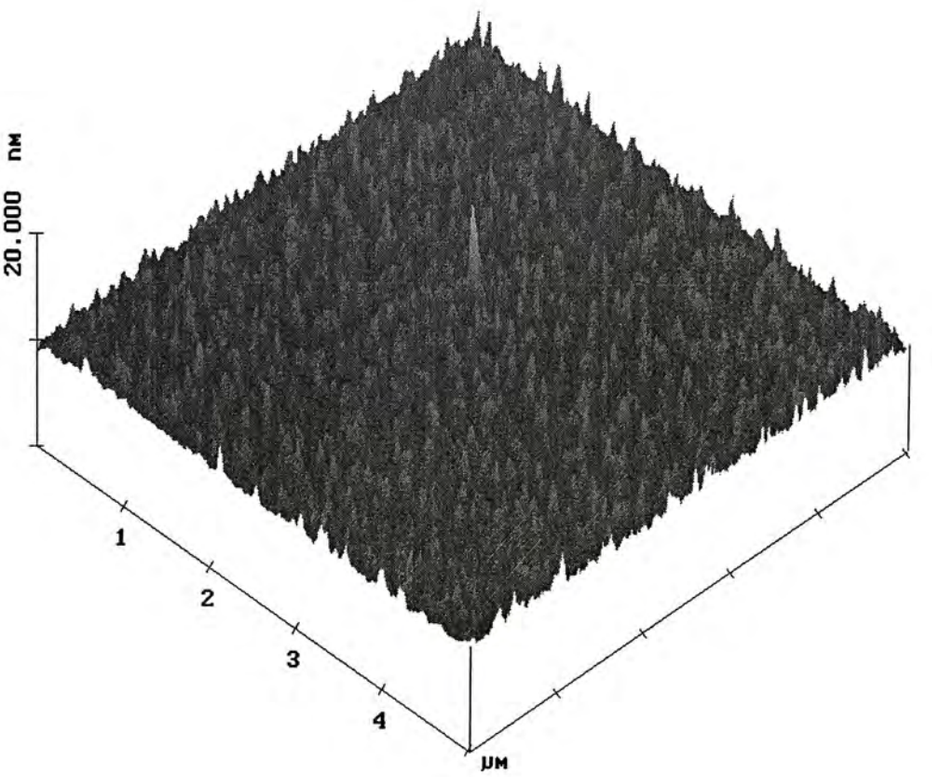


(c)

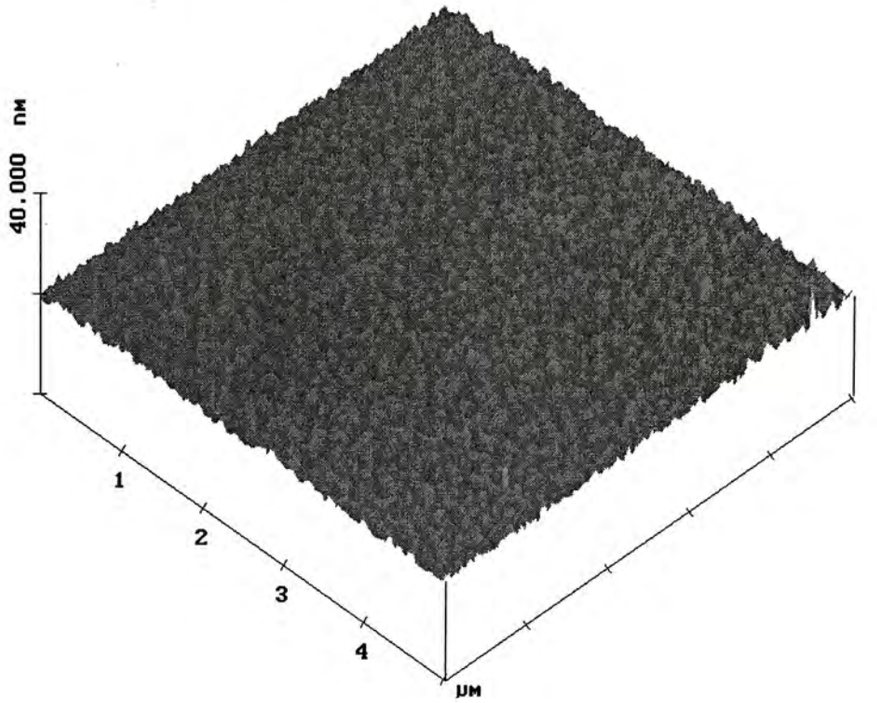


(d)

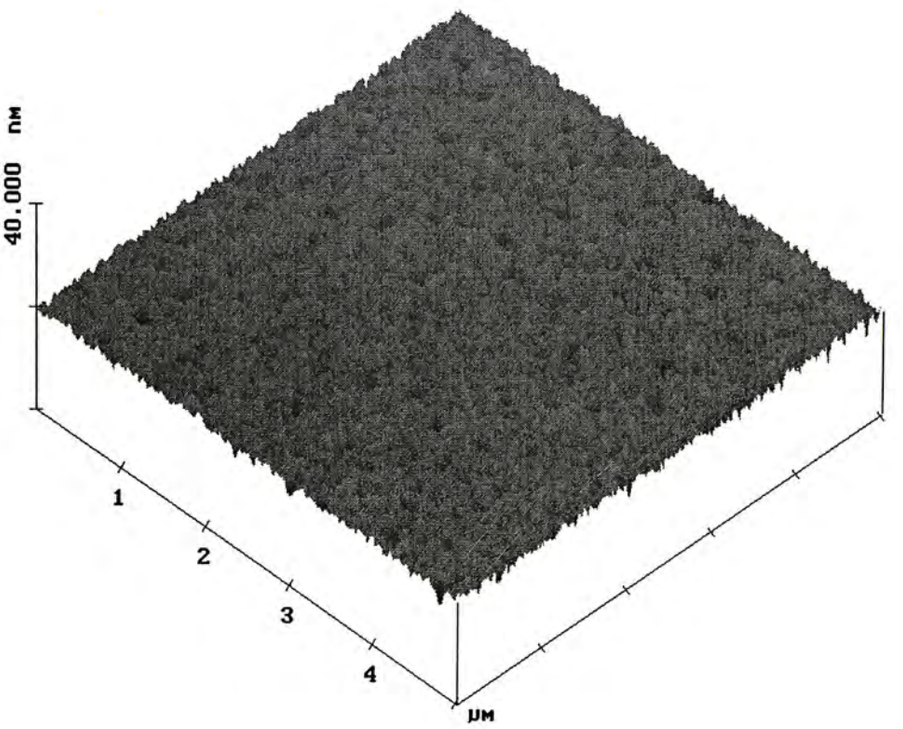


(e)

**Fig. 4.5** AFM images of the $Fe_{90}C_{10}$ nanocomposite films. (a) as-deposited; (b), (c), (d) and (e), after annealing at 200℃, 300℃, 400℃ and 500℃, respectively

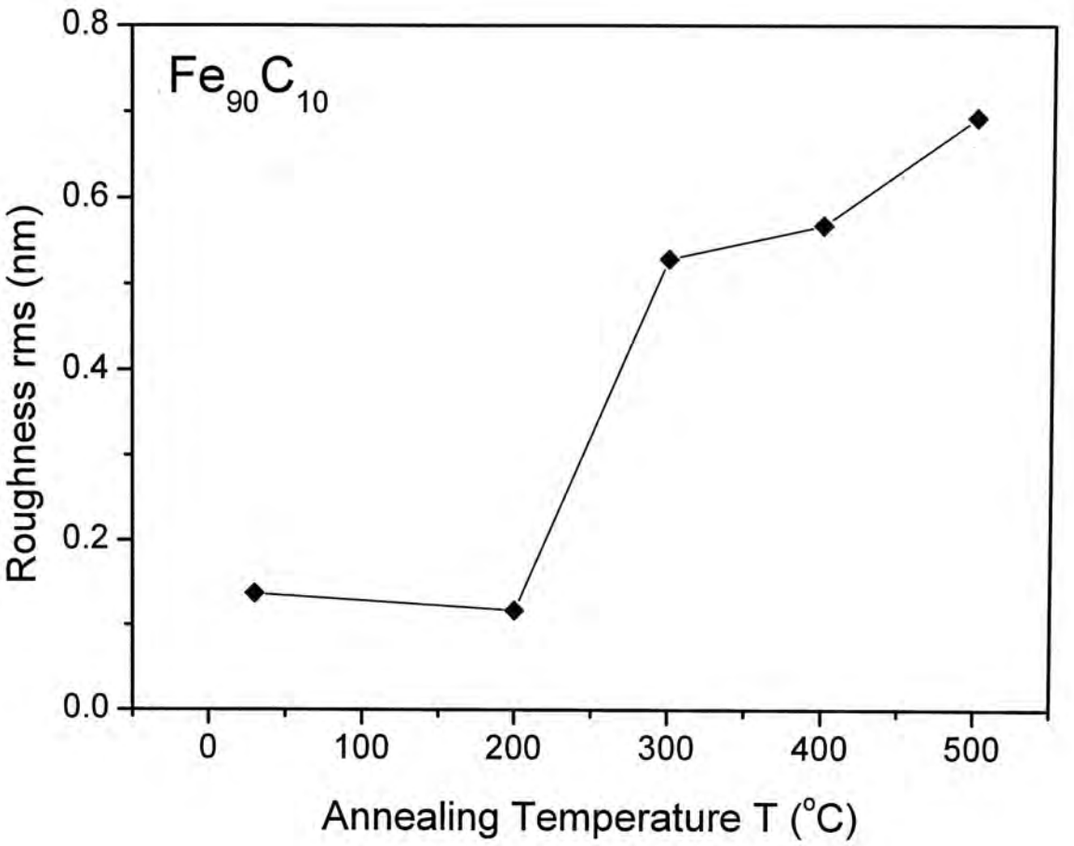


**Fig. 4.6** The graph of root-mean-square roughness (nm) against annealing temperature for $Fe_{90}C_{10}$ sample

The roughness of the sample depends on the annealing treatment. The as-deposited samples and 200℃ annealed samples showed a very smooth surface morphology. The root-mean-square roughness is about 0.15nm. After annealing at temperature equal to or above 300℃, because the crystallization and grain growth of the Fe body-centered cubic (bcc) phase, the root-mean-square value in roughness of the samples increased rapidly from 0.15 nm to about 0.55 nm at an annealing temperature of 300℃ and eventually to about 0.69 nm at annealing temperature of 500℃ annealing. These AFM results are consistent with to the XRD results.

### 4.2.5 MFM results

The magnetic domain structures of these co-deposited Fe-C samples were studied by a Nanoscopy III scanning probe microscope (Digital Instrument Inc.) with a Co-alloy-coated silicon tip using tapping and lift modes. As mentioned before, the MFM is capable of detecting the magnetization. The tip is lifted to a height of 20 nm to prevent the influence of the surface morphology during the magnetic domain measurement.

Figure 4.7 shows the simultaneously obtained AFM (left) and MFM (right) images of the as-deposited and annealed $Fe_{90}C_{10}$ films. The bright and dark regions in the MFM images represent magnetic domains with anti-parallel perpendicular magnetization to the film plane. MFM images of the co-deposited samples do not seem to have correlation with the surface morphology as revealed by the AFM images. It is because the roughness of the surface morphology is so smooth and we should use the tapping and lift modes of the MFM measurement. According to the XRD results, bcc-Fe is formed when the annealing temperature increased to 300℃. The MFM images of the as-deposited and 200℃ annealed $Fe_{90}C_{10}$ films show a relatively poor magnetic contrast. It shows that the as-deposited and 200℃ annealed $Fe_{90}C_{10}$ films seem to be amorphous and therefore no domain structure is formed at room temperature. When the annealing temperature reaches to 300, 400 and 500℃, MFM images with good contrast and aggregated large domains are observed, as shown in Fig. 4.7 (c), (d), and (e), respectively. This is consistent with the XRD results which showed that bcc-Fe grains were formed when the $Fe_{90}C_{10}$ films were annealed at temperature equal to or above 300℃. The MFM images show explicitly that magnetic domain structures with widths as small as 0.2 $\mu$m were formed in

these annealed samples.

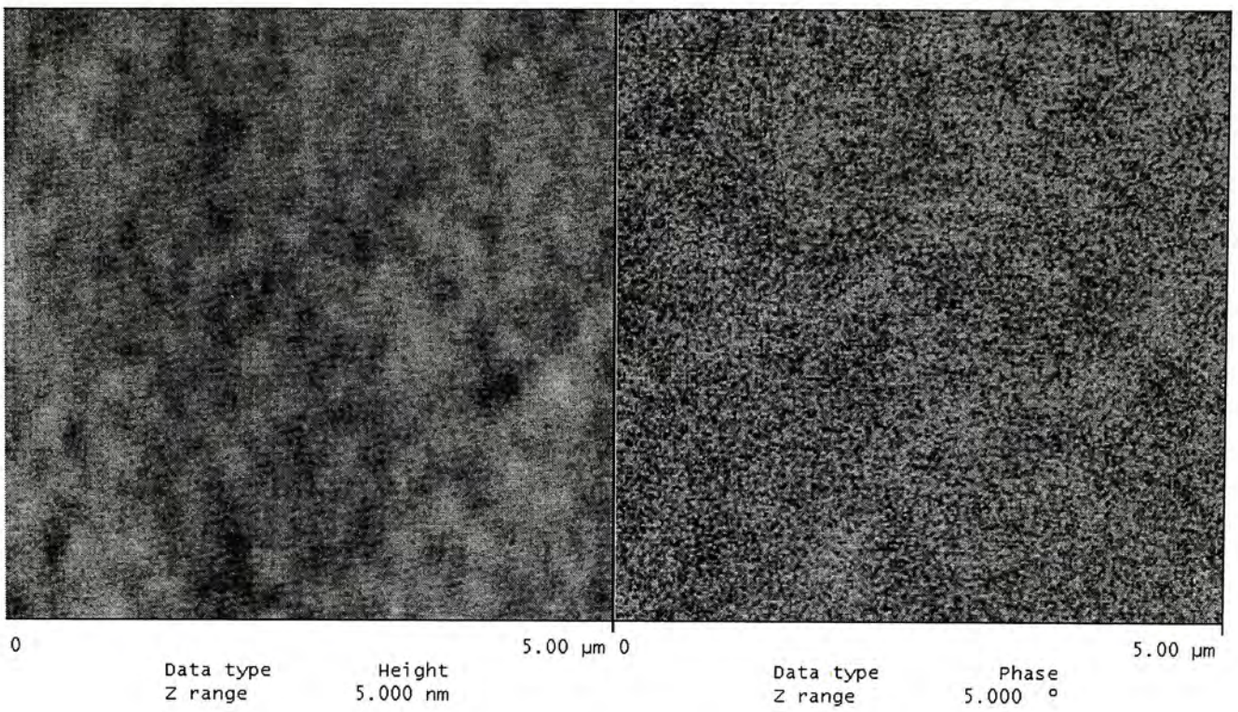


(a)

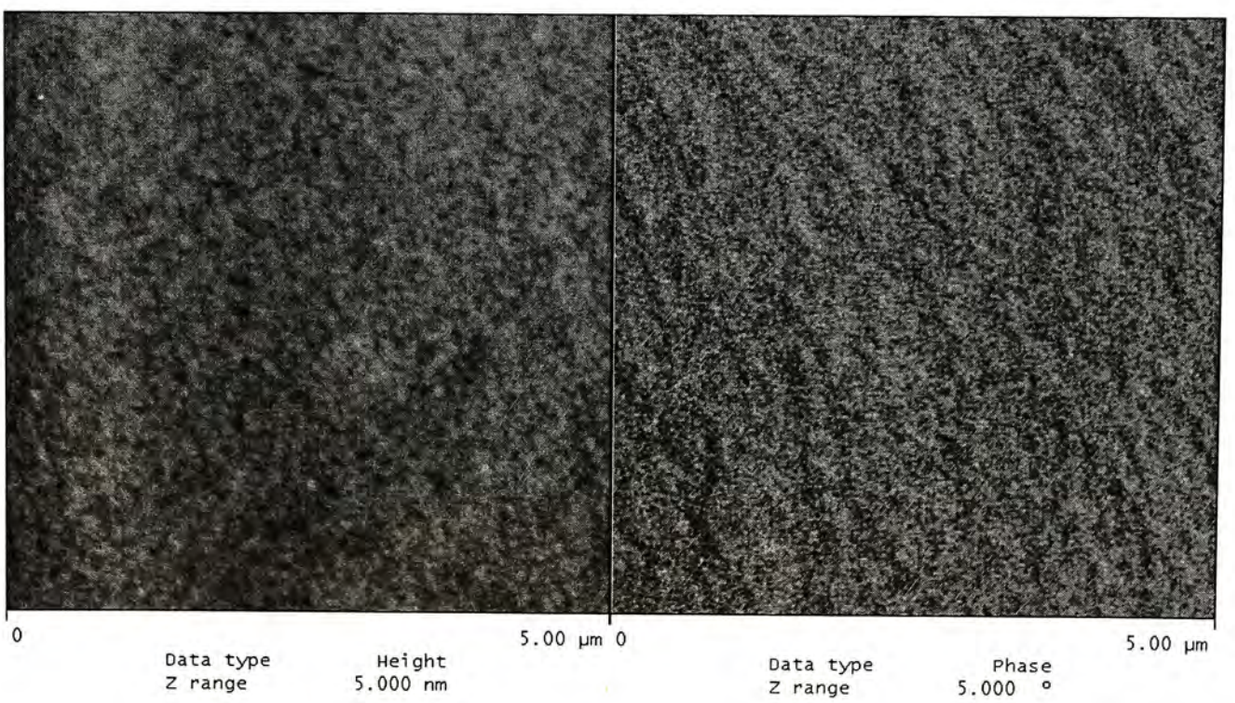


(b)

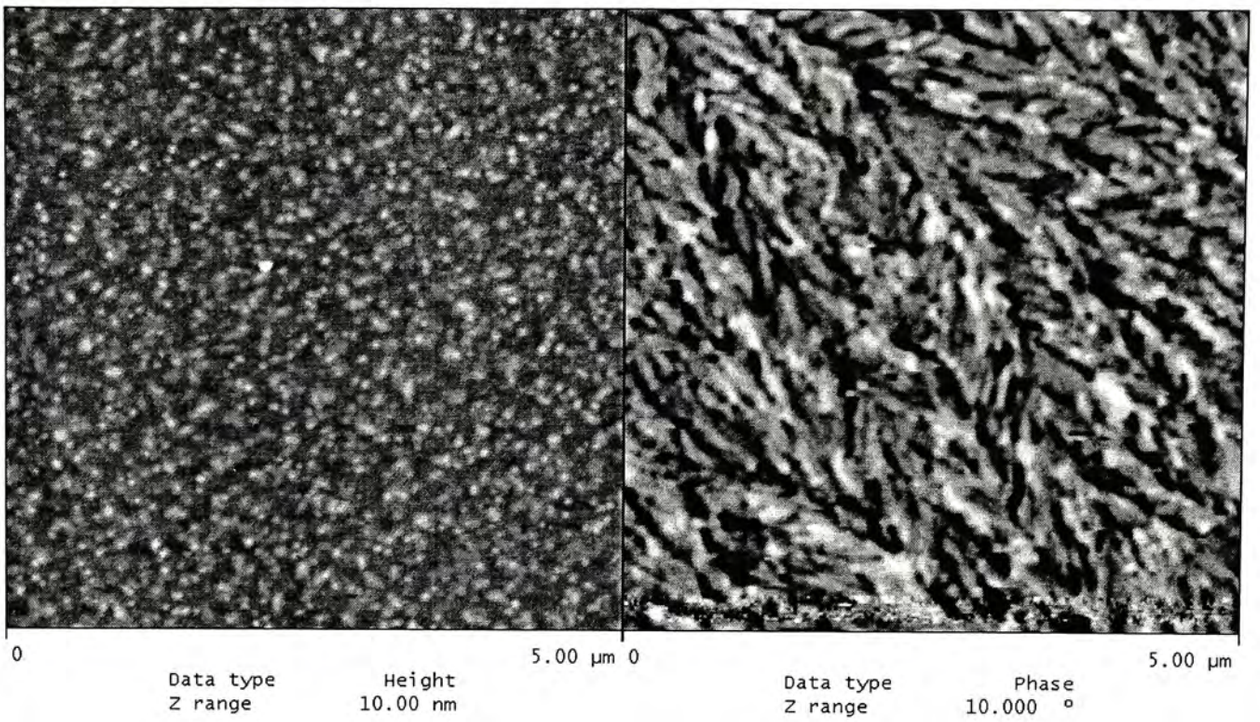
0
5.00 µm
Data type Height
Z range 10.00 nm
0
5.00 µm
Data type Phase
Z range 10.000 °

(c)

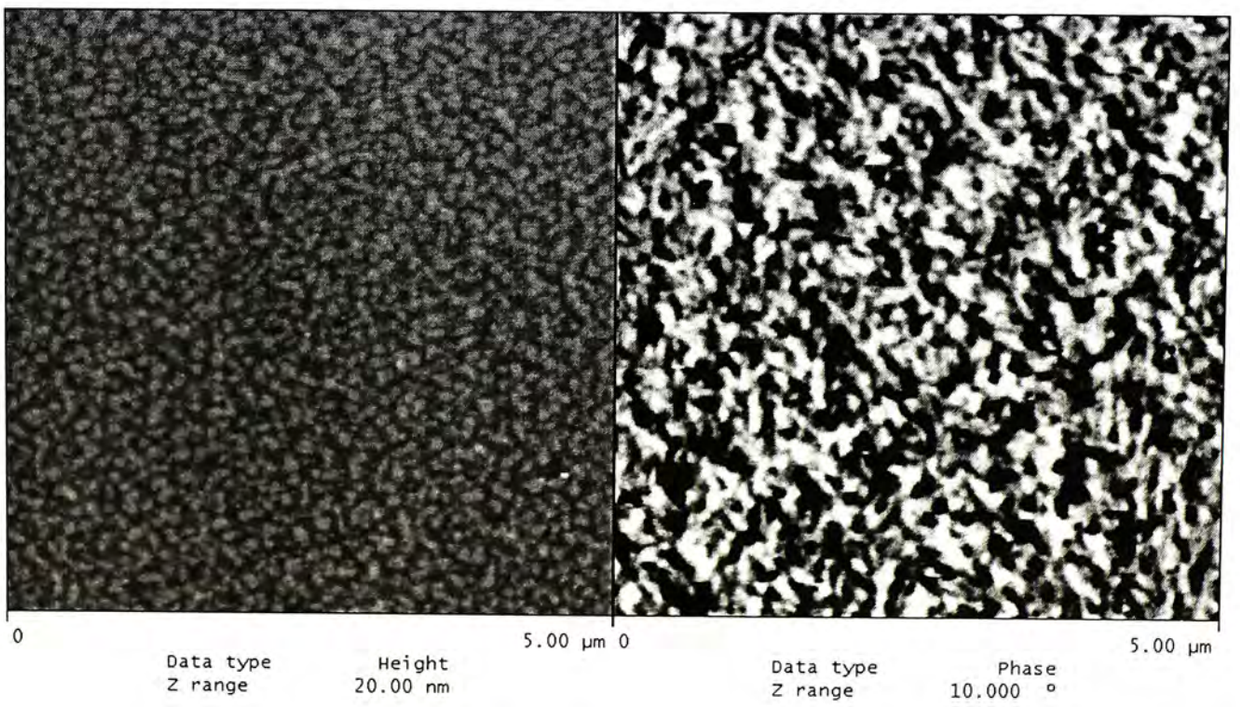
0
5.00 µm
Data type Height
Z range 20.00 nm
0
5.00 µm
Data type Phase
Z range 10.000 °

(d)

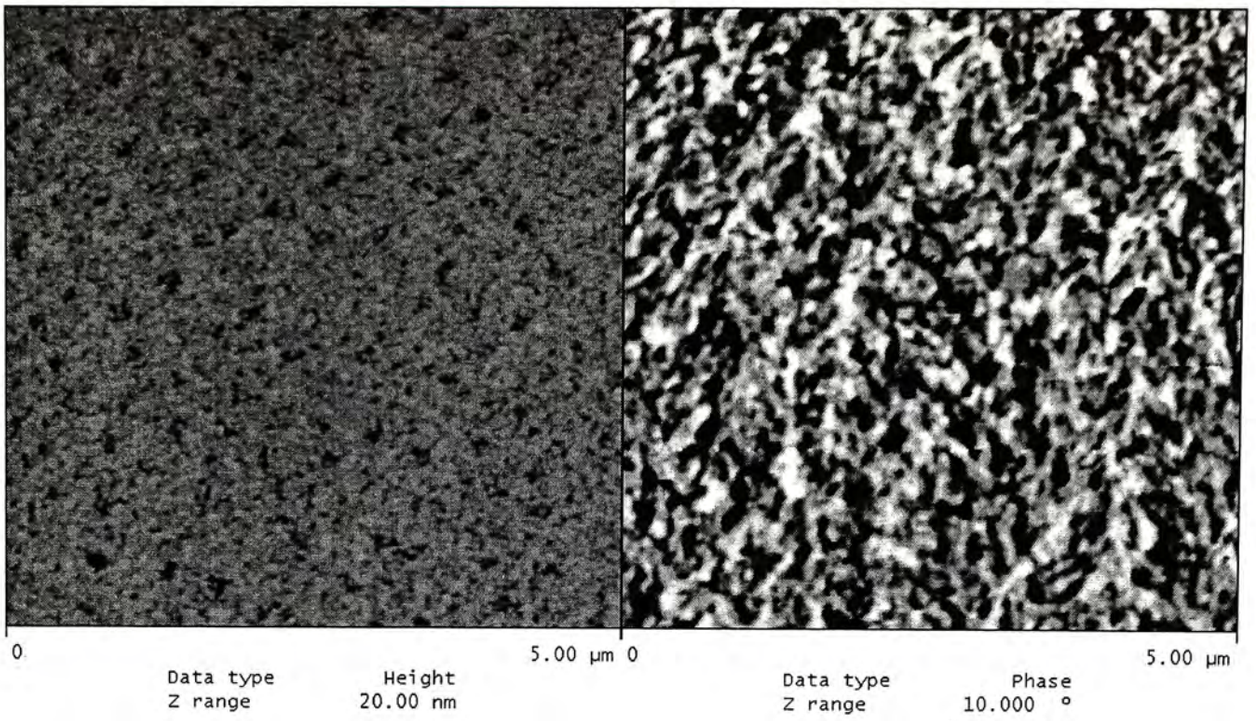


(e)

**Fig. 4.7** AFM (left) and MFM (right) images of sizes 5 $\mu$m×5 $\mu$m of the $Fe_{90}C_{10}$ nanocomposite films. (a) as-deposited; (b), (c), (d) and (e), after annealing at 200℃, 300℃, 400℃ and 500℃, respectively

### 4.2.6 Vibrating sample magnetometer (VSM) measurements

The standard in-plane M/H loops Fe-C granular magnetic thin films of three compositions were obtained by VSM measurements.

Two typical in-plane M-H loops are shown in Fig. 4.8. They can show the magnetic properties of the bcc-Fe phase and $Fe_3C$ phase. The saturation magnetization (Ms), the coercive field (Hc), the saturation magnetic field (Hs) and the ratio of the remanence to the saturation magnetization ($M_r/M_s$) for these films are listed in details as an Appendix. For easy comparison, a simplified table including only values of the as-deposited samples and the 400℃ annealed samples are given in Table 4.1 to give a general idea of the properties of these samples. The saturation magnetization and coercivity against annealing temperature graphs were also shown in Fig. 4.9 and Fig. 4.10, respectively.

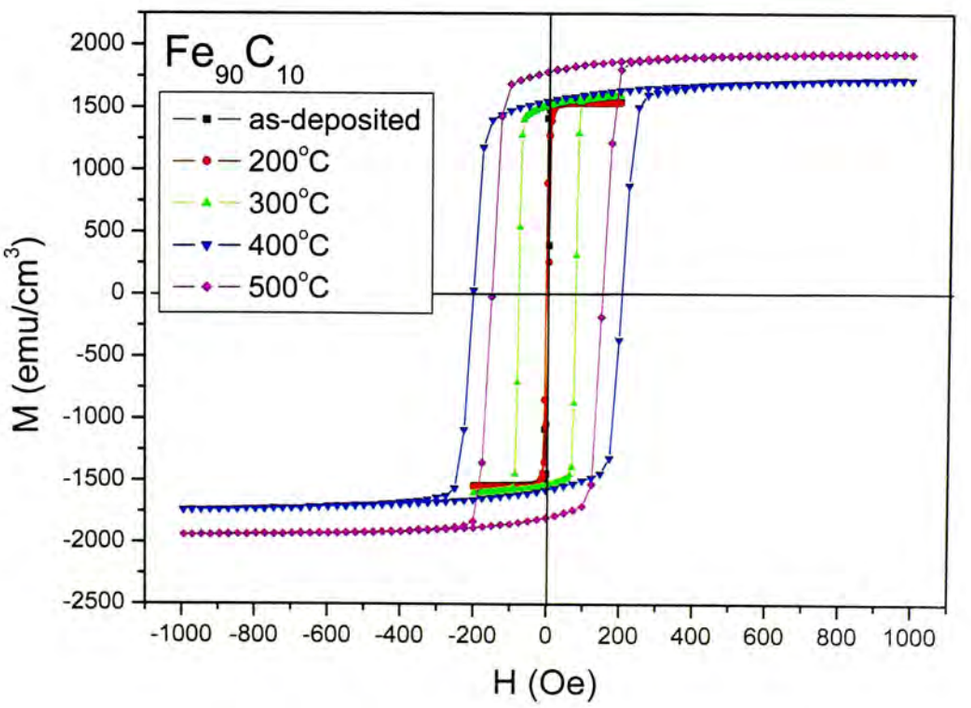


(a)

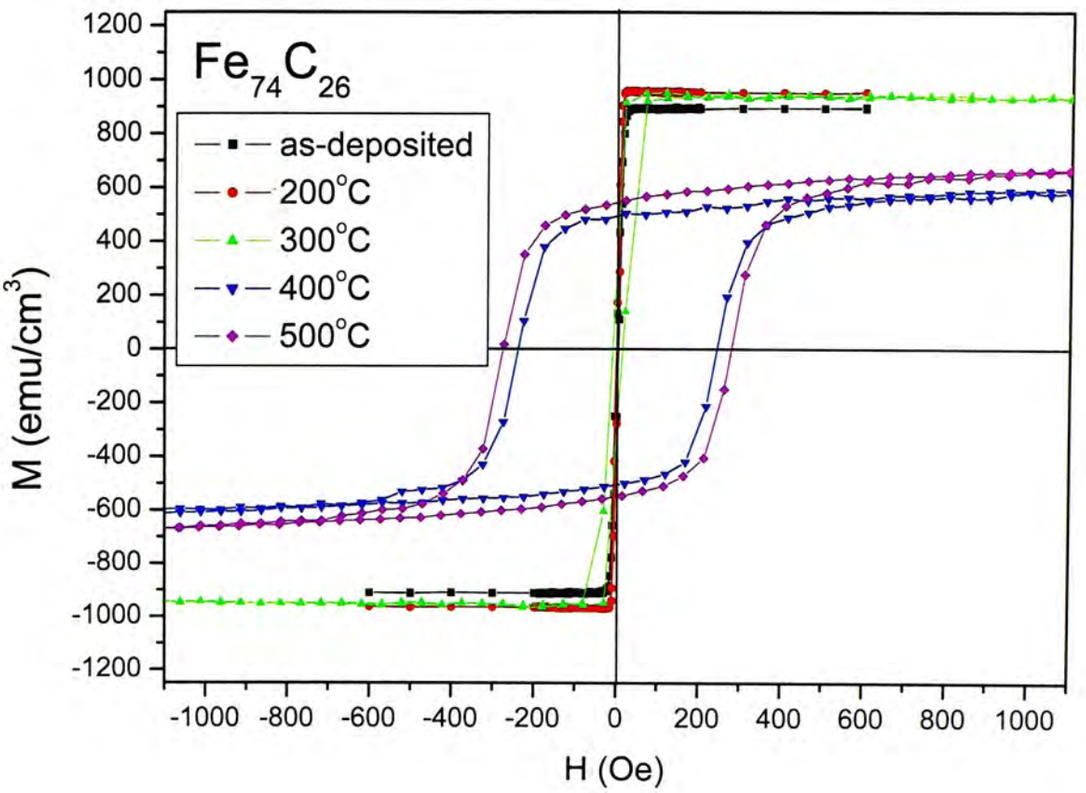


(b)

**Fig. 4.8** In-plane M-H hyteresis loops for (a) $Fe_{90}C_{10}$ and (b) $Fe_{74}C_{26}$ at different annealing temperatures

| Sample | $T_a$(℃) | $M_s$ (emu/cm$^3$) | $H_c$ (Oe) | $H_s$ (Oe) | $M_r/M_s$ |
|---|---|---|---|---|---|
| $Fe_{66}C_{34}$ | as-dep. | 670 | 4 | 70 | 0.42 |
| | 400 | 470 | 110 | 360 | 0.88 |
| $Fe_{74}C_{26}$ | as-dep. | 890 | 5 | 20 | 0.21 |
| | 400 | 610 | 235 | 610 | 0.87 |
| $Fe_{90}C_{10}$ | as-dep. | 1550 | 7 | 20 | 0.90 |
| | 400 | 1720 | 200 | 550 | 0.88 |

**Table 4.2** Saturation magnetization $M_s$, coercivity $H_c$, saturation magnetic field $H_s$ and the ratio of the remanence to the saturation magnetization $M_r/M_s$ as obtained from the M-H loops of the as-deposited and annealed Fe-C films at 300K. ($T_a$ is the annealing temperature, as-dep. is the as-deposited sample.)

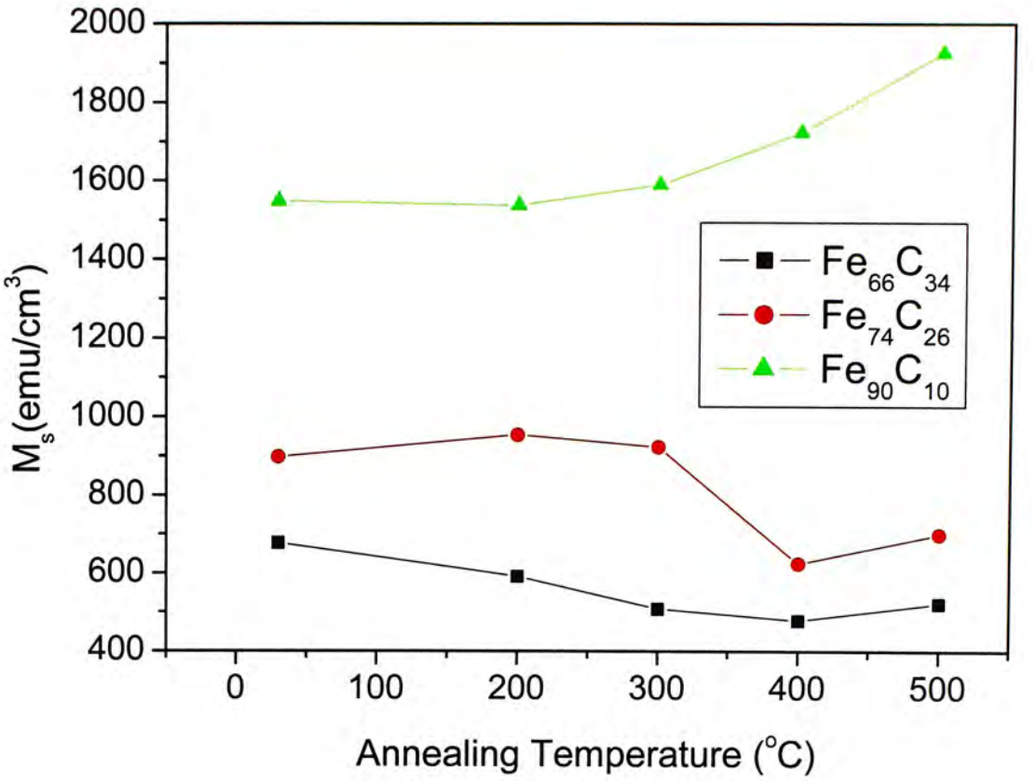


**Fig. 4.9** Saturation magnetization against annealing temperature for different Fe-C samples

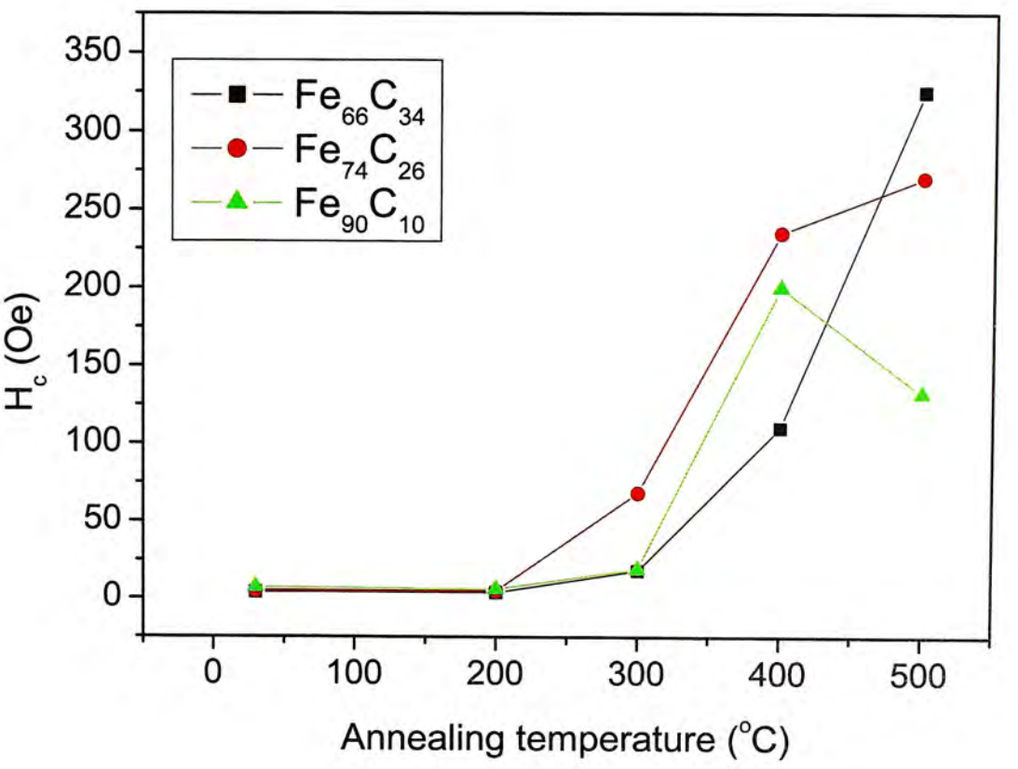


**Fig. 4.10** Coercivity against annealing temperature for different Fe-C samples

In Fig. 4.8 (a), the soft magnetic property of the as-deposited $Fe_{90}C_{10}$ film is clearly seen. The saturation magnetization is quite high with a value of about 1550 emu/cm$^3$ and the coercivity is about 7 Oe. When this film was annealed, the magnetic property became hardened and the coercivity increased (Fig. 4.10). The largest coercivity value reached 200 Oe when the $Fe_{90}C_{10}$ film was annealed at 400℃ (Fig. 4.10). $H_c$ decreased to 132 Oe when the $Fe_{90}C_{10}$ film was annealed at 500℃. This may be attributed to the possible contact of neighboring Fe grains after annealing at this temperature, which may lead to the formation of effective multi-domain structures. Also, the saturation magnetization increased to the highest value of 1930 emu/cm$^3$ when the $Fe_{90}C_{10}$ film was annealed at 500℃ (Fig. 4.9).

The as-deposited and low temperature annealed equal to or lower 200℃ also showed $Fe_{74}C_{26}$ film soft magnetic properties with a low coercivity because of the amorphous nature of these films. They also became magnetically hardened after annealing at higher temperatures (≧300℃). But the saturation magnetization of these samples became lower because the $Fe_3C$ phase was formed. For bulk materials, iron has a high saturation magnetization of 212 emu/g which is higher than that of iron carbide (140 emu/g) [33]. The $M_s$ value decreased from 900emu/cm$^3$ for the as-deposited sample down to 700 emu/cm$^3$ for the 500℃ annealed sample. But the coercivity increased from 5 Oe as-deposited to 270 Oe as-deposited and annealed 500℃, respectively. Moreover, sample $Fe_{66}C_{34}$ is very similar to$Fe_{74}C_{26}$ sample like the structural formation by XRD results. So the saturation magnetization decreased and the coercivity increased when these samples from as-deposited to annealing at 500℃.

### 4.2.7 Resistivity

The resistivities of three Fe-C samples were measured by the four-contact technique. The resistivity as a function of temperature ranging from 30 to 300K is shown in Fig. 4.11. At temperatures below about 100K, all the as-deposited samples show constant resistivity values of about 111 $\mu\,\Omega$cm, 93 $\mu\,\Omega$cm and 87 $\mu\,\Omega$cm for the $Fe_{66}C_{34}$, $Fe_{74}C_{26}$ and $Fe_{90}C_{10}$samples, respectively. The resistivities of all samples then increased to high values as the temperature increased to beyond 100K. In general, the electrical resistivity of these Fe-C granular thin films showed metal-like behaviour. The room temperature resistivity values were determined to be 125 $\mu\,\Omega$ cm, 102 $\mu\,\Omega$cm and 98 $\mu\,\Omega$cm for the as-deposited $Fe_{66}C_{34}$, $Fe_{74}C_{26}$ and $Fe_{90}C_{10}$ samples, respectively.

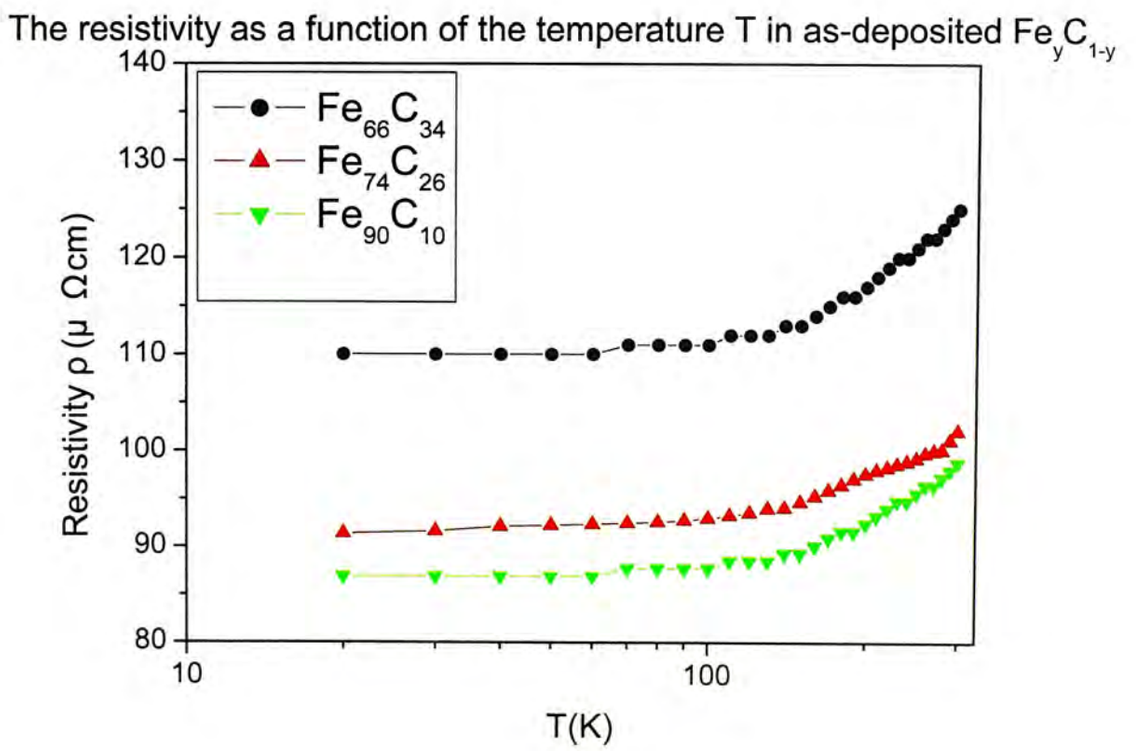


**Fig. 4.11** The graph of resistivity as a function of the temperature T in as-deposited $Fe_yC_{1-y}$ samples

### 4.2.8 Transmission electron microscopy (TEM):

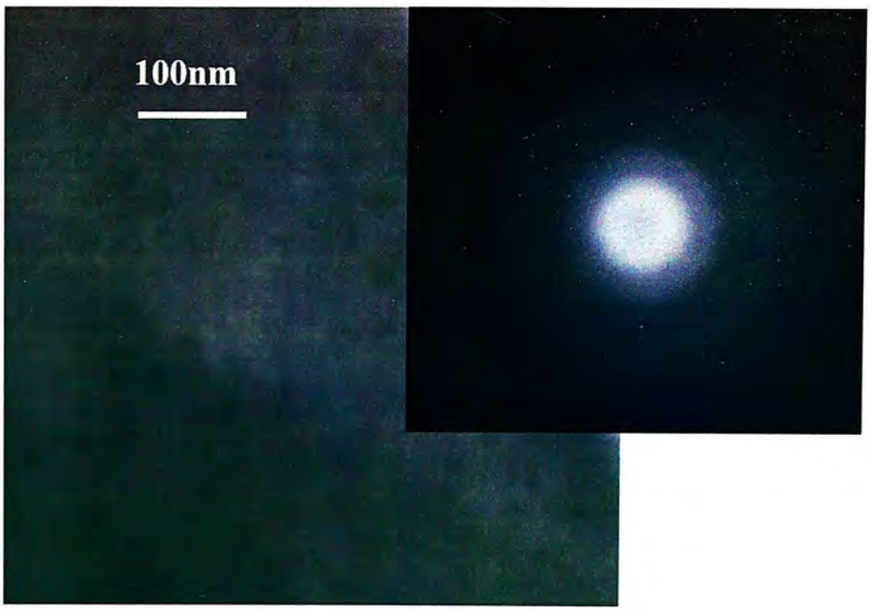


**Fig. 4.12** TEM plan-view bright field (BF) micrographs and electron diffraction (ED) pattern (insert) for the as-deposited $Fe_{90}C_{10}$ film

Both TEM and XRD results showed that the as-deposited $Fe_yC_{1-y}$ films were amorphous. Fig. 4.12 is the plan-view bright field (BF) micrographs and electron diffraction (ED) pattern (insert) for the as-deposited $Fe_{90}C_{10}$ film. As shown in Fig. 4.12, the electron diffraction (ED) pattern shows halos. It indicates that the film is amorphous. The bright field (BF) micrograph shows granular structure through the contrast is weak.

## 4.3 Application potential

Since the requirements for thin film head core materials are high moment to generate high field without saturation of the core, low coercivity ($H_c$) to reduce magnetic hysteresis loss and high resistivity ($\rho$) to suppress eddy current. Our results show that the as-deposited $Fe_{90}C_{10}$ sample is quite suitable for this application.

First, the XRD and TEM results show that the as-deposited $Fe_{90}C_{10}$ sample is amorphous (Fig. 4.3 and Fig. 4.12). Second, the AFM image also shows that the root-mean-square roughness is only about 0.15 nm. It is quite smooth and suitable for the magnetic head application. Third, from the in-plane hyteresis loop of this sample, the saturation magnetization is about 1550 emu/cm$^3$ and the coercivity is 7 Oe (Fig 4.13 and Fig. 4.14). Finally, the resistivity of this sample at room temperature is about 98 $\mu\Omega$cm (Fig. 4.15). These values show that the as-deposited $Fe_{90}C_{10}$ films may seek their applications as high-density magnetic recording head.

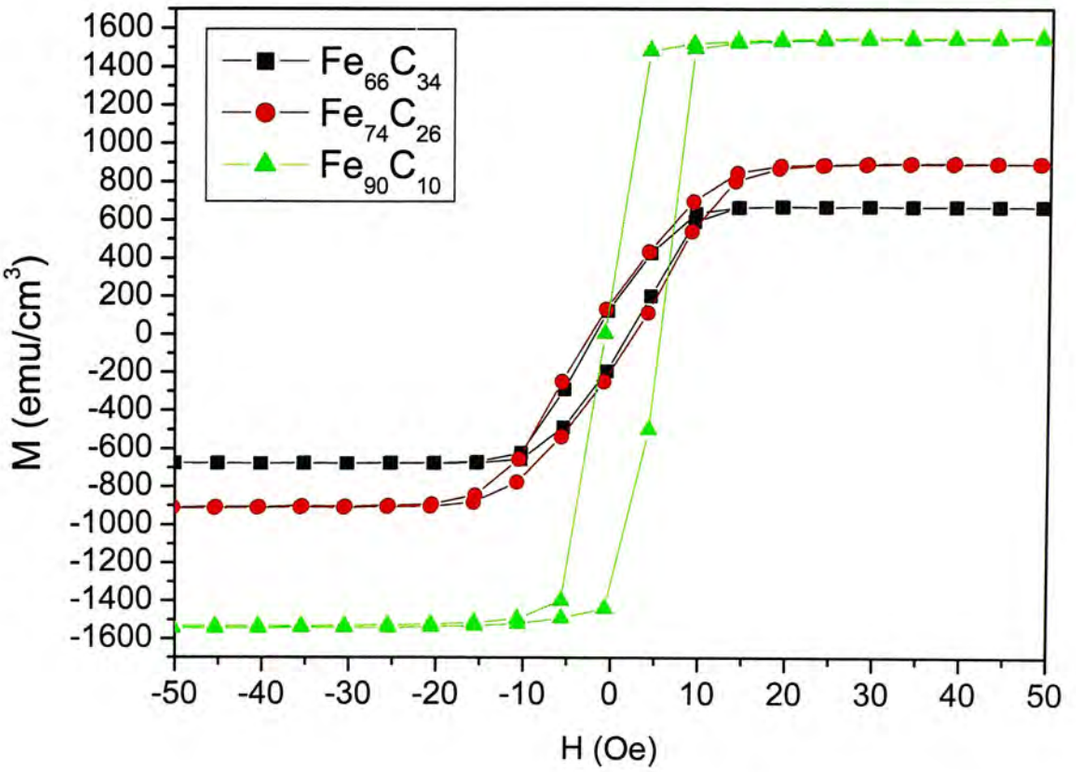


**Fig. 4.13** In-plane M/H loop for as-deposited $Fe_yC_{1-y}$ samples at room temperature

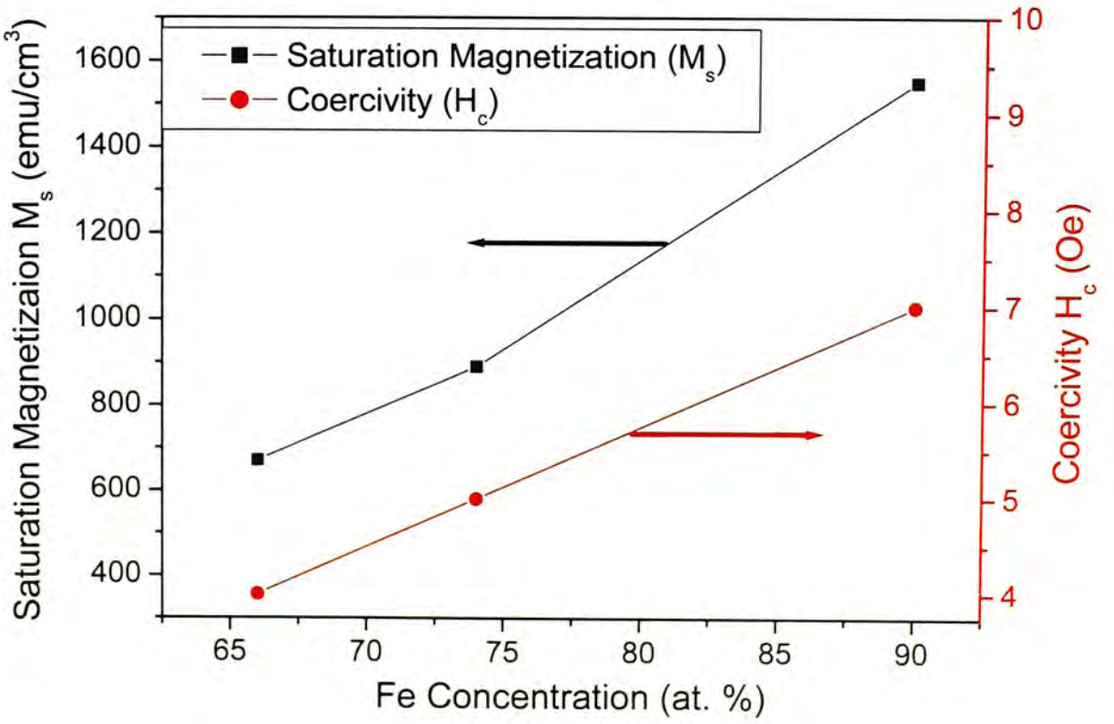


**Fig. 4.14** In-plane $M_s$ and $H_c$ values for as-deposited $Fe_yC_{1-y}$ samples at room temperature

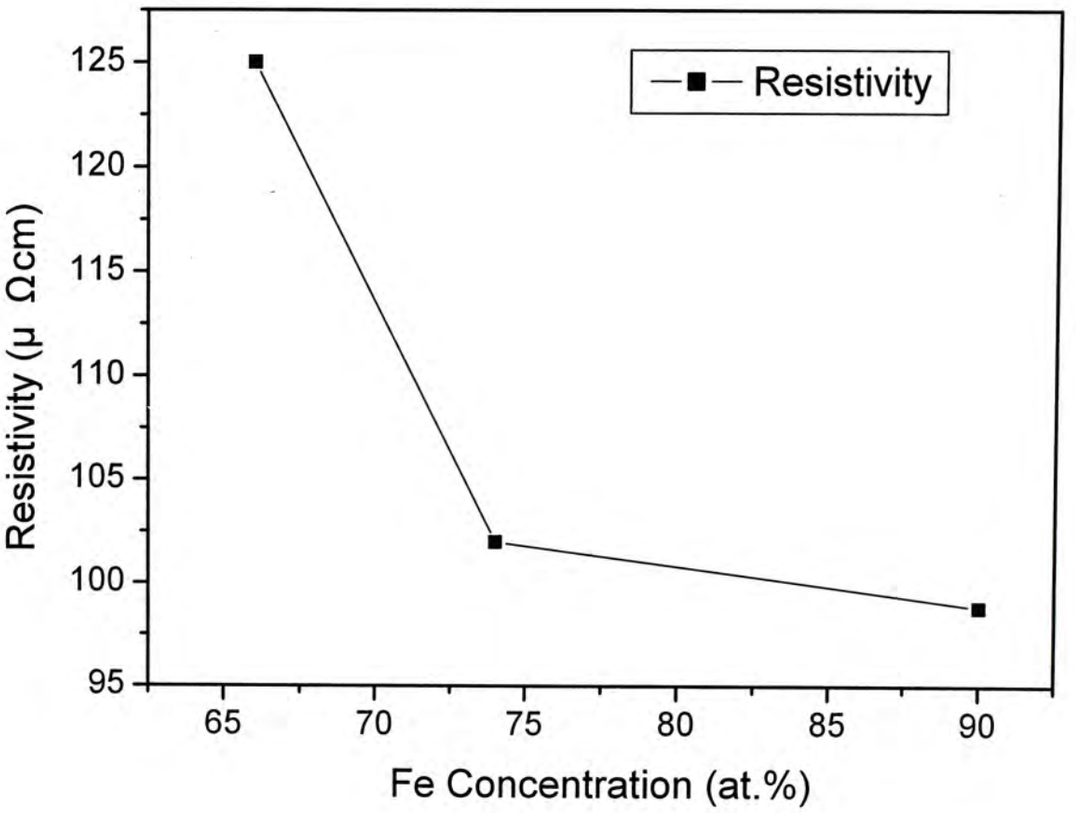


**Fig. 4.16** Resistiviy of the as-deposited $Fe_yC_{1-y}$ samples at room temperature

## 4.4 Summary

We have prepared Fe-C thin films using the pulsed filtered vacuum arc deposition technique. As the data rate in magnetic recording is approaching gigahertz levels, there is urgent need in the development of soft magnetic materials with high magnetic moment and high resistivity for magnetic recording head applications. This application requires the saturation magnetization to bein the range of 1400 – 1700 emu/cm$^3$ [10, 11], the coercivity to be around 5 Oe [10], and a moderate resistivities of ~100 $\mu\,\Omega$cm [12]. For the as-deposited $Fe_{90}C_{10}$ granular magnetic thin film, it shows a high saturation magnetization of 1550 emu/cm$^3$. The coercivity and resistivity of this sample are about 7Oe and 98 $\mu\,\Omega$cm at room temperature, respectively. And the roughness of this sample is about 0.15nm. These films may seek their applications as high-density magnetic recording head.

Moreover, XRD measurements showed that bcc-Fe phase was formed in the $Fe_{90}C_{10}$ samples when the annealing temperature was above 300℃. The AFM images also show the roughness of these samples increases with annealing temperature. The domain structures in these films were studied using MFM observations. The domain structures of the co-deposited $Fe_{90}C_{10}$ also depend on annealing temperature. MFM images with good contrast showing clear domain structures are observed for samples with higher annealing temperatures. Higher saturation magnetization of values up to 1930 emu/cm$^3$ and coercivity up to 200 Oe were obtained at higher annealing temperatures.

For the $Fe_{66}C_{34}$ and $Fe_{74}C_{26}$ samples, $Fe_3C$ phase was formed when they were annealed at above 400℃. The dependence of $M_s$ and $H_c$ of these samples on

annealing temperature was also obtained.

# Chapter 5 Conclusion

## 5.1 Main results of this work

In this work, we have used a new method namely, the pulsed filtered vacuum arc co-deposition method, to prepare the granular metal-carbon magnetic thin films. The magnetic properties of these films were studied by vibrating sample magnetometer (VSM) and their relation to the processing conditions have been studied and discussed in conjunction with results of non-Rutherford backscattering spectrometry (NRBS), x-ray diffraction (XRD), transmission electron microscopy (TEM), x-ray photoelectron spectroscopy (XPS), atomic-force microscopy (AFM), magnetic-force atomic microscopy (MFM) The resistivity was measured by the four-contact technique.

Firstly, the Co-C granular films prepared by pulsed filtered vacuum arc co-deposition method. For their results, we would like to separate the structural and magnetic parts for discussion. In the structural part, the hcp-Co phase is formed when the samples annealed above 500℃ and the concentration of Co above 30 at.%. The root-mean-square roughness value of these samples is also increased to above 0.25nm. In magnetic part, MFM images with good contrast and aggregated large domains are observed in these samples when they annealed at 500℃ or above. The Co concentration increases from 13 at.% to 49 at.%, Ms is increased almost linearly from 60 eum/cm$^3$ to 620 eum/cm$^3$. But the coercivity increases and then decreases at the cobalt concentration 43 at.% because the enhancement of intergrain exchange coupling and the percolation threshold is reached. $H_c$ reaches the maximum value about 700 Oe. After optimization, the sample $Co_{43}C_{57}$ annealed at 600℃ is applied to the high-density recording media but it can be improved with addition with Pt to

the Co-C samples.

Secondly, prepare Fe-C thin films also using pulsed filtered vacuum arc deposition technique. The as-deposited films are amorphous and magnetically soft. For the as-deposited $Fe_{90}C_{10}$ granular magnetic thin films, they should have high saturation magnetization to be 1550 emu/cm$^3$. The coercivity and resistivity of this sample are about 7 Oe and 98 $\mu\Omega$cm at room temperature, respectively. And then the roughness of this sample is about 0.15nm. Since the data rates in magnetic recording approach gigahertz levels, high-moment materials, soft and high resistivity so as to minimize the eddy current effects in magnetic recording heads is developing, these films may seek their applications as high-density magnetic recording head.

Moreover, XRD measurements showed that bcc-Fe phase was formed in the $Fe_{90}C_{10}$ samples when the annealing temperature was above 300℃. The AFM images also show the roughness of these samples increases with annealing temperature. The domain structures in these films were studied using MFM observations. The domain structures of the co-deposited $Fe_{90}C_{10}$ also depend on annealing temperature. MFM images with good contrast showing clear domain structures are observed for samples with higher annealing temperatures. Higher saturation magnetization of values up to 1930 emu/cm$^3$ and coercivity up to 200 Oe were obtained at higher annealing temperatures.

For the $Fe_{66}C_{34}$ and $Fe_{74}C_{26}$ samples, $Fe_3C$ phase was formed when they were annealed at above 400℃. The dependence of $M_s$ and $H_c$ of these samples on annealing temperature was also studied.

## 5.2 Future work

First of all, in order to attain higher coercivity, addition of Pt element to the Co-C thin films is required. It should not change their nanogranular morphology but higher uniaxial magnetocrystalline anisotropy $K_u$ of fct-cobalt-pt phase is formed. By our new preparation method, three sources can be used at the same time during the experiment. Cobalt, platinum and carbon sources are co-deposited into $SiO_2$ substrate. In our laboratory, Mr. M. F. Chiah was prepared some these samples.

In my opinion, Fe/Pt and Co/ Pt will be implanted into $SiO_2$ substrate. Fct-phase of Fe/Pt and Co/Pt may be formed when they are annealed above 650℃ [24]. It is because these samples have a higher uniaxial magnetocrystalline anisotropy $K_u$. And the $SiO_2$ should replace the role of the carbon for the matrix of the granular magnetic thin film

Secondly, we want to know that bcc-Fe phase and $Fe_3C$ phase are formed or not when the $Fe_{74}C_{26}$ films annealed at 500℃. More detailed investigation by microstructure characterization techniques such as transmission electron microscopy (TEM) is very useful. The TEM technique can give information on the granular size and the structural evolution can be determined by electron diffraction (ED).

Finally, the optimization to obtain the soft magnetic Fe-C thin films is very important. The saturation magnetization $M_s$, coercivity $H_c$ and resistivity $\rho$ can be improved when the composition of Fe is changed. Also, a further study is needed to

clarify these thin films.

## Reference:

[1] W. Kratschmer, L. D. Lamb, K. Fostiropouklos, D. R. Huffman, Nature 347 (1990) 354

[2] J. J. Host, J. A. Block, K. Parvin, V. P. Dravid, J. L. Alpers, T. Sezen, R. Laduca, J. Appl. Phys. 83 (1998) 793

[3] W. Zhang, Ian W. Boyd, et al., J. Appl. Phys., 81, 5211, (1997)

[4] M. J. Carey, A. P. Young, et al., Appl. Phys. Lett. 61, 2935, (1993)

[5] H. Sang, G. Ni, and S. P. Wong et al., IEICE Trans. Electron., Vol. E80-C, 1161, (1997)

[6] J. C. Soares, L. M. Redondo, et al. J. Vac. Sci. Technol. A 16, 1812, (1998)

[7] Callister, D. William, "Materials Science and Engineering" (1999)

[8] H. N. Bertram, H, Zhou, and R. Gustafson, IEEE Trans. Magn., vol. 34, p.1845, (1998)

[9] M. F. Doerner, K. Tang, T. Arnoldussen, H. Zeng, M. F. Toney, and D. Weller, IEEE Trans. Magn., vol. 33, p.978, (1997)

[10] Y. K. Liu and M. H. Kryder, Appl. Phys. Lett. 77, 426 (2000)

[11] B. Viala, M. L. Minor, and J. A. Barnard, J. Appl. Phys. 80, 3941 (1996)

[12] Y. Chen, S. Hossain, C. Qian, M. Miller, and H. C. Tong, J. Appl. Phys. 85, 4562 (1999)

[13] X. Shi, B. K. Tay, H. S. Tan, E. Liu, J. Shi, L. K. Cheah, and X. Jan, Thin Solid Films, 345 (1999)

[14] K. Sekar, G. Kuri, et al., Indian J. Phys. 68A (1), 1-22 (1994)

[15] Dr. Matej Mayer, SIMNRA Version 4.40, (1997)

[16] Nuffield, E. W., "X-ray diffraction method" (1996)

[17] Szymanski, and Herman A., "Raman spectroscopy: theory and practice" (1967)

[18] Long, Derek Albert, " Raman spectroscopy" (1977)

[19] Williams, David B., " Transmission electron microscopy: a textbook for material science" (1996)

[20] Briggs, " Handbook of x-ray and ultraviolet photoelectron spectroscopy" (1977)

[21] Cohen, Samuel H., Bray, and Mona T., "Atomic force microscopy and scanning tunnelling microscopy" (1993)

[22] DMS-magnetic News, www.dms-magnetics.com (2000)

[23] H. Wang, S.P Wong, W. Y. Cheung, N. Ke, M. F. Chaih, H. Liu, and X.X. Zhang, J. Appl. Phys. 88, 2603 (2000).

[24] T. J. Konno and R. Sinclair, Acta Metall. Mater. 42 (1994) 1231.

[25] AISN Software Inc., PeakFit version 4.0, (1995)

[26] S. Prawer, K. W. Nugent, Y. Lifshitz, G. D. Lempert, E. Grossman, J. Kulik, I. Avigal, R. Kalish, Diamond Relat. Mater. 5 (1996) 433.

[27] T. Yoki and T. A. Nguyen, IEEE Trans. Magn. MAG-29, 307 (1993).

[28] E. S. Murdock, R. F. Simmmons, and R. Davision, IEEE Trans. Magn. MAG-28, 3078 (1992).

[29] M. Yu, Y. Liu, D. J. Sellmyer, J. Appl. Phys. 85, 4319 (1999).

[30] J. J. Delaunay, T. Hayashi, M. tomita, S. Hirono, and S. Umemura, Appl. Phys. Lett. 71, 3427 (1997).

[31] H. J. Grabke: Iron steel Inst. Jpn. Int., 1989, vol. 29, pp. 529-538.

[32] I. N. Shabanova and V. A. Trapeznikov: J. Elec. Spectr. Related Phenomena, 1975, vol. 6, pp. 297-307.

[33] X. Q. Zhao, B. X. Liu, Y. Liang, and Z. Q. Hu, Journal of Magnetism and Magnetic Materials, 164 (1996) 401-410.

# Publications

**2002** H. Wang, S. P. Wong, M. F. Chiah, C. Y. Poon, W. Y. Cheung "Structural and electrical properties of $Co_xC_{1-x}$ nanogranular films prepared by pulsed filtered vacuum arc deposition", Thin Solid Films, 405, (2002), 304-309.

**2001** M. F. Chiah, H. Wang, C. Y. Poon, W. Y. Cheung and S. P. Wong, "Characterization of CoPt-C nanocomposite films prepared by pulsed filtered vacuum arc deposition", Materials Research Society Fall Meeting 2001.

**2001** H. Wang, S. P. Wong, M. F. Chiah, W. Q. Li, C. Y. Poon, W. Y. Cheung and N. Ke, "Magnetically soft Co-C granular-like amorphous thin films with high resistivity and high saturation flux density", Materials Research Society Fall Meeting 2001.

# APPENDIX

| Sample | $T_a$(℃) | $M_s$ (emu/cm$^3$) | $H_c$ (Oe) | $H_s$ (Oe) | $M_r/M_s$ |
|---|---|---|---|---|---|
| $Fe_{66}C_{34}$ | as-dep. | 670 | 4 | 70 | 0.42 |
| | 200 | 590 | 4 | 70 | 0.50 |
| | 300 | 510 | 18 | 150 | 0.82 |
| | 400 | 470 | 110 | 360 | 0.88 |
| | 500 | 520 | 330 | 380 | 0.92 |
| $Fe_{74}C_{26}$ | as-dep. | 890 | 5 | 20 | 0.21 |
| | 200 | 950 | 5 | 20 | 0.30 |
| | 300 | 920 | 70 | 50 | 0.33 |
| | 400 | 610 | 235 | 610 | 0.87 |
| | 500 | 700 | 270 | 800 | 0.85 |
| $Fe_{90}C_{10}$ | as-dep. | 1550 | 7 | 20 | 0.90 |
| | 200 | 1540 | 6 | 20 | 0.86 |
| | 300 | 1590 | 19 | 200 | 0.80 |
| | 400 | 1720 | 200 | 550 | 0.88 |
| | 500 | 1930 | 130 | 600 | 0.92 |

**Appendix I** Saturation magnetization $M_s$, coercivity $H_c$, saturation magnetic field $H_s$ and the ratio of the remanence to the saturation magnetization $M_r/M_s$ as obtained from the M-H loops of the as-deposited and annealed Fe-C films at 300K. ($T_a$ is the annealing temperature, as-dep. is the as-deposited sample.)